University of Alberta

The Role of Atmospheric Dynamics and Climate Change on the Fate of Glaciers in the Karakoram, Himalaya

by

Tamara Joleen Janes

A thesis submitted to the Faculty of Graduate Studies and Research
in partial fulfillment of the requirements for the degree of

Master of Science

Department of Earth and Atmospheric Sciences

Fall 2010
Edmonton, Alberta

Examining Committee

Dr. Andrew Bush

Department of Earth and Atmospheric Sciences

Dr. Gerhard Reuter

Department of Earth and Atmospheric Sciences

Dr. Gordon Swaters

Department of Mathematics

Abstract

High-resolution regional climate simulations of the Karakoram, Himalaya have been performed for investigation into the atmospheric dynamics in this region, and their role in the Karakoram's snowfall accumulation and glacial evolution. It has been seen through a combination of field measurements and satellite observations that glaciers in this region appear to be reacting differently to contemporary climate change. This region has exhibited a relatively large number of either static or advancing glaciers whilst other glaciers in the central and eastern Himalaya, as well as around the world, are nearly all retreating. The amount of precipitation received in the Karakoram region depends on the interplay between two climate systems: the westerly winds blowing over the Mediterranean and Caspian Seas, and the summer Asian monsoon winds that blow over the Indian Ocean. This study extends the modelling time frame by performing time slice calculations for the Karakoram region through the 21st century. It is found that, despite region wide simulated temperature changes, the highly elevated regions of the Karakoram mountain range experience positive snow mass balance until the end of the modelling time period. It is speculated that this result is arising from a strong positive correlation between snow mass balance and simulated increases in regional precipitation, which outweighs the negative correlation between snow mass balance and simulated increases in temperature. Also, the extreme elevations within the Karakoram allow regional alpine glaciers to benefit from a strong elevation signal seen in net snowfall accumulation, and hence snow mass balance.

Acknowledgements

I would personally like to thank S. Emily Collier, E. Pollock, Dr. Andrew B.G. Bush, Dr. Bruce Sutherland, and Dr. Paul Myers for their help and support during my studies at the University of Alberta.

Contents

List of Figures

Introduction

Around the world, alpine glaciers have been consistently retreating due to changes in local weather, global atmospheric circulation patterns and, inevitably, climate change (Dyurgerov, 2003; Oerlemans, 2005). As civilization has flourished, our dependency on fossil fuels has led us to the most rapid climate change event in recorded history, which is likely to continue and even accelerate through the 21st century (IPCC, 2007). From the year 1850 to the year 2000, alpine glaciers decreased in mass by almost 50% due to the increase in globally averaged temperatures (Zemp *et al.*, 2006). Most of these drastic changes to the alpine glaciers have occurred within the last 30 years, indicating a correlation with the global climate change that is occurring (Oerlemans, 2005). However, there is a region of alpine glaciers in the Karakoram, Himalaya that seem to be reacting quite differently to the observed changes in global climate.

The Karakoram, Himalaya

The Karakoram is a large mountain range that forms part of the greater Himalayan range, spanning the borders between China, India, and Pakistan, with an average elevation of 5000m (Singh & Ganju, 2008), making it the highest and one of the most inaccessible mountain ranges on Earth (Searle, 1991; Copland *et al.*, 2009). The Himalayan region is the most glaciated part of the world outside the polar regions (Thompson *et al.*, 2000; Seong *et al.*, 2007) and for this reason is frequently referred to as the "third pole". The glaciers within this region are behaving very differently than most other alpine glaciers around the world. A number of glaciers here have been recorded as advancing from the years of 1977 to 2006, in times when glaciers around the world have been consistently retreating (Hewitt, 2005). These observations are counterintuitive, as the warming trend from climate change is suggested to be amplified at higher elevations (Thompson *et al.*, 2000; Hewitt, 2005). Thus, one would expect alpine glaciers at high elevations to be the first to react to an increase in globally averaged temperatures. However, this does not seem to be the case in the very high elevations of the Karakoram. Not only have glaciers in this region been recorded as advancing, but a number of glaciers have also been stated as "surging" (Hewitt, 2005). A surge glacier is one that has a usually short-lived advancement at velocities up to 100 times faster than normal, but does not necessarily experience an increase in glacial thickness. These advancing and surging glaciers indicate a positive mass balance in this region, meaning that the glaciers are acquiring mass through variations in snowfall at a greater rate than they are losing mass through meltwater and runoff.

Climate Factors

In order to understand the seemingly anomalous expansion of the alpine glaciers in the Karakoram region, the atmospheric dynamics of the regional climate need to be understood. The Karakoram region is located at a boundary between tropical and continental climate influences (Archer & Fowler, 2006). There are three distinct climate factors that affect the region of the Karakoram: predominant westerly winds in the winter, the Asian monsoon winds in the summer, and continental anticyclones that determine whether a region experiences cloudy or sunny conditions (Hewitt, 2005, 2007; Seong *et al.*, 2007). The westerlies, which flow over the Mediterranean and Caspian Seas, carry cooler temperatures than the monsoon winds that blow over the warmer Indian Ocean. The strength of these westerly winds, which have been correlated with the Northern Atlantic Oscillation index (NAO) (Thompson & Wallace, 2001), are a determining factor for winter snowfall accumulation in the Karakoram (Archer & Fowler, 2004). Two-thirds of the Karakoram's snowfall accumulation occurs in the winter and spring, when the mid-latitude westerlies are dominant, while the other one-third occurs in the summer, when the summer Asian monsoon winds are dominant (Hewitt, 2007; Seong *et al.*, 2007; Seong *et al.*, 2009). The strength of the summer monsoon, which has been correlated with the El Niño-Southern Oscillation (ENSO) in the tropical Pacific Ocean, plays a key role in determining the amount of summer snow accumulation. During an El Niño event (EN), in which warming and increased precipitation over the central and eastern tropical Pacific Ocean occurs, observations show less precipitation and warmer temperatures associated with a relatively weak summer monsoon. It is likely that with a weakening of the southwesterly monsoon winds entering the Karakoram region, the westerly winds will be dominant and result in cooler temperatures and an increase in snowfall. During a La Niña event (LN), in which cooling and a decrease in precipitation over the central and eastern tropical Pacific Ocean occurs, observations show cooler temperatures and more precipitation associated with strong summer monsoons. It is likely that with a strengthening of the southwesterly monsoon winds entering the Karakoram region, the influence of the westerlies will be suppressed, and warmer temperatures and a decrease in accumulated snowfall will result. NAO, the Asian monsoon and ENSO are discussed in detail in the following sections.

The North Atlantic Oscillation

The North Atlantic Oscillation is a global-scale climate variability pattern that is characterized by fluctuations in sea level pressure between the semi-permanent high and low pressure systems over Iceland and the Azores, respectively known as the Icelandic low and the Azores high (Thompson & Wallace, 2001). The phase of the NAO is distinguished by analyzing sea level pressure differences between the Azores (or Portugal) and Iceland. At times when this difference is large, NAO is said to be in its positive phase, characterized by a strengthening of the mid-latitude westerlies, bringing increased precipitation and cooler temperatures to Europe. When this pressure difference is diminished, NAO is said to be in its negative phase, in which the mid-latitude westerlies are suppressed, allowing for more extreme temperature variations and less precipitation over Europe. While the impacts of NAO have been presumed to be restricted to the region extending from eastern North America to central Europe, the effects of the NAO have, however, been shown to influence climate variability at close to all longitudes of the Northern Hemisphere (Thompson & Wallace, 2001).

It has been suggested by Archer & Fowler (2004) that rainfall changes in the Karakoram region could be partially related to NAO variability. In their study, a significant positive correlation was found between the winter NAO index and winter precipitation in the Karakoram, implying that the enhanced westerlies resulting from a positive NAO phase will penetrate as far east as the trans-Himalayan region, bringing increased precipitation from orographic uplift to the Karakoram. On the other hand, a negative correlation is found between the NAO index and precipitation associated with the Asian summer monsoon, implying less frequent intrusions of the summer monsoon winds into the Karakoram region during times of positive NAO (Dugam *et al.*, 1997). Since it is approximated that two thirds of the Karakoram's annual snowfall accumulation occurs in the winter months, it is imperative to consider the effects of the NAO on westerlies in the Karakoram region.

The Asian Monsoon

The term "monsoon" is traditionally used to define seasonal variations in wind patterns, but is more generally used to describe the tropical and subtropical seasonal reversal in atmospheric circulation and associated precipitation (Trenberth *et al.*, 2000). This atmospheric circulation variability arises from seasonal reversals in temperature gradients between oceans and neighbouring continental land masses. This seasonality is apparent in the two distinct modes of the Asian monsoon. In the summer Asian monsoon, or the "wet" season, higher temperatures occur over the Indian subcontinent than over the Indian Ocean due to differential warming arising from differences in specific heat capacities, which results in a circulation pattern similar to a large-scale "sea-breeze". Warm, moist air originating over the Arabian Sea is carried inland by this circulation pattern, bringing convection and heavy rainfall to the

Indian subcontinent. In this mode, winds over the Indian subcontinent are predominantly southwesterly. In the winter Asian monsoon, or the "dry" season, this temperature gradient is reversed, again due to differences in specific heat capacities, and the resulting circulation pattern is similar to a large-scale "land-breeze". Colder, dry air originating over northern Asia is carried out to sea, resulting in subsidence and a lack of rainfall over the Indian subcontinent. In this mode, winds over the Indian subcontinent are predominantly northeasterly.

The Asian monsoon is sensitive to external large-scale forcing parameters that can either strength or weaken monsoon circulation, such as orbital configuration, glacial-age surface boundary conditions, and atmospheric CO_2 concentration (Prell & Kutzbach, 1992). An overall strengthening of the Asian monsoonal system has been linked to the presence of high topography (Prell & Kutzbach, 1992; Trenberth *et al.*, 2000), increased summer solar radiation from orbital parameter variations (Prell & Kutzbach, 1992), as well as the uplift of the Tibetan Plateau, a result of post-collisional convergence between India and Eurasia roughly 50 million years ago (Ma) (Zhisheng *et al.*, 2001). However, the timescales over which many of these variations occur are much too long to be resolved in this study, and hence we will focus our attention on variations in the monsoon due to changes in atmospheric CO_2 concentration.

Variations in the Asian monsoon have a large impact on the Karakoram region, as the strength of the monsoon will affect the rate of summer precipitation over the region, and hence will be a deciding factor for a glacier's potential to advance or retreat.

The El Niño Southern Oscillation (ENSO)

As mentioned previously, variations in the El Niño-Southern Oscillation (ENSO) have an impact on the Asian monsoon (Yanfeng & Longxun, 2002), which in turn has an impact on the fate of glaciers in the Karakoram region. ENSO is an interannual climate variability that occurs across the tropical Pacific Ocean, with implications for climate variability around the world. It is known as "quasi-periodic", as while the length of ENSO events is relatively well known, the time interval between consecutive ENSO events can range from 2 to 10 years (Philander, 1997).

ENSO involves an oscillation in both the atmosphere and the ocean. The oceanic component consists of a warm and cold phase, named El Niño and La Niña respectively. During an El Niño phase, there is an eastward transfer of heat from the warm-water pool in the western Pacific Ocean, resulting in positive sea surface temperature anomalies in the majority of the tropical Pacific Ocean along with a shallower east-west thermocline slope. During a La Niña phase, there is a westward advancement of the cold-water tongue located off the west coast of South America, resulting in negative sea-surface temperature anomalies for much of the eastern Pacific Ocean, along with a steepening of the east-west thermocline slope as the warm-water pool in the western Pacific is confined. It is often harder to define a La Niña event, as it is characterized by a strengthening of the tropical Pacific's normal conditions. The atmospheric component, or the Southern Oscillation, is characterized by an oscillation in surface pressure between the tropical eastern and western Pacific. The strength of this oscillation is measured by the Southern Oscillation Index (SOI), which focusses on the pressure differences between Tahiti in the eastern Pacific, and Darwin, Australia in the western Pacific. When the pressure in Tahiti tends to be higher than the pressure in Darwin, positive values of the SOI occur, along with increased rainfall in the western Pacific and decreased rainfall in the eastern and central Pacific. This pressure difference induces a strengthening of the equatorial easterly trade winds (part of the Walker circulation), which in turn induces strong coastal upwelling of cold, deep ocean waters off the west coast of South America, possibly inducing a La Niña oceanic phase. When the pressure in Tahiti tends to be less than the pressure in Darwin, negative values of the SOI occur, along with increased rainfall in the eastern and central Pacific, and decreased rainfall in the western Pacific. This pressure difference induces a weakening, or even a reversal, of the equatorial easterly trade winds, which allows for the warm-water pool in the western Pacific Ocean to migrate eastwards, indicating a shift towards an El Niño oceanic phase.

While the causes of ENSO events are unknown, it is theorized that they are initiated by the changes in strength of the equatorial easterlies. As these easterlies weaken, heat is transported eastward by an equatorial Kelvin wave propagating along the thermocline. The arrival of the Kelvin wave at the west coast of South America signals the beginning of a warm, El Niño event. These warm events have been tied to warm, mild winters in western North America, extreme droughts in the Indonesian region, Australia, and South Africa, and a much weaker summer Asian monsoon. At the end of an El Niño event, the ocean returns to its normal state, however it is possible for the ocean to overshoot this normal state, resulting in stronger than normal equatorial easterlies. If there is a strengthening of these easterlies, there is an inhibition of eastward heat transport, and a cold, La Niña event will ensue, which has mostly the opposite effects on global climate than El Niño.

Objectives

The intent of this project is to investigate the interplay of regional atmospheric dynamics over the Karakoram region in order to understand how these processes influence the region's glacial dynamics. Through regional climate modelling studies for a future climate scenario, we aim to determine the atmospheric dynamics that govern the mass balance of glaciers in this very unique region. Unfortunately, no existing model is able to accurately portray all of the climate factors influencing atmospheric dynamics in the Karakoram region, nor do these existing models incorporate any dynamical or hydrological aspects of alpine glaciers. For this reason, our modelling objectives are limited to those climate factors that are well-simulated by our chosen model, namely the midlatitude westerlies, ENSO, the Asian monsoonal system and detailed regional atmospheric dynamics.

Chapter 1 of this paper describes the two numerical models used in this project, as well as their parameterizations. Chapter 2 outlines the results obtained from future climate scenarios performed over the 21st century with focus on the Karakoram region, and Chapter 3 covers the discussions and conclusions of this study.

Numerical Model Setup

1.1 Introduction to the Mesoscale Model

The Fifth-Generation National Center for Atmospheric Research/Penn State University Mesoscale Model 5 version 3 (NCAR/PSU MM5 v.3, herein denoted as MM5) is the chosen fine-mesh, coupled non-hydrostatic mesoscale model for performing the regional climate simulations in this project. MM5 is designed to perform mesoscale and regional scale simulations of atmospheric circulations by interpolating global pressure level data to a predefined horizontal grid (Hernandez *et al.*, 2006; Grell *et al.*, 1994). By solving the mathematical equations outlined in Grell *et al.* (1994), as well as in Appendix A of this study, MM5 is able to compute wind and temperature fields, among other meteorological quantities, as a function of time.

Over regions of complex topography such as the Himalayan region, dynamical forcing can vary on a scale of less than a few hundred kilometres. Therefore, obtaining meaningful results in the presence of complex topography requires a model with fine horizontal resolution, as seen in MM5 (Dickinson *et al.*, 1989). Without the fine-mesh attributes of this model, parameters such as precipitation could be grossly underestimated due to a lack of resolution over high-elevation mountain ranges. By embedding this high-resolution, limited area model within a global atmosphere-ocean model that will be described in section 1.2, high-resolution results over complex, seasonally snow-covered topography are achievable, as seen in the studies by Dickinson *et al.* (1989), Bromwich *et al.* (2005) and Hernandez *et al.* (2006). Thus, MM5 is an adequate regional model for simulating climate scenarios in the Karakoram, Himalaya.

1.2 Mesoscale Model Setup and Parameterizations

MM5 performs with 24 terrain-following sigma levels, where sigma is a dimensionless quantity that can range from 0, being the model top with a relatively low vertical resolution, to 1, being the surface level with much higher vertical resolution (Grell *et al.*, 1994). One outer domain and two nested domains with a horizontal resolution of 90 km, 30 km and 10 km are created to obtain output over the Karakoram, Himalaya. Each of these domains has 75x80, 61x61 and 52x61 gridpoints, respectively (as seen in Figure 1.1). The outer domain is driven by output from the atmosphere-ocean global circulation model described in the following section, with no feedbacks between the two models, whereas the two inner domains are two-way coupled and communicate data between themselves throughout the integration. A closer view of the highest resolved domain is shown in Figure 1.2.

For an area such as the Karakoram, in which seasonal differences are vast, the National Center for Environment Prediction (NCEP), Oregon State Uni-

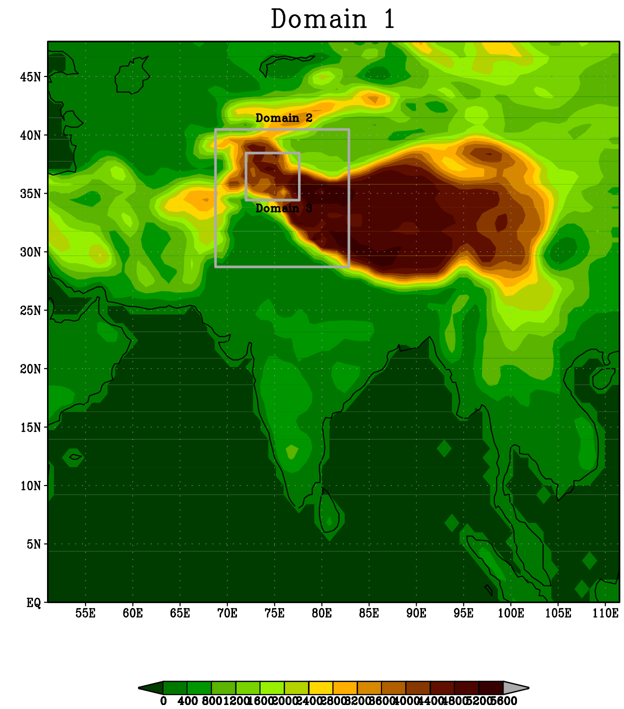

Figure 1.1: The 3 chosen regional model domains, plotted over topography (elevation contours in metres).

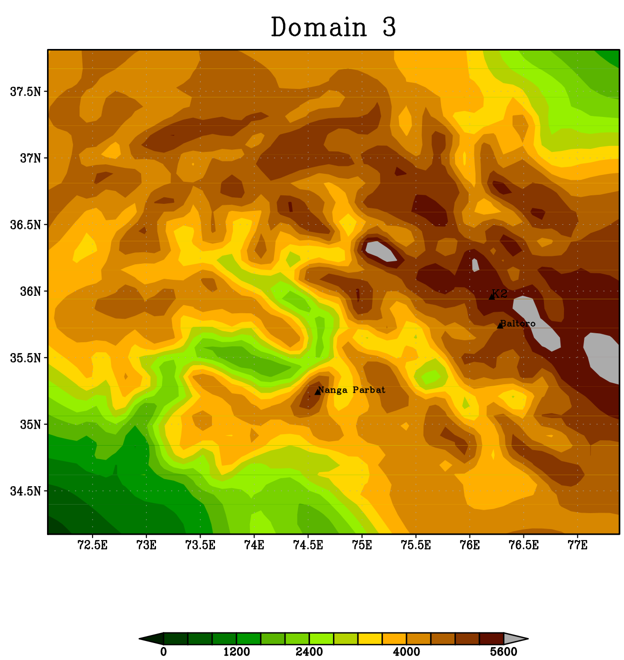

Figure 1.2: A close up of domain 3 with the locations of Nanga Parbat, K2 and the Baltoro glacier, plotted over topography (elevation contours in metres).

versity (OSU), Air Force, Hydrology Research Lab land-surface model (herein denoted as NOAH-LSM) is used to better accomodate for both diurnal and seasonal differences in surface fluxes (see Chen and Dhudia, 2001, Parts I and II). This land-surface model provides us with information on vegetation and land use as well as soil moisture, water content and temperature, which are crucial variables to modelling the atmospheric circulation near the surface. In order to account for the different possible types of precipitation in an area with such vast differences in topography, such as the Karakoram, we have chosen the implementation of the mixed-phase method, as seen in Reisner *et al.* (1998), in which explicit parameterizations were created to include ice physics and super-cooled liquid water in the formation of precipitation. This parameterization allows for five separate states of precipitation: rain, snow, ice, vapour, and cloud. The planetary boundary layer formulation seen in Troen and Mahrt (1986) is used, which requires only modest vertical resolution and is therefore an adequate choice for use with MM5.

1.3 Introduction to the Atmosphere-Ocean Global Circulation Model

A coupled atmosphere-ocean global circulation model (herein denoted as GCM) is used to create the boundary conditions necessary to perform simulations in MM5. The atmospheric component of this model is the Princeton Geophysical Fluid Dynamics Laboratory global spectral model (see Gordon & Stern, 1982) which contains 14 terrain-following sigma levels with rhomboidal truncation at wavenumber 30. This results in an equivalent spatial resolution in the latitude and longitude of 2.25° at the equator, decreasing at higher latitudes, and 3.75° respectively (Bush, 2004).

This global spectral model is then coupled with the Modular Ocean Model version 2, also developed at the Princeton Geophysical Fluid Dynamics Laboratory (see Pacanowski, 1995). This model has 15 levels in the vertical, and a horizontal spatial resolution similar to the global spectral model with 2° in the latitude and 3.62° in the longitude (Bush, 2004). Through the integration of this coupled model, global circulation datasets with daily variability are created, which can then be used as initial and lateral boundary conditions for the MM5 model. This method of embedding course-resolution GCM results within a high-resolution mesoscale model, known as "climate downscaling", is used to achieve more accurate climate representations in the presence of large bodies of water, vegetation, or complex topography than the global atmosphere-ocean model could achieve alone, and has been used successfully in studying the regional climate for the topographically-complex western United States (Dickinson *et al.*, 1989; Giorgi, 1990), as well as over Europe (Giorgi *et al.*, 1990; Giorgi *et al.*, 1997), and simulations for the Asian summer monsoon (Ji & Vernekar, 1997). The future climate scenario integrations of this model are discussed in sections 2.1.

Simulations of the Potential Effects of Rising CO_2

In one of the first studies of atmospheric CO_2 and its influence on global temperatures, Callendar (1938,1949) suggested that due to carbon dioxide's strong absorbing power in the infrared region of the spectrum, the ever increasing concentration of CO_2 in our atmosphere will have a warming effect on globally averaged temperatures. As natural and anthropogenic changes to the climate system alter the radiative balance, adjustments in temperature, precipitation and other quantities are needed in order to reach a new equilibrium consistent with this radiative forcing, which arises from perturbations in the infrared (from changes in greenhouse gas concentrations) and solar (from changes in the surface albedo or the presence of aerosols) components of the radiation spectrum (Boer *et al.*, 2004). Since the proposal of this theory in the 1930's, the topic of climate change due to increasing atmospheric CO_2 concentrations has received world-wide attention. Numerical simulations of rising CO_2 concentrations performed by Manabe & Wetherald (1975) agree with Callendar's suggestion that an increase in atmospheric CO_2 concentration will lead to a global temperature increase. This proposed warming has been observed and well documented within the last few decades, and was positively correlated with the observed increase in atmospheric CO_2 by Hansen *et al.* (1981). The global consequences of a warming climate have sparked many scientists to perform simulations of possible climate scenarios in which the atmospheric concentration of CO_2 reaches twice the current amount (herein denoted as the $2XCO_2$ regime). The results of these studies have shown that the observed warming trend, and other global effects of an increase in globally averaged temperatures, will continue through the 21st century, and possibly even increase in intensity (Manabe & Wetherald, 1975; Hansen *et al.*, 1981; Manabe *et al.*, 1991; Manabe *et al.*, 1992; Giorgi *et al.*, 1992; Manabe & Stouffer, 1994; Giorgi *et al.*, 1997; Stouffer, 2004).

Changes in atmospheric CO_2 concentration have not only been linked to an increase in globally averaged temperatures, but have also been shown to modify the hydrological cycle through changes in the strength and location of precipitation and evaporation. Studies by Manabe & Wetherald (1975), Manabe *et al.* (1991), Manabe *et al.* (1992) and Held & Soden (2006) have shown that the observed anthropogenic warming of the atmosphere significantly increases precipitation and evaporation rates around the world. Following the Clausius-Clapeyron expression, as seen in Held & Soden (2006) and given by equation (2.1):

$$\frac{d}{dT}\ln e_s = \frac{L}{RT^2} \tag{2.1}$$

where L is the latent heat of vaporization and R is the universal gas constant, as the atmospheric temperature T gradually warms there is consequently a non-linear increase in saturation vapour pressure e_s (Held & Soden, 2006). This increase in saturation vapour pressure allows the atmosphere to accumulate more water vapour before a precipitation event occurs, and hence amplifies the effect of the hydrological cycle, resulting in more precipitation over wet regions and less precipitation over dry regions (Held & Soden, 2006). A more active hydrological cycle has been shown to cause an increase in intensity of the summer monsoon precipitation over the Indian sub-continent (Prell & Kutzbach, 1992).

Many studies have shown that an increase or decrease in radiative forcing induces an El Niño-like or La Niña-like response of the tropical Pacific Ocean (Meehl & Washington, 1996; Bush & Philander, 1998; Timmerman *et al.*, 1999; Cai & Whetton, 2000; Cubasch *et al.*, 2001; Chen *et al.*, 2005; Guilyardi, 2005). Specifically, the tropical Pacific Ocean exhibits an El Niño-like response to positive radiative forcing (warming), and a La Niña-like response to negative radiative forcing (cooling) (Boer *et al.*, 2004). It has been shown in Boer *et al.* (2004), as well as later in this study, that an increase in greenhouse gas concentration leads to an expansion of the convection region in the tropical Pacific Ocean, and a shift towards an El Niño-like pattern of sea surface temperature anomalies, which will weaken the summer monsoon winds and decrease the frequency of summer monsoon intrusions into the trans-Himalayan region. Along with the tendency of a semi-permanent El-Niño event, it has been suggested that the phase of NAO will also shift towards a more positive state, which has been observed to be occurring over the last three decades (Visbeck *et al*, 2001). However, due to the complex relationship between NAO and ENSO, in which the westerlies associated with NAO tend to be stronger during El Niño events (Alexander *et al.*, 1992; Dugam *et al.*, 1997) , this trend in NAO could be a direct result of the trends suggested for ENSO.

The combination of these changes in global temperature and precipitation, as well as variations in climate circulation patterns such as the monsoon, NAO and ENSO, can have a devastating effect on the fate of alpine glaciers around the world. Oerlemans (2005) has shown that the mass balance of midlatitude and tropical glaciers is strongly correlated with the increase in globally averaged temperatures, stating that the observed increase in temperature is the cause of rapidly receding glaciers in the last century. It has been further suggested by Giorgi *et al.* (1997) that the climate change signal is amplified at higher elevations, resulting in an increase in melting and runoff for high-altitude glaciers. Coupled with the snow-albedo positive feedback, this melting in turn decreases the amount of reflected incoming solar radiation, and hence allows for subsequent recession of the glacier. However, the increasing trend in precipitation and temperature, coupled with the snow-albedo feedback as well as changes in regional climate patterns, can lead to rare cases of glacial expansion, as seen in Alaska (Molnia, 2007), Nepal (Salerno *et al.*, 2008) and the Karakoram, Himalaya (Hewitt, 2005; Hewitt, 2007). If a mountainous region experiences an increase in precipitation in the form of snowfall, the amount of incoming solar radiation is reduced, and through the snow-albedo positive feedback, glacial expansion or even surging can occur (Bush, 2000).

The glaciers contained in the Karakoram, Himalaya, generally differ in elevation and regional climate regimes from most of the glaciers used by Oerlemans (2005) to track glacier evolution resulting from contemporary climate change (Hewitt, 2007). Whereas most glacial surges occur in historical intervals, surges reported within the Karakoram have been out of phase with their observed intervals (Hewitt, 2009; Copland *et al.*, 2009), and a response to climate change is the only reasonable explanation for these events (Hewitt, 2007).

Studies on glacial evolution in the nearby Wakhan Pamir, Afghanistan, which rarely receives summer monsoonal precipitation, have predicted a long-term glacial retreat trend with a doubling of the atmospheric CO_2 concentration (Haritashya *et al.*, 2009). Since one-third of the Karakoram's annual snowfall is contributed by the summer monsoonal precipitation (Hewitt, 2007; Seong *et al.*, 2007; Seong *et al.*, 2009), one would expect the glacial evolution in the Karakoram region to differ from that of the Wakhan Pamir region. Glacial expansion and surging in the Karakoram is limited to glaciers at very high elevations, which contradicts the theory, proposed by Giorgi *et al.* (1997), that the climate change signal is greatly amplified at higher elevations (Hewitt, 2005). However, maximum precipitation in the Karakoram region occurs between 5000 and 6000 metres above sea level, which is 2000-3000 metres higher than what is generally reported for tropical mountain ranges (Hewitt, 2005). Observational records indicate a significant increase in both winter and summer precipitation resulting from greater transport of moisture to higher altitudes, along with winter warming and declining summer temperatures attributed to cloudiness and cyclonic activity, which suggest favourable conditions for a positive mass balance scenario (Archer & Fowler, 2004; Hewitt, 2007).

The climate dynamics of the Karakoram region are complex, but variations in these regimes play an important role in regulating snow accumulation (Seong *et al.*, 2009), and a better understanding of their relationship to glacial mass balance is therefore needed to accurately predict the fate of the Karakoram glaciers in a world of increasing global temperatures. By performing regional scale numerical simulations for the Karakoram, Himalaya, we investigate the evolution of climate dynamics in this region in response to global climate change, and their role on the glacial activity.

2.1 Initial and Lateral Boundary Conditions

The coupled global atmosphere-ocean model described in section 1.2 is integrated twice to create the initial and lateral boundary conditions necessary for integrating MM5. The first of these integrations imposes a modern CO_2 concentration of 387 ppmv for a 28-year control run. The second integration imposes a CO_2 concentration that increases quadratically to 690 ppmv by the year 2110, which follows the IS92a-Fr-Central emission scenario and is comparable to the B2 estimates of the Special Report on Emission Scenarios (IPCC 2007). The datasets are then subdivided into 10-year subsets, each representing a particular time period of interest. The years chosen for these subsets were 17-26 of the control integration, and the years 2020-2029, 2045-2054, 2071-2080, and 2095-2104 of the increasing CO_2 integration (herein denoted as Control, 2025, 2050, 2075, and 2100 respectively). Each 10-year subset is then averaged to create daily boundary condition data containing the 10-year average of each variable, which are then implemented as initial and lateral boundary conditions for the MM5 integrations described below.

2.2 Mesoscale Model Integrations

The regional mesoscale model described in section 1.1 is integrated on a monthly basis, with a 2 day spin-up period and 4.5 hour temporal resolution for the span of one year, resulting in the ability to portray an annual average containing input data from the global atmosphere-ocean model spanning the entire 10 year period. It has been suggested by Qian *et al.* (2003) that a spin-up period of 1 or 2 days, which is implemented in this study, is sufficient enough to allow the model to adjust from the initial conditions (or the "initial shock"). A total of 60 MM5 integrations were performed on a Western Canada Research Grid (Westgrid) SGI Origin using 48 processors and 48 gigabytes from a total of 256 gigabytes of main memory.

2.3 Results and Analysis

As in any climate simulation study, it is important to compare simulation results with observations if at all possible, in order to determine any model biases. Annually averaged temperature, precipitation rate, and wind field results for the control simulation, along with the long-term mean temperature, precipitation rate, and wind field patterns from NCEP Reanalysis Data (Kalnay *et al.*, 1996) are shown in Figures 2.1, 2.2 and 2.3 (respectively). Annually averaged temperature patterns are in reasonable agreement with NCEP Data (Fig. 2.1), with slightly colder temperatures simulated over the northern Himalayan region. Annually averaged precipitation patterns have considerable differences when compared to NCEP Data (Fig. 2.2), most notably the enhanced precipitation over the northwestern Indian Ocean as well as decreased precipitation over Southeast Asia. Precipitation rates do seem to be in agreement with NCEP Data over the northwestern Himalaya and northern India. Annually averaged wind field patterns also show considerable differences when compared to NCEP Data (Fig. 2.3), with an overall strengthening of winds across the entire domain (as seen from the difference in the plotted vector

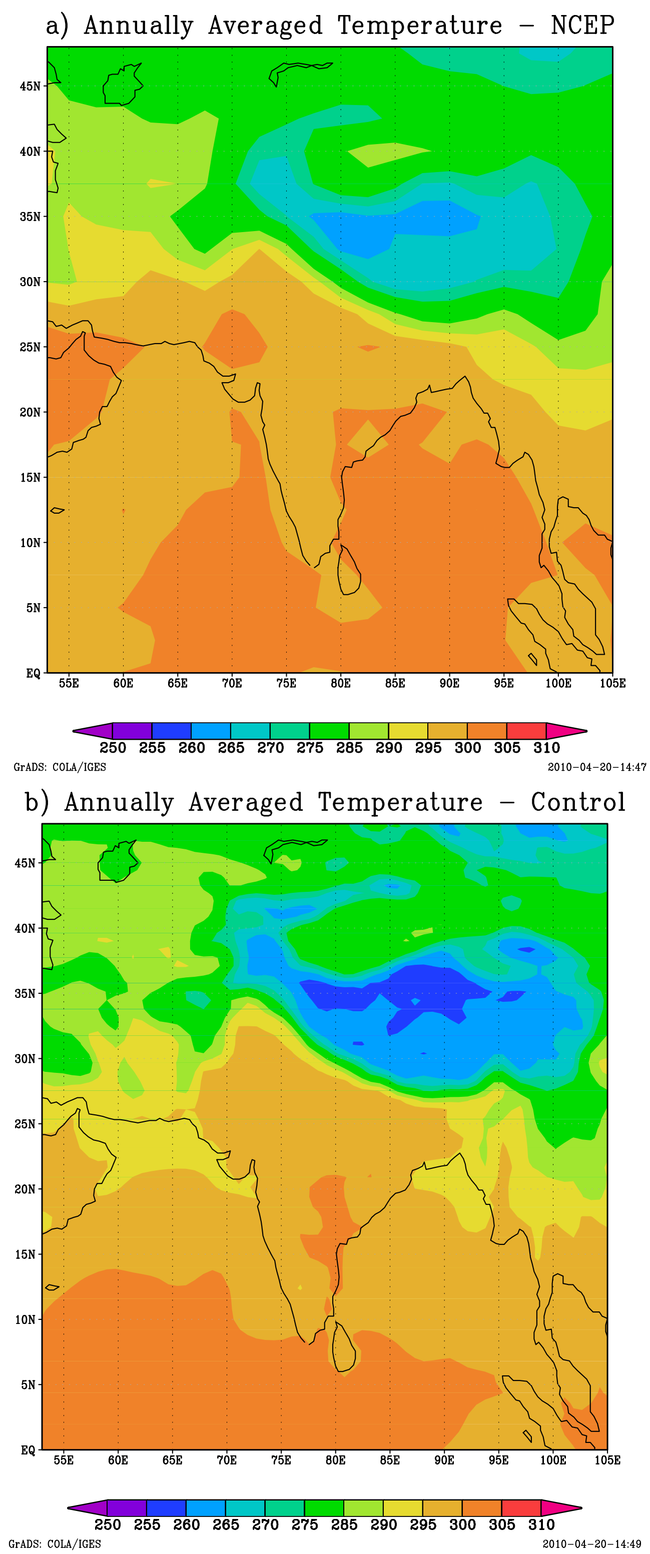

Figure 2.1: a) Annually averaged temperature (K) taken from NCEP Reanalysis Data. b) As in a), but for the Control simulation.

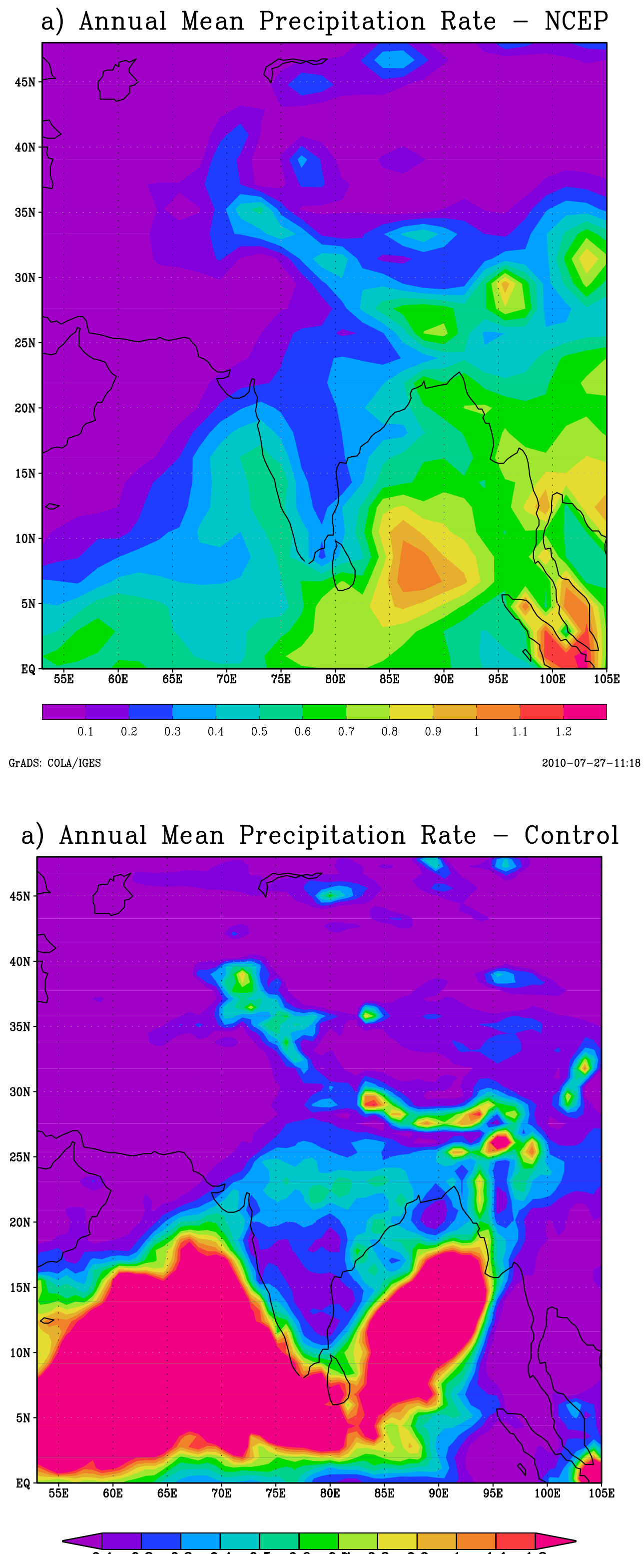

Figure 2.2: a) Annually averaged precipitation rate (kgm^2s^{-1}) taken from NCEP Reanalysis Data. b) As in a), but for the Control simulation.

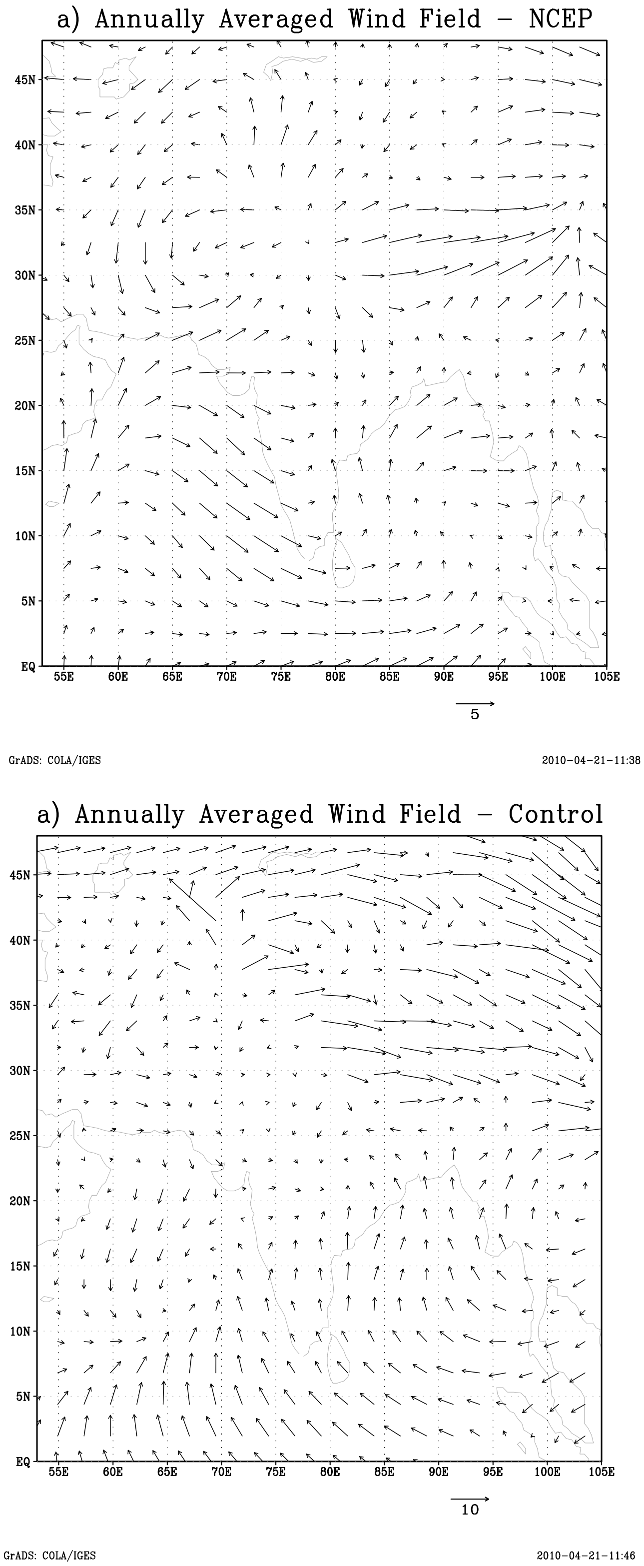

Figure 2.3: a) Annually averaged wind field (ms^{-1}) taken from NCEP Reanalysis Data. b) As in a), but for the Control simulation. Note the difference in vector scale between the two plots.

scale). The anticyclonic motion apparent in NCEP Data near 30-35°N and 65-70°E is captured in the MM5 results, as well as the westerly pattern near 30-35°N and 90-100°E.

Differences between the NCEP data and MM5 results obtained for the control simulation are likely arising from differences in model and data resolution. With a horizontal spatial resolution of approximately 210 km (Kalnay *et al.*, 1996), the NCEP data assimilation system is unable to accurately portray small scale variability in the fields under scrutinization. The enhanced precipitation seen over the Indian Ocean during the control simulation can also be attributed to increased convergence of the strengthened lower-level winds simulated by MM5 (c.f. Fig. 2.3).

2.3.1 Annual and Seasonal Results

Next, we investigate the evolution of climate variables through the 21st century. Figure 2.4 shows a steady increase in annually averaged near-surface temperatures, with differential warming between the continental interior and surrounding water mass arising from differences in specific heat capacity values for water (taken as 4186 $Jkg^{-1}K^{-1}$) and dry air (taken as 1004 $Jkg^{-1}K^{-1}$). By the end of the 21st century, simulated temperatures over water have increased by $\sim$1.5 K, whereas the highest amplitude of temperature increase over land is $\sim$4.5 K. Areas on the eastern side of the Tibetan Plateau, as well as to the north and south, experience the largest increase in temperature, with relatively smaller changes over Southern India and areas in which temperature changes are moderated by the presence of higher elevation, such as the frontal

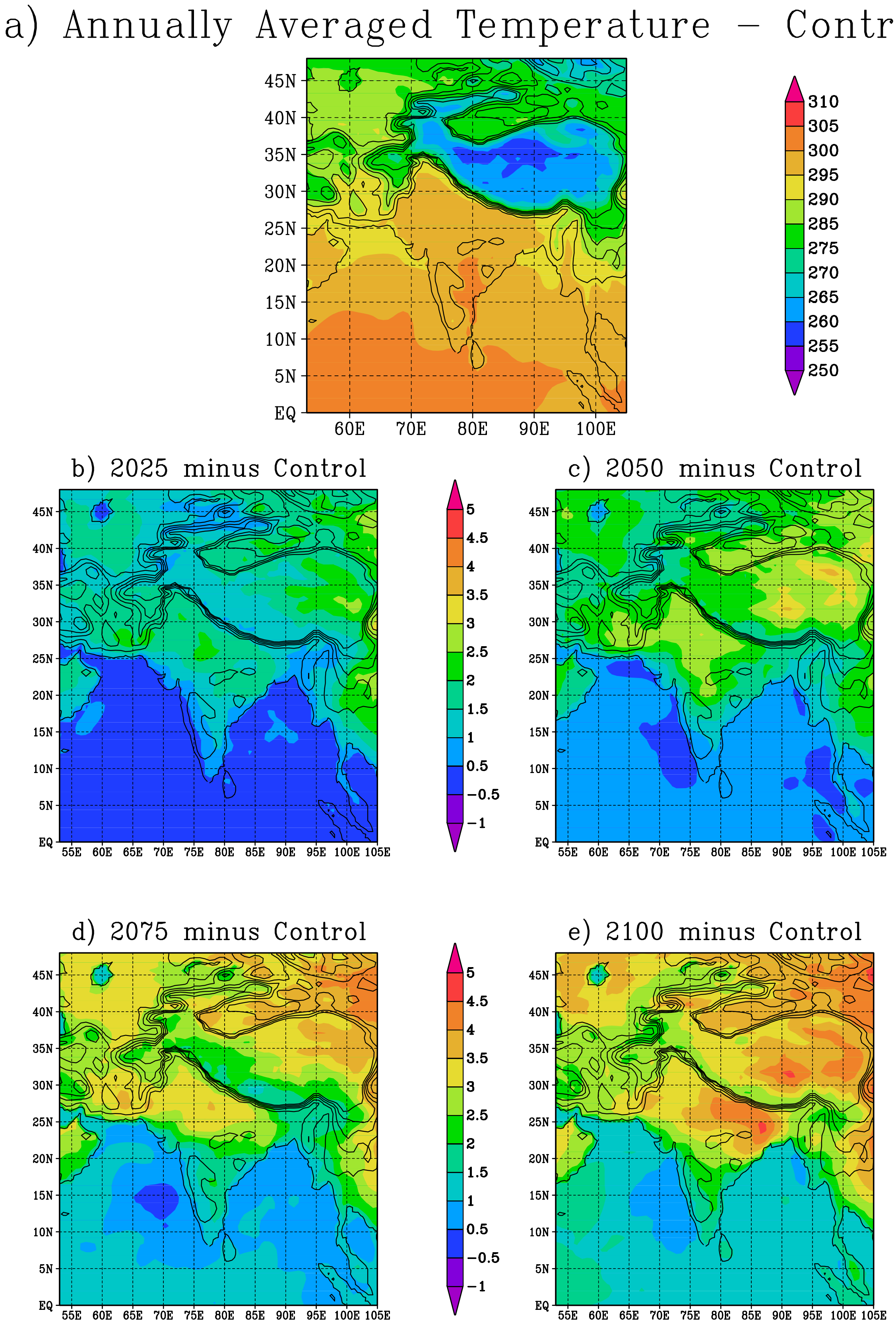

Figure 2.4: a) Annually averaged 2 metre temperature (K) for the Control simulation. b) As in a) but for 2025 minus Control. c) As in a) but for 2050 minus Control. d) As in a) but for 2075 minus Control. e) As in a) but for 2100 minus Control. Contour lines represent terrain.

and northwestern regions of the Himalaya.

With an increase in temperature, following equation (2.1), saturation vapour pressure will also increase, allowing the atmosphere to accumulate more water vapour before the occurrence of precipitation events. To investigate this relationship, we look at the evolution of near-surface atmospheric water vapour content through the 21st century (Fig. 2.5). By the end of the 21st century, the amount of water vapour per kilogram of dry air increases by over 8% in maritime regions, and by 16% throughout the Himalayan region. On the other hand, there is a considerable decrease in water vapour content over the Indian subcontinent in the 2025 and 2075 integrations, indicating a drying of the atmosphere in this region. The absence of this drying in the 2050 and 2100 integrations can be explained by the strength and direction of lower level wind anomalies in this region (c.f. Figs. 2.5b and 2.5d). In the 2025 and 2075 integrations, there is a more northwesterly component to lower level winds over the Indian subcontinent, suppressing the poleward transport of moisture from the Indian Ocean to India's interior. It has been stated in previous studies that an increase of atmospheric water vapour content has an effect on relative humidity, such that there are only slight variations in the evolution of relative humidity in a warming climate (Manabe & Wetherald, 1975; Ingram, 2002; Lorez & DeWeaver, 2007). Figure 2.6 portrays the evolution of surface relative humidity through the 21st century to be decreasing by roughly 4% over the dry Indian subcontinent, with minimal changes elsewhere in the domain.

Increases in atmospheric water vapour content imply an exaggeration of the hydrological cycle, in which areas that are usually in receipt of precipitation will experience an increase in precipitation, and areas in which evaporation oc-

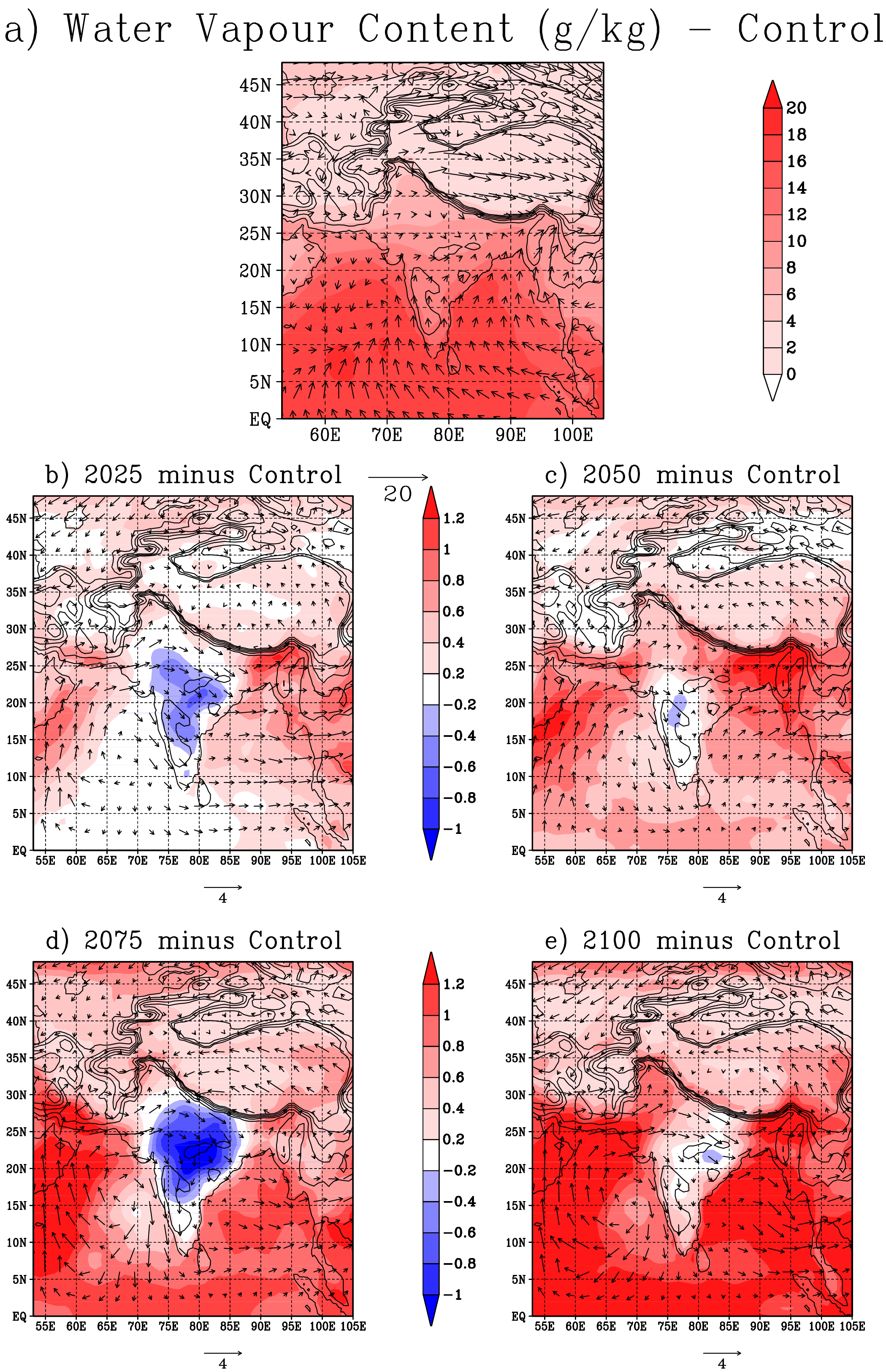

Figure 2.5: a) Annually averaged water vapour content (g/kg) at a 2 metre height, superimposed with lower level winds averaged over the lowest 8 σ levels (m/s) for the Control simulation. b) As in a) but for 2025 minus Control. c) As in a) but for 2050 minus Control. d) As in a) but for 2075 minus Control. e) As in a) but for 2100 minus Control. Contour lines represent terrain.

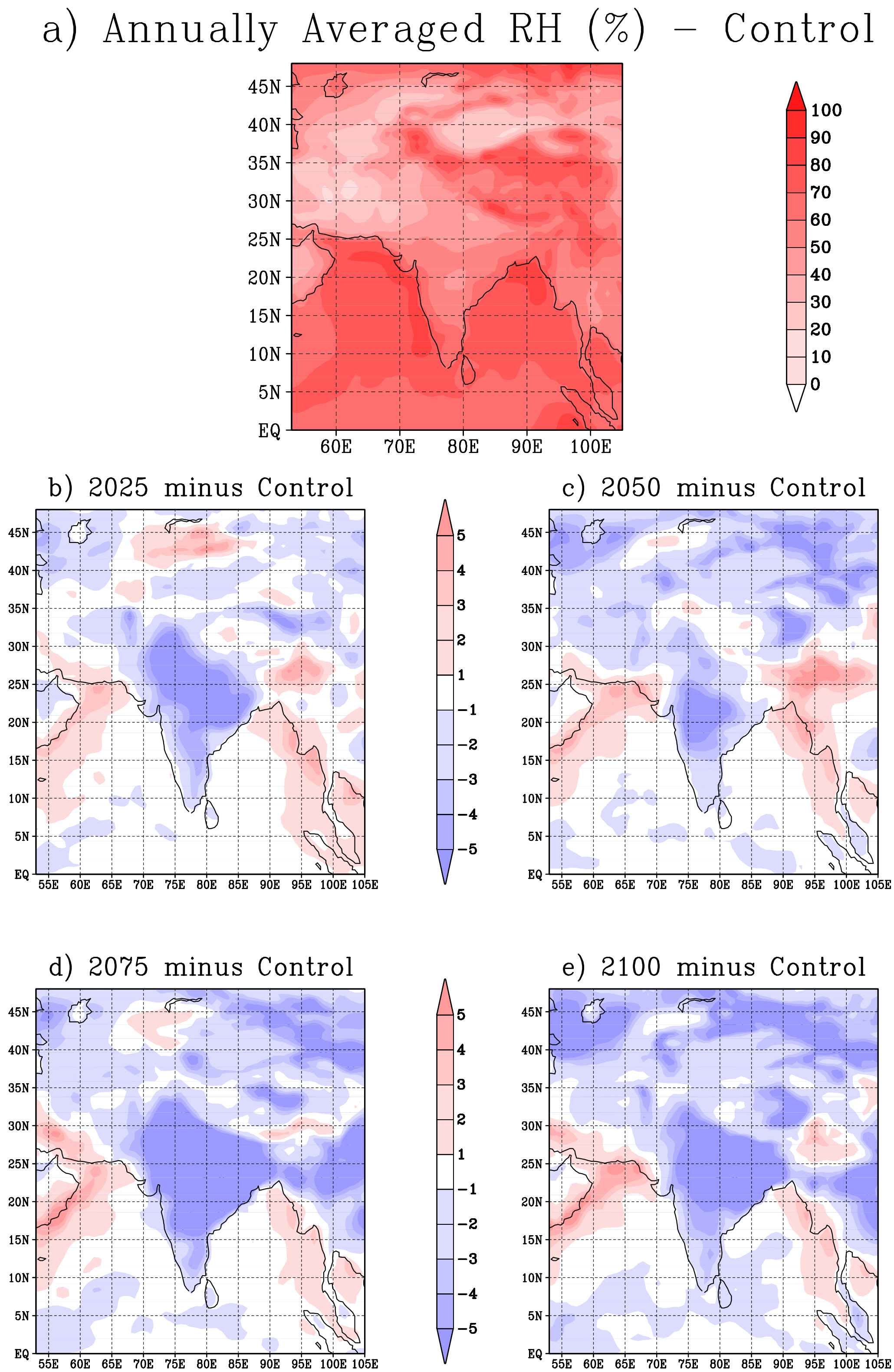

Figure 2.6: a) Annually averaged surface relative humidity (%) for the Control simulation. b) As in a) but for 2025 minus Control. c) As in a) but for 2050 minus Control. d) As in a) but for 2075 minus Control. e) As in a) but for 2100 minus Control.

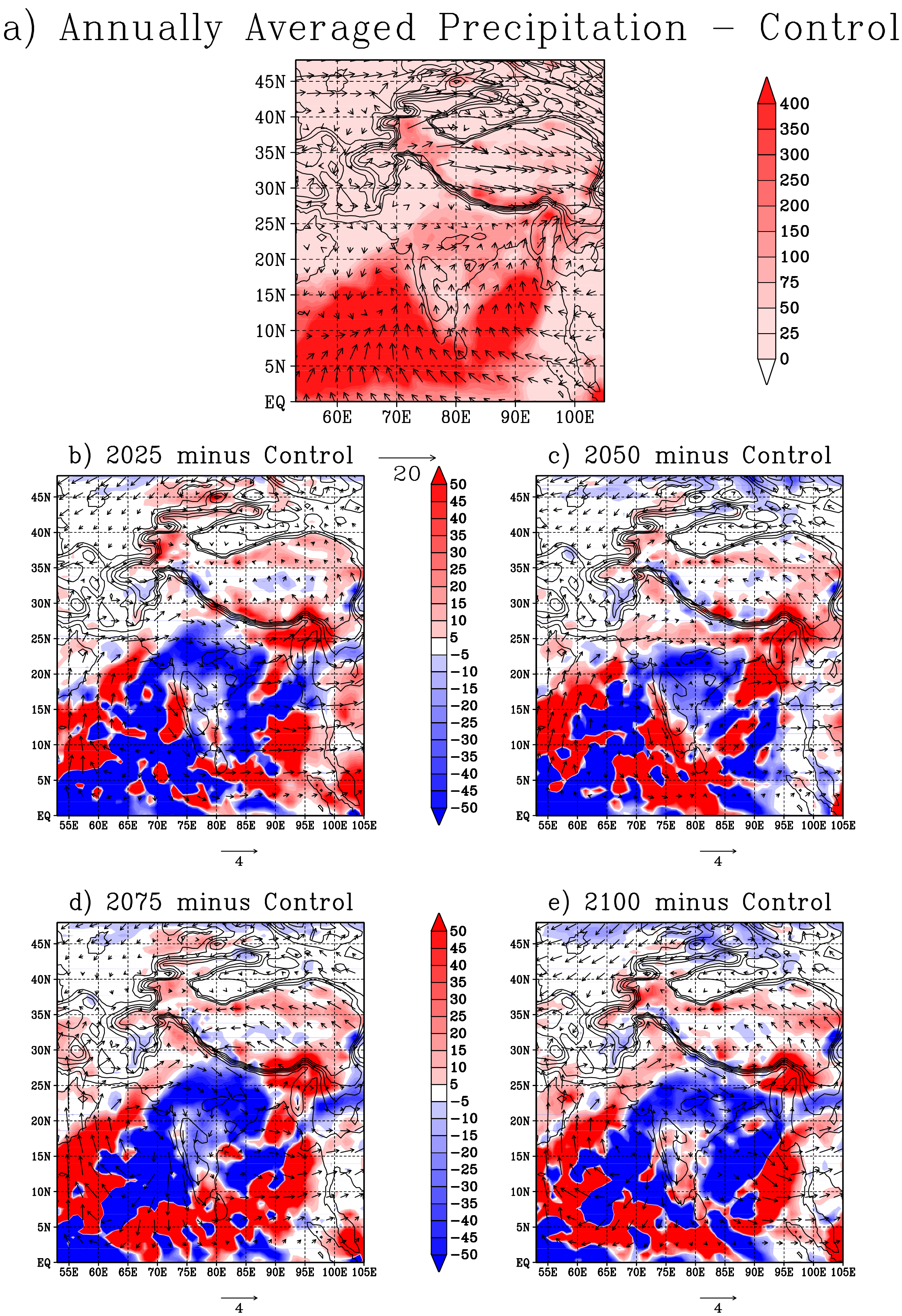

Figure 2.7: a) Annual mean total precipitation (cm) superimposed with lower level winds averaged over the lowest 8 σ levels (m/s) for the Control simulation. b) As in a) but for 2025 minus Control. c) As in a) but for 2050 minus Control. d) As in a) but for 2075 minus Control. e) As in a) but for 2100 minus Control. Contour lines represent terrain.

curs will see a decrease in precipitation. The intensification in evaporation is due to not only the increase in downward radiation resulting from an increase in atmospheric CO_2, but also a decrease in the Bowen ratio, which compares the energy available for upward sensible heat flux to the energy available for upward latent heat flux. A decrease in this ratio portrays the evaporation process as a more effective way of removing heat from Earth's surface than an upward flux of sensible heat, and is seen to be more significant over wetter maritime regions (Manabe & Wetherald, 1975). Figure 2.7 shows the evolution of results obtained for total precipitation for the 21st century. Oceanic areas show the most extreme increases and decreases in precipitation through the 21st century, which is expected with an intensification of the hydrological cycle since water masses experience vast amounts of both precipitation and evaporation. Along the Himalayan front, as well as throughout the Himalayan region, there is an increase in precipitation on the order of $\sim$20% over the eastern front, and a similar order of increase through areas in the Himalayan interior by the end of the 21st century. Comparing these values with the computed percentage increases in temperature, we obtain a sensitivity for precipitation of $\sim$1.25%/K over the Himalayan region, which is in agreement with the global-mean sensitivity of 1.4%/K calculated for a similar emission scenario in the study by Johns *et al.* (2003). There is a marked reduction in precipitation around 25°N over the Indian subcontinent, with increases in precipitation to the north and south, which indicates a northward shift of the rainbelt associated with the Intertropical Convergence Zone (ITCZ). This shift arises from enhanced poleward transport of warm, moist air from the subtropics to the mid-latitudes, as well as a northward shift of maximum zonal wind in the lower troposphere (the "jet stream"), which is a result of increasing temperatures related to increasing atmospheric CO_2 concentration (Manabe *et al.*, 1992).

To further validate our results, we investigate the evolution of soil moisture in the winter and summer months through the 21st century by averaging over four soil levels with a maximum depth of 1 m (Figs. 2.8 and 2.9). During the winter months of December, January and February (DJF), there is a marked decrease in soil moisture around 25°N over the Indian subcontinent (between 65°E and 95°E), with the exception of the 2050 simulation, with increases in soil moisture on either side of this latitude by the end of the 21st century (c.f. Fig. 2.8e). Areas of decreased soil moisture are clearly correlated with regions of decreased annual precipitation (c.f. Fig. 2.7), as well as regions of depressed annually averaged atmospheric water vapour content (c.f. Fig. 2.5). During the summer months of June, July and August (JJA), changes in soil moisture are very minimal, with extreme regional variability. The most notable change is located over Southeast Asia, in which initial increases in soil moisture are replaced with slight decreases by the end of the 21st century (c.f. Fig. 2.9).

In order to determine how large scale changes in the above mentioned climate variables will effect the Karakoram region in particular, we must first investigate the evolution of the influential climate dynamics of the region, which requires us to investigate the evolution of ENSO and NAO. As mentioned previously, the state of ENSO has a direct influence on the strength of the Asian summer monsoon winds and associated precipitation. Through investigation of sea surface temperatures (SSTs) within the GCM boundary conditions used in this project, the evolution of the state of the tropical Pacific Ocean can be interpreted (Fig. 2.10). Here, we are particularly interested in the Niño-3.4 region of the tropical Pacific Ocean (ranging from 5°N - 5°S

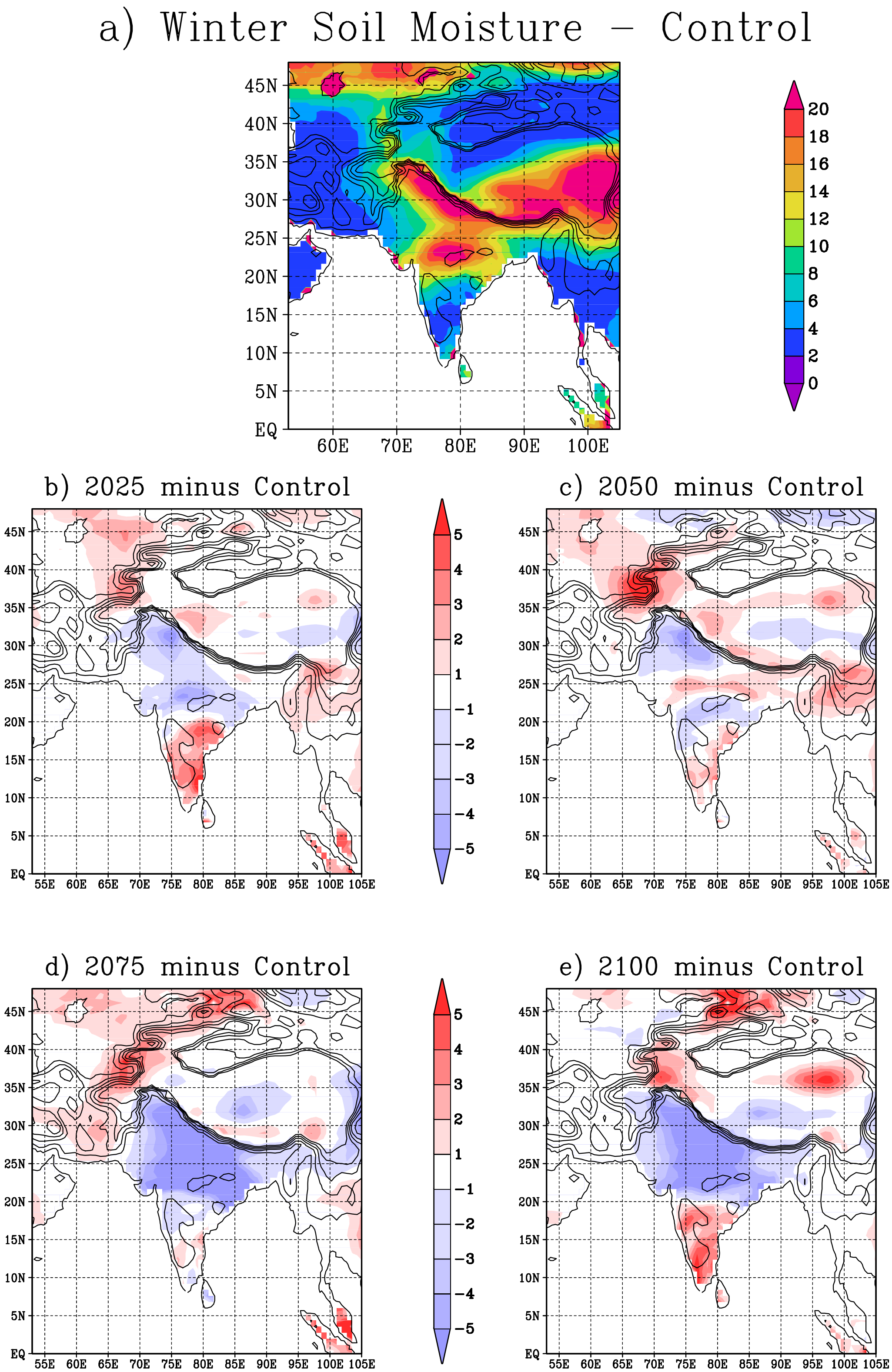

Figure 2.8: a) Soil moisture (cm water equivalent per month) averaged over DJF for the Control simulation. b) As in a) but for 2025 minus Control. c) As in a) but for 2050 minus Control. d) As in a) but for 2075 minus Control. e) As in a) but for 2100 minus Control. Contour lines represent terrain.

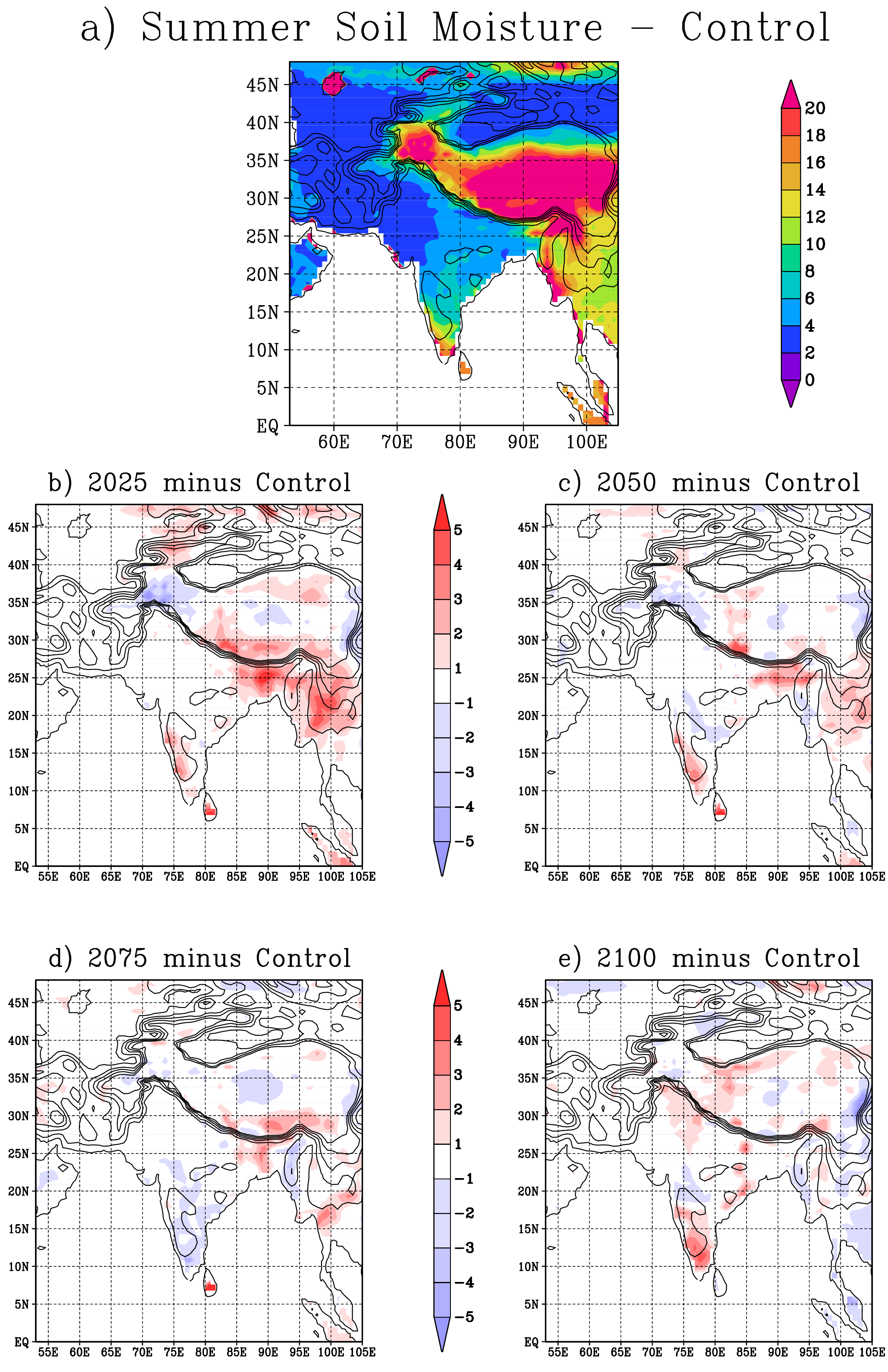

Figure 2.9: a) Soil moisture (cm water equivalent per month) averaged over JJA for the Control simulation. b) As in a) but for 2025 minus Control. c) As in a) but for 2050 minus Control. d) As in a) but for 2075 minus Control. e) As in a) but for 2100 minus Control. Contour lines represent terrain.

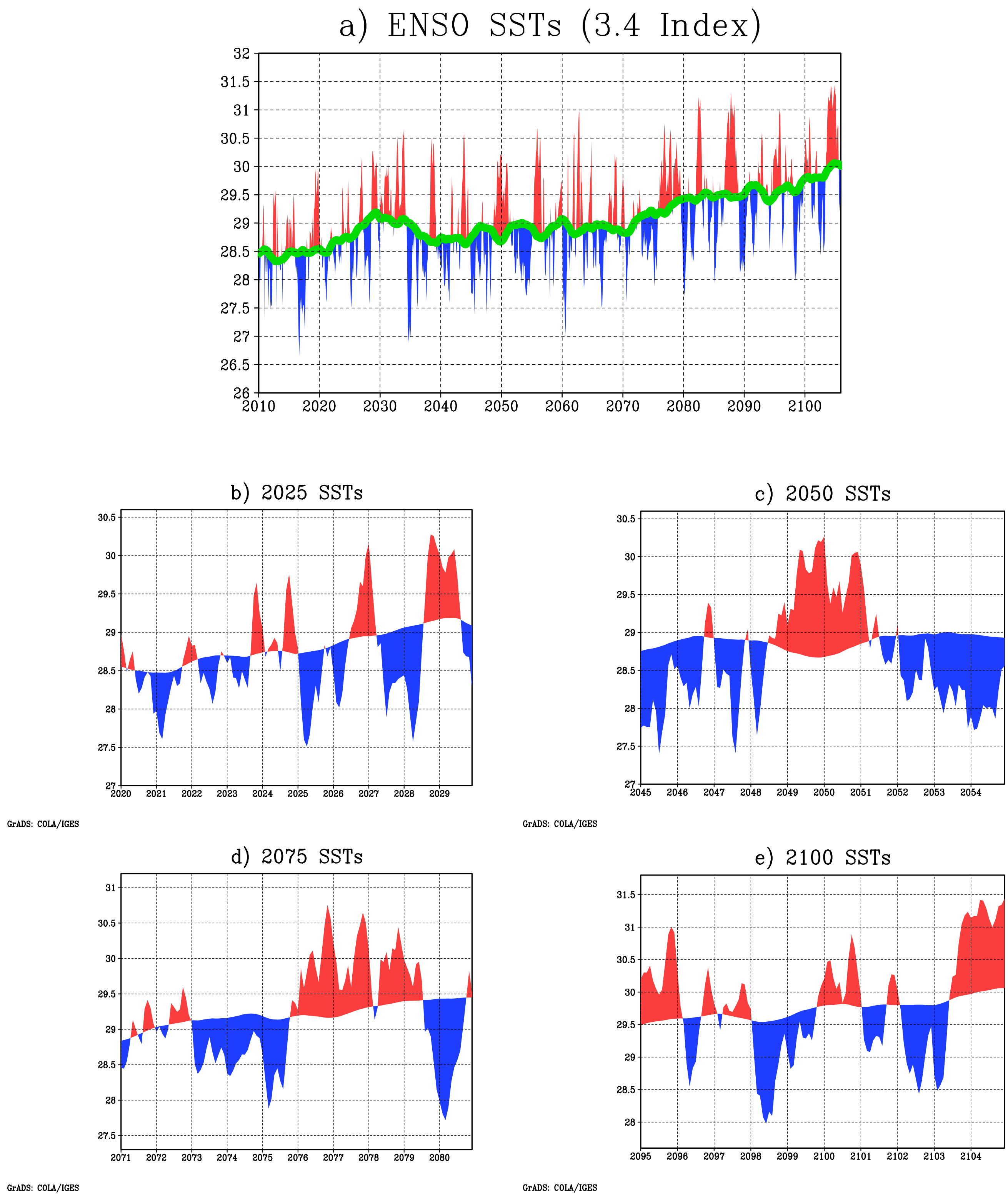

Figure 2.10: a) Sea surface temperatures (°C) superimposed with a 10-year running mean (in green) for the ENSO 3.4 region spanning the 21st century. b) A closer look at SSTs, superimposed with a 10-year running mean, surrounding 2025. c) As in b) but for 2050. d) As in b) but for 2075. e) As in b) but for 2100.

and 120°- 170°W), which is known to be a more sensitive indicator to changes in ENSO behaviour under a changing climate (Trenberth, 1997; Bush, 2007). SSTs averaged over this region are then subtracted from a 10-year running mean in order to obtain SST anomalies for each time slice calculation. It is clear that under anthropogenic forcing, SSTs steadily increase from 28.5°C to roughly 30°C by the end of the 21st century (c.f. Fig. 2.10a). In order to determine whether this increase in SSTs is solely due to increasing global temperatures or a shift towards a more El Niño-like state of the tropical Pacific Ocean, we must also investigate fluctuations in other ENSO-defining variables, such as sea level pressure and equatorial trade wind strength (Fig. 2.11). Following the method used in Vecchi *et al.* (2006), the sea level pressure (SLP) gradient between averaging areas in the eastern and western tropical Pacific Ocean is calculated by performing a 6-month running mean which is then subtracted from a 5-year running mean to reduce seasonal and annual variability. A decreasing SLP gradient implies a weakening of the Walker circulation pattern, and hence a shift towards an El Niño-like state. Figure 2.11a shows a distinctive decrease in SLP gradient surrounding 2030, which correlates with the simulated El Niño event at this time (c.f. Fig. 2.10a), after which a slight decrease in SLP is apparent through the end of the simulation. During times of suppressed Walker circulation, a weakening of the easterly trade winds near the equator is expected. Figure 2.11b shows a 10-year running mean of the zonal wind strength, averaged over the area enclosed in the blue box, which indicates a strong weakening of trade wind strength surrounding 2030, which again correlates with the simulated El Niño event at this time (c.f. Fig. 2.10a), after which an overall weakening in trade wind strength is seen by the end of the 21st century. Both of the above results concur with the suggestion of a shift towards a more El Niño-like state of the tropical Pacific Ocean with increasing atmospheric CO_2 concentration.

When solely considering the impacts of ENSO teleconnections, a shift towards an El Niño-like state of the Pacific Ocean correlates with an increasingly positive NAO phase (Visbeck *et al.*, 2001), however when considering the effects of steadily increasing global temperatures, one would expect a shift towards a negative NAO phase due to a decreasing sea level pressure gradient between the Icelandic low and the Azores high. Through further investigation of our GCM boundary conditions, the phase of NAO is found to be more positive initially, but less positive by the end of the 21st century (c.f. Fig. 2.12). With an increasingly positive NAO phase, one would expect the SLP gradient between the Icelandic Low and the Azores High to similarly increase, which is not the case here (c.f. Fig. 2.12a). While there is an increase in SLP gradient until approximately 2070, the sharp decrease thereafter suggests a dominance of the NAO response to climate warming over the NAO teleconnections with ENSO in the 21st century. The strength of the associated westerlies is shown in Figure 2.12b, and while it does agree very well with results for SLP gradient (these two factors should be positively correlated), it again does not agree with a steadily strengthening NAO circulation pattern related to a more El Niño-like state of the Pacific Ocean, suggesting the importance of global temperature increases on NAO variability and evolution during the 21st century.

Correlating with the above-mentioned evolution of ENSO through the 21st century, a weakening of the Asian summer monsoon is expected. Figure 2.13 shows the evolution of lower level winds averaged over the summer months of June, July and August. A significant weakening of the summer monsoon winds is not apparent until the 2075 simulation (c.f. Fig. 2.13d), with only slight

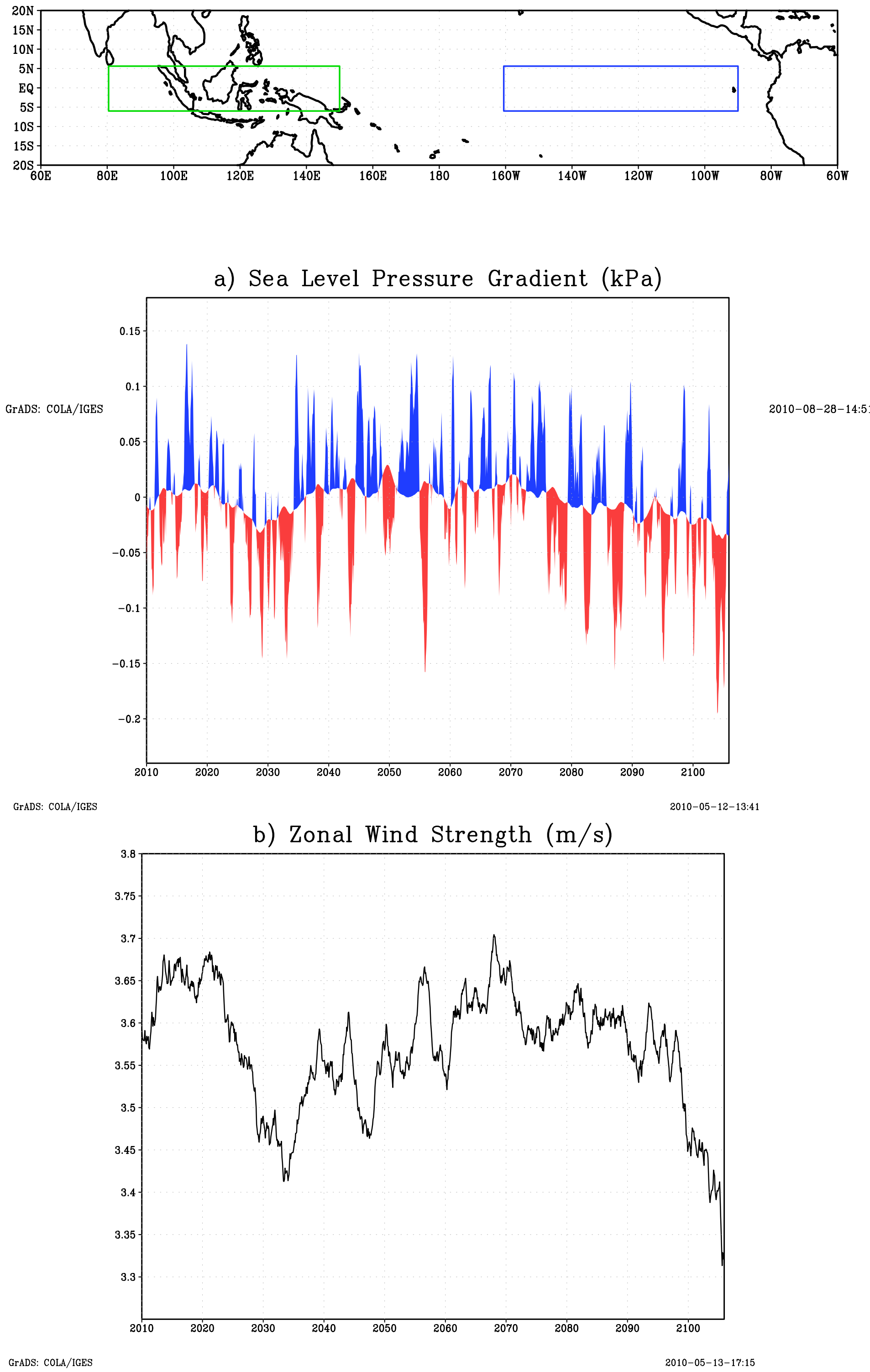

Figure 2.11: (Top Image) Averaging areas for plots below. a) 6-month running mean SLP gradient (kPa, blue box minus green box) deviation from a 10-year running mean. b) 5-year running mean zonal wind strength averaged over the blue box in the top image.

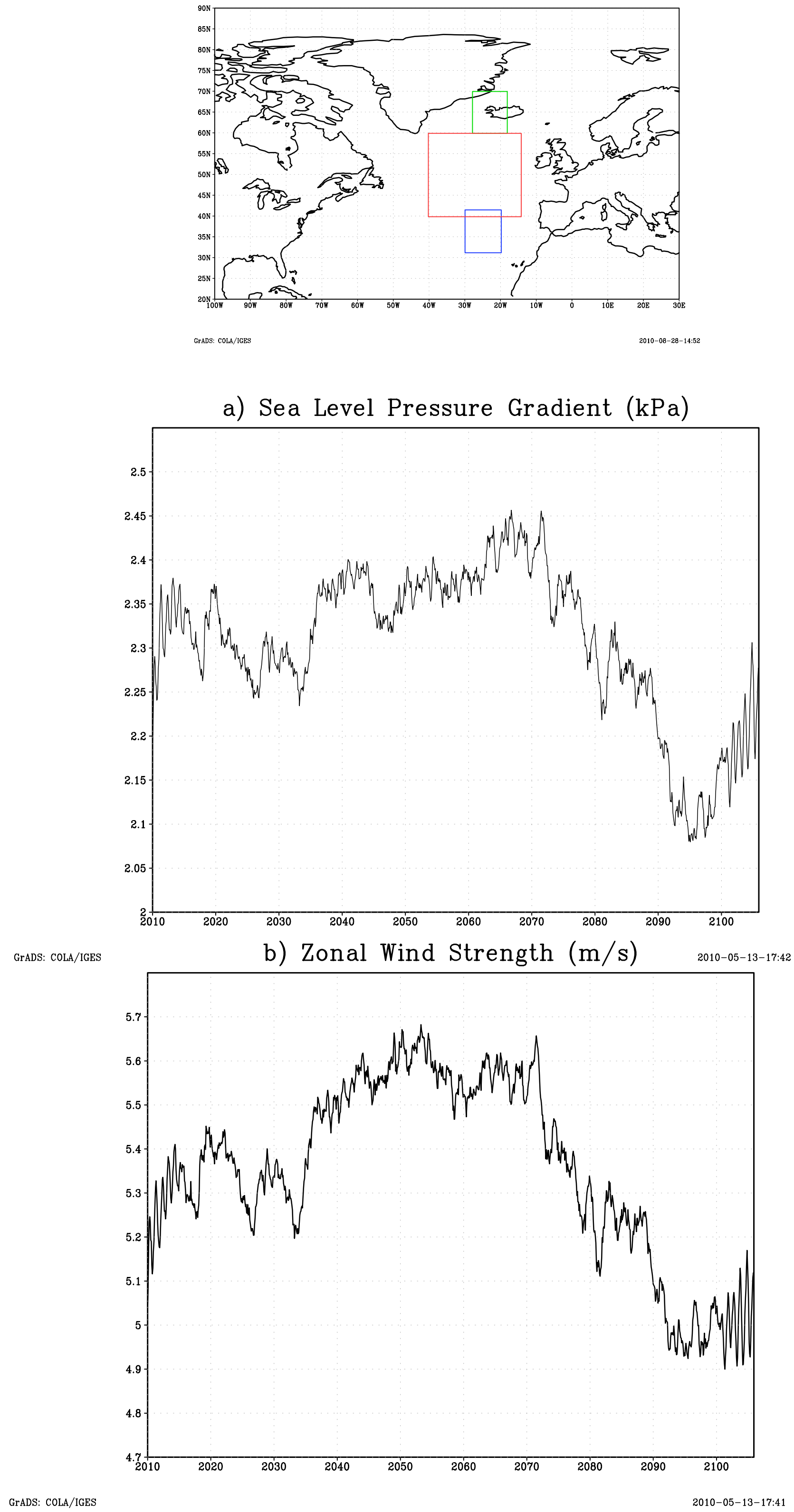

Figure 2.12: (Top Image) Averaging areas for plots below. a) 5-year running mean SLP gradient (kPa, blue box minus green box). b) 5-year running mean zonal wind strength averaged over the red box in the top image.

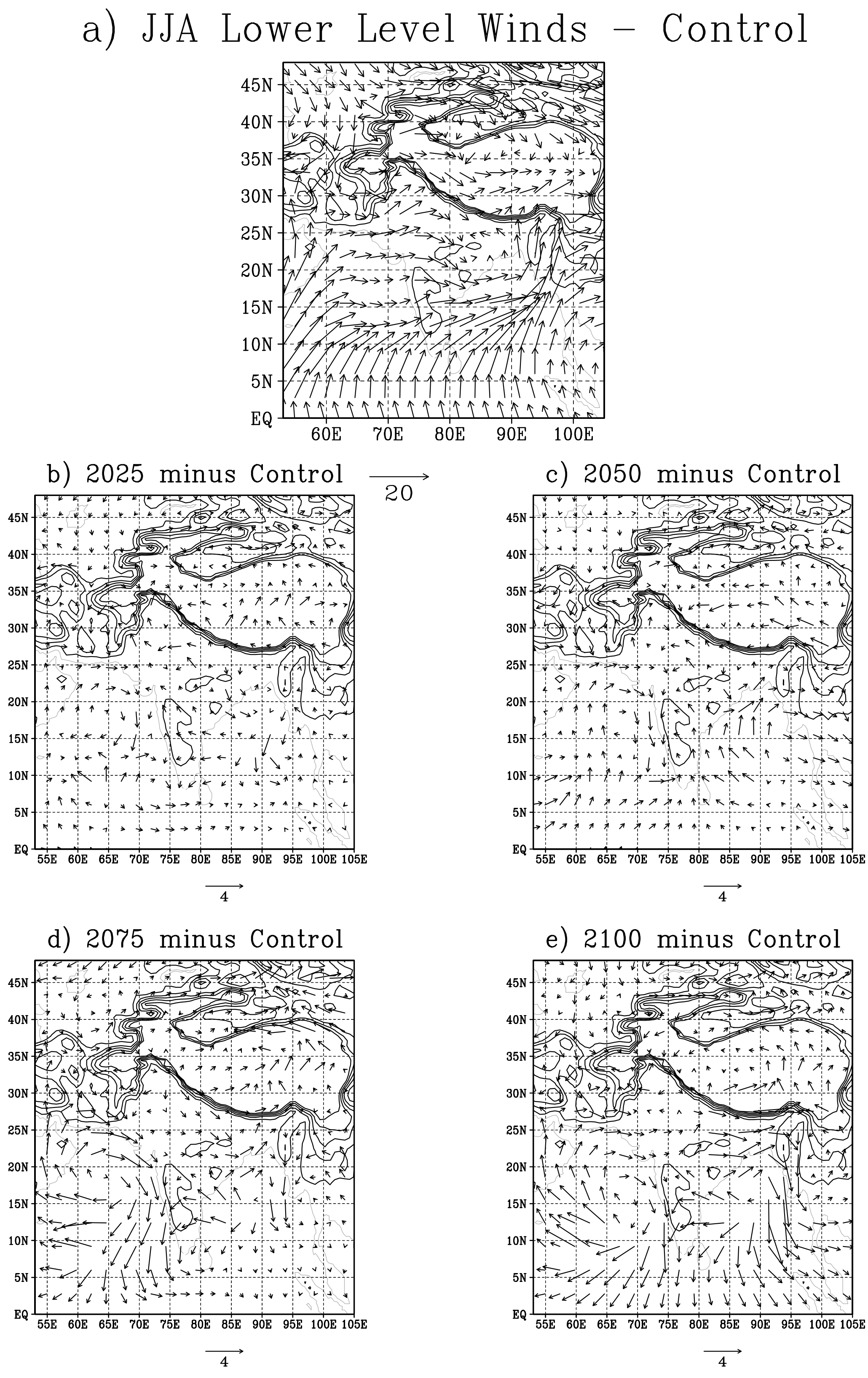

Figure 2.13: a) JJA lower level winds (m/s), averaged over the lowest 8 σ levels, for the Control simulation. b) As in a), but for 2025 minus Control. c) As in a), but for 2050 minus Control. d) As in a), but for 2075 minus Control. e) As in a), but for 2100 minus Control. Contour lines represent terrain.

variations occurring before this time. This is in agreement with the evolution of ENSO presented above, in which the decreases in SLP gradient and zonal wind strength are not apparent until approximately 2080 (c.f. Fig. 2.11a and 2.11b). An overall weakening of the Asian summer monsoon will decrease the frequency of monsoon intrusions into the Karakoram region, therefore altering the Karakoram's accumulated summer precipitation.

In order to fully understand the implications of an increasingly warmer climate on glaciers in the Karakoram region, we must investigate the seasonality of the simulated temperature changes presented in this study over the second model domain (Figs. 2.14 - 2.17). Figure 2.14 suggests that the majority of the annual mean temperature increase (c.f. Fig. 2.4) occurs in the spring months of March, April and May (MAM), with an increase of over 8 K seen in the lower elevation regions surrounding the Tibetan plateau. However, these temperature increases are not large enough to allow for a transition in precipitation type from snow to rain in the high-elevated areas of the Karakoram region. Temperature changes over the months of June, July and August (JJA) are minimal over the northwestern Himalaya, with low elevation areas experiencing an initial decrease in surface temperature followed by slight increases by the 2100 simulation (Fig. 2.15). Initially, temperature anomalies for the months of September, October and November (SON) are shown to decrease for some regions in the 2025 integration, but show increases of ~ 3 K in the 2100 simulation (Fig. 2.16). Temperature changes over the months of December, January and February (DJF) show a considerable decrease in temperature over the majority of the western Himalaya for the 2025 and 2075 integrations, with only a slight overall increase by the end of the 21st century (Fig. 2.17). There is evidence of an elevation dependency of temperature

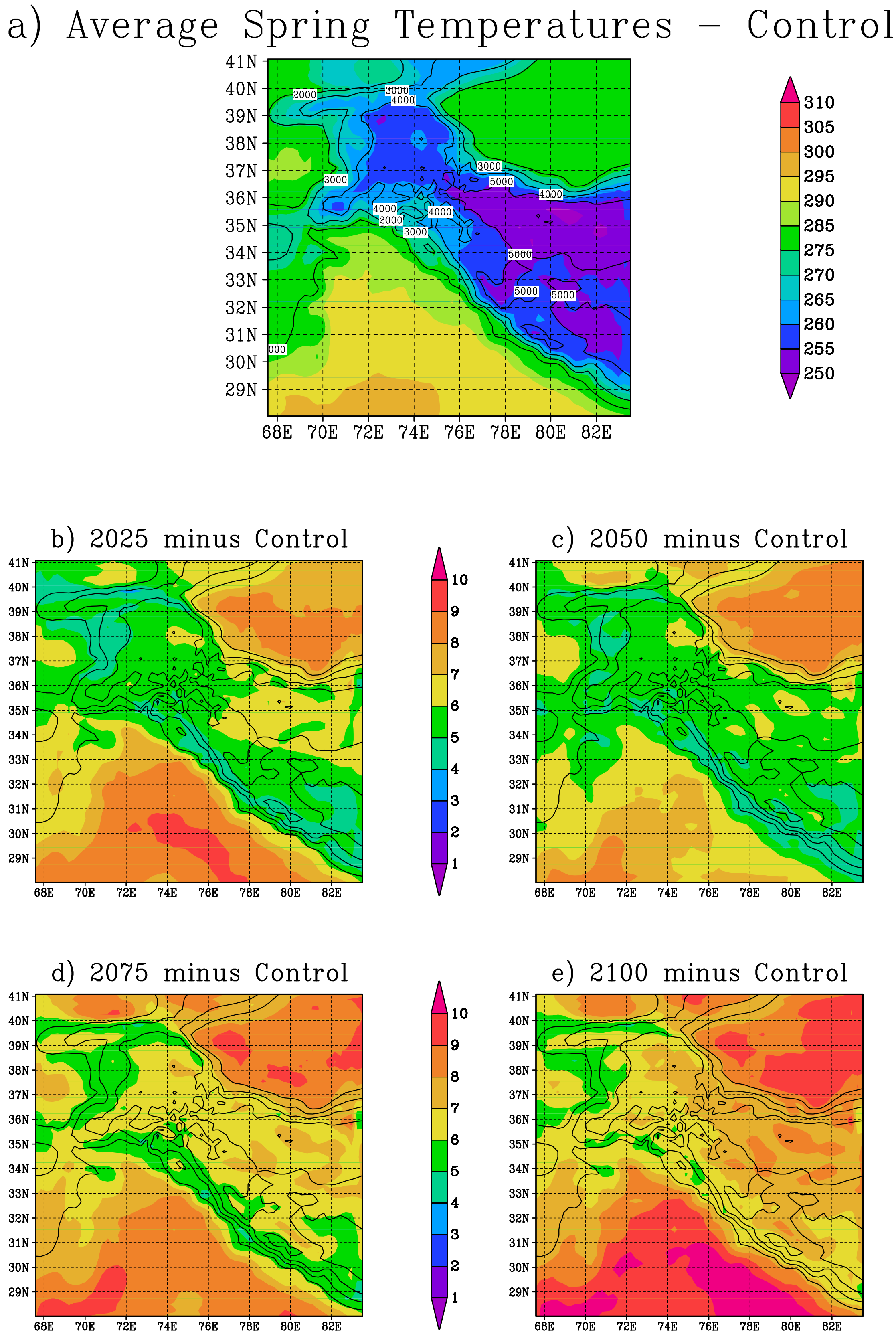

Figure 2.14: a) Surface temperature (K) averaged over the MAM period for the Control simulation. b) As in a) but for 2025 minus Control. c) As in a) but for 2050 minus Control. d) As in a) but for 2075 minus Control. e) As in a) but for 2100 minus Control. Contour lines represent terrain, which are labelled in image a).

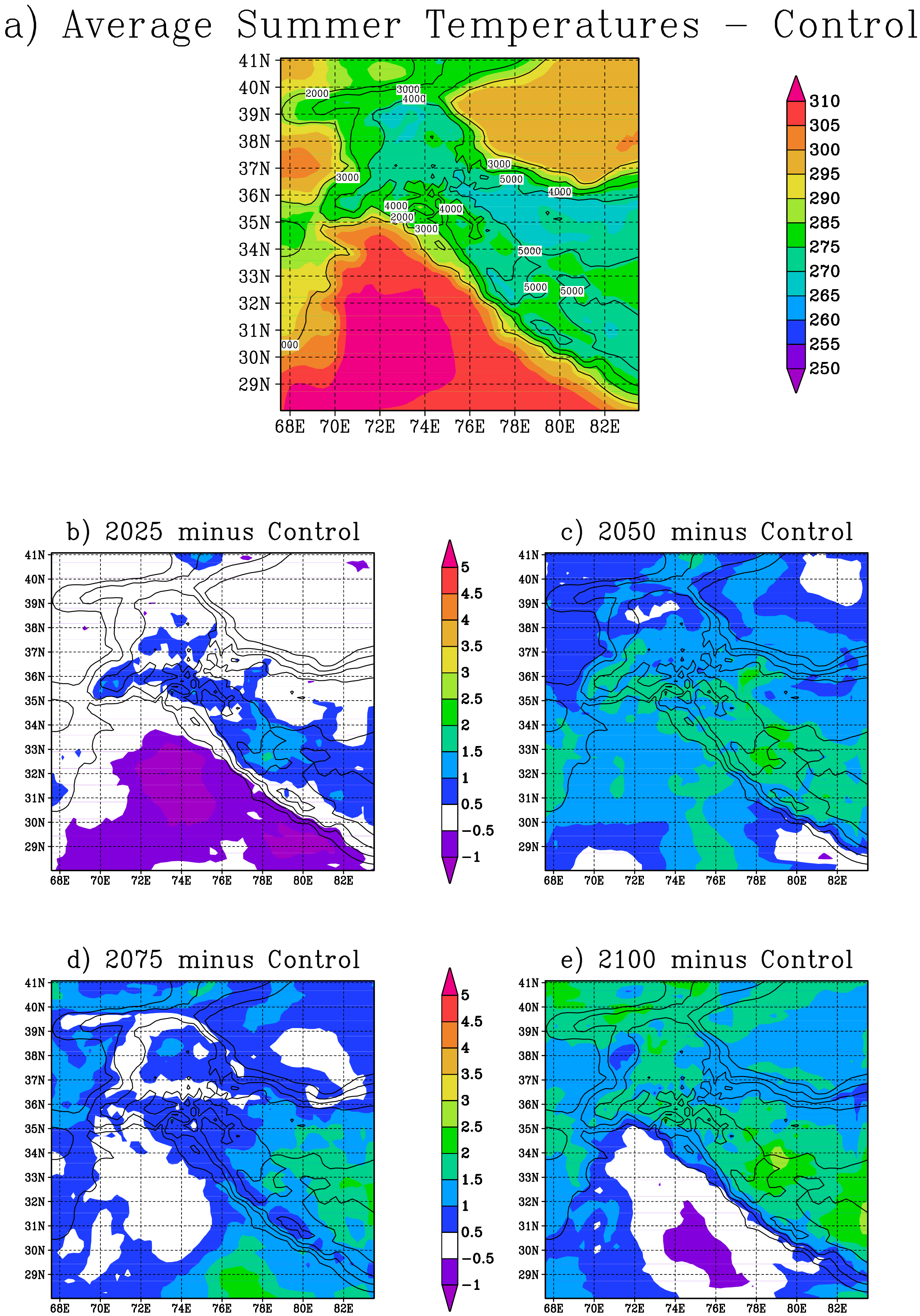

Figure 2.15: a) Surface temperature (K) averaged over the JJA period for the Control simulation. b) As in a) but for 2025 minus Control. c) As in a) but for 2050 minus Control. d) As in a) but for 2075 minus Control. e) As in a) but for 2100 minus Control.

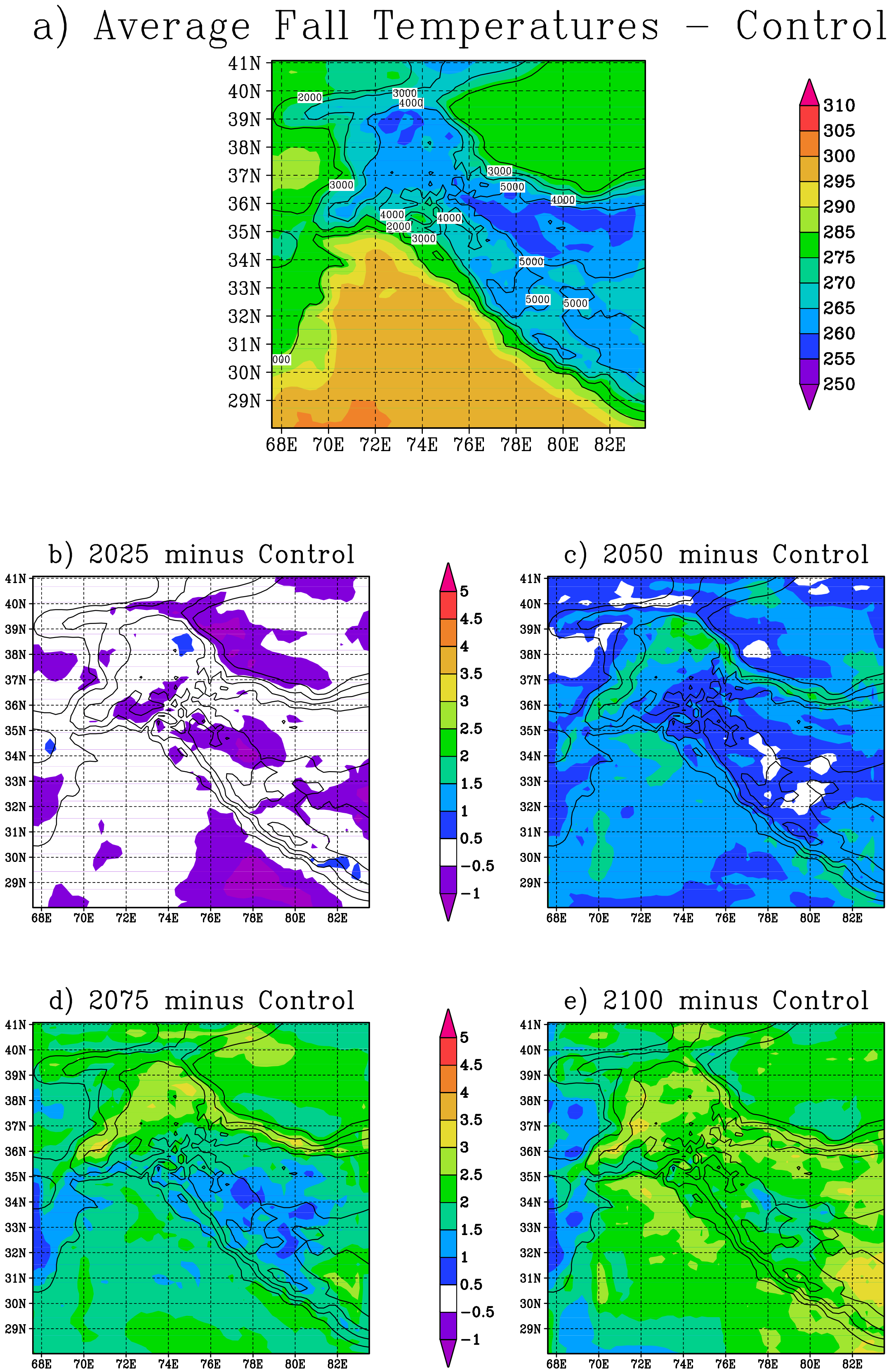

Figure 2.16: a) Surface temperature (K) averaged over the SON period for the Control simulation. b) As in a) but for 2025 minus Control. c) As in a) but for 2050 minus Control. d) As in a) but for 2075 minus Control. e) As in a) but for 2100 minus Control.

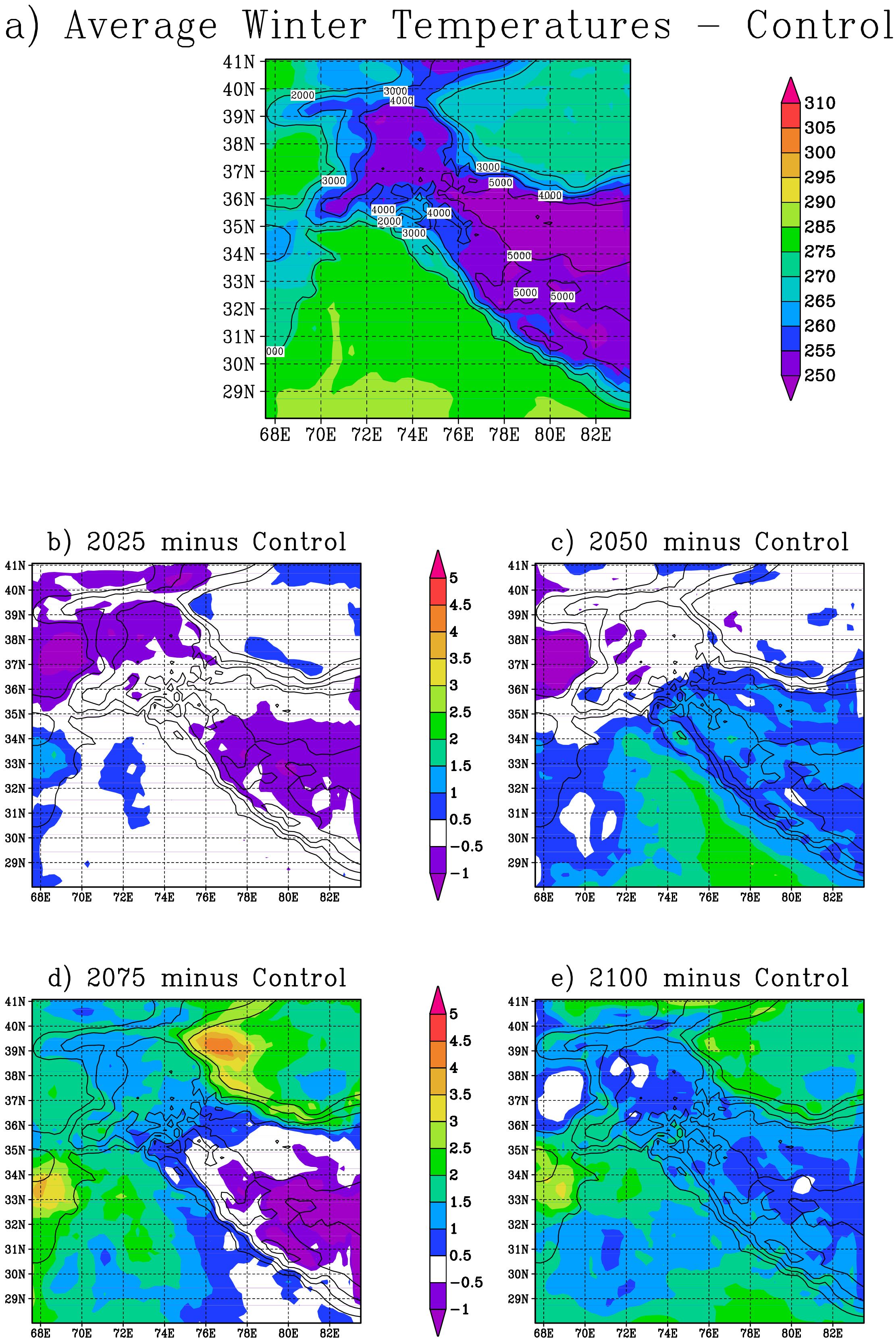

Figure 2.17: a) Surface temperature (K) averaged over the DJF period for the Control simulation. b) As in a) but for 2025 minus Control. c) As in a) but for 2050 minus Control. d) As in a) but for 2075 minus Control. e) As in a) but for 2100 minus Control.

fluctuations in all months by the end of the 21st century (c.f. Figs. 2.14e, 2.15e, 2.16e and 2.17e), most of which is located above the 5000 m elevation level, on the eastern side of the domain displayed in the previously mentioned figures, however this dependency is least apparent in the winter months, when warming at higher elevations is less than at surrounding lower elevations by the end of the 21st century.

As mentioned previously, the Karakoram region is under the influence of two very distinct climate patterns, the relative contributions of which need to be compared in order to determine their influence on glacial mass balance in the region. As shown in Figure 2.18, the Karakoram region experiences intrusions of the summer monsoon winds from the south, as well as persistent westerly winds originating over the Mediterranean and Caspian Seas. The difference in air temperature between the westerly and monsoonal flow is on the order of 10°C during the entire century-long simulation, implying that when monsoon flow is diminished, which occurs during ENSO conditions, the colder westerlies are the dominant air flow into the Karakoram region. During the peak summer monsoon months of July and August, we compare the influence of each of these climate patterns by dividing the zonal component of the midlatitude westerlies, averaged over Box 1 in Figure 2.18, by the meridional component of summer monsoon flow, averaged over Box 2 in Figure 2.18 (herein denoted as the Westerly Index, as seen in the works of S. Emily Collier, personal communication). A computed value for this index is found for each time period of integration, and is given in Table 2.1.

Higher computed values for the Westerly Index indicate a weaker input of the monsoonal flow, allowing for cooler temperatures to arise in the Karako-

Table 2.1: Calculated values of the Westerly Index for the 21st century

Time Period	Westerly Index Value
Control	0.797
2025	0.776
2050	0.519
2075	1.006
2100	0.788

ram region, at which point an increase in snowfall accumulation is expected. Smaller values indicate a stronger monsoonal flow influence carrying warmer temperatures into the region, at which point decreased snowfall accumulation is expected. Table 2.1 suggests that a linear evolutionary trend of the Westerly Index does not exist within our simulated results, thus it is necessary to investigate the evolution in mean July-August wind strength and direction through the 21st century (Fig. 2.19). The 2025 simulation has a Westerly Index value slightly less than that of the Control simulation, implying a slightly greater influence of the summer monsoon winds, which can be seen to the southwest of the study region in Figure 2.19b. During the 2050 simulation, a much stronger influence of the summer monsoon winds can be seen directly to the south of the study region (c.f. Figure 2.19c), which is in agreement with the much smaller Westerly Index value computed in Table 2.1. The Westerly Index value computed for the 2075 simulation suggests a drastic shift towards a more westerly dominated air flow, which concurs with Figure 2.19d, in which there is a diminished influence of the monsoonal flow to the south of the study region. By the end of the 21st century, the Westerly Index suggests either a reduction in influence of the westerlies or strengthening of the monsoon. This is slightly unexpected, as with decreasing summer monsoon wind strength suggested for the 21st century (c.f. Fig 2.13) an ever increasing Westerly Index would be the expected outcome. However, the wind anomalies portrayed in Figure 2.19e do

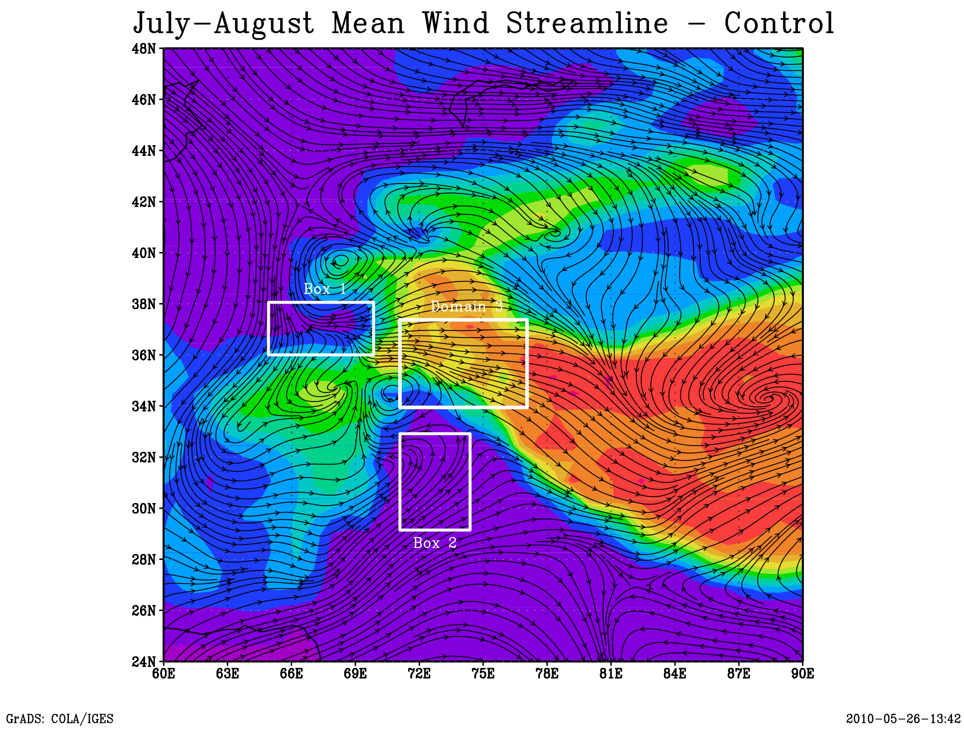

Figure 2.18: a) July-August mean wind streamline averaged over the lowest 8 σ levels. The 3 outlined boxes indicate the location of the study region (Domain 3), as well as the averaging areas of the westerly (Box 1) and monsoon (Box 2) influence on the study region.

in fact suggest a weakening of the summer monsoon flow, thus a decrease in the Westerly Index from 2075 to 2100 can only be explained by a weakening of the westerly flow into the region, which is confirmed to the west of the study region in Figure 2.19e, and is expected during a time of decreasing NAO phase (c.f. Fig. 2.12).

The seasonal temperature fluctuations (c.f. Figs. 2.14 - 2.17), coupled with changes in regional circulation patterns mentioned above, could have a detrimental effect on alpine glaciers in the Karakoram region, pending that temperature changes allow for a transition from below to above freezing level, during which received precipitation would fall as glacier-diminishing rain, instead of glacier-nourishing snow. It is therefore imperative to investigate the seasonal accumulation of all types of precipitation to determine the signifi-

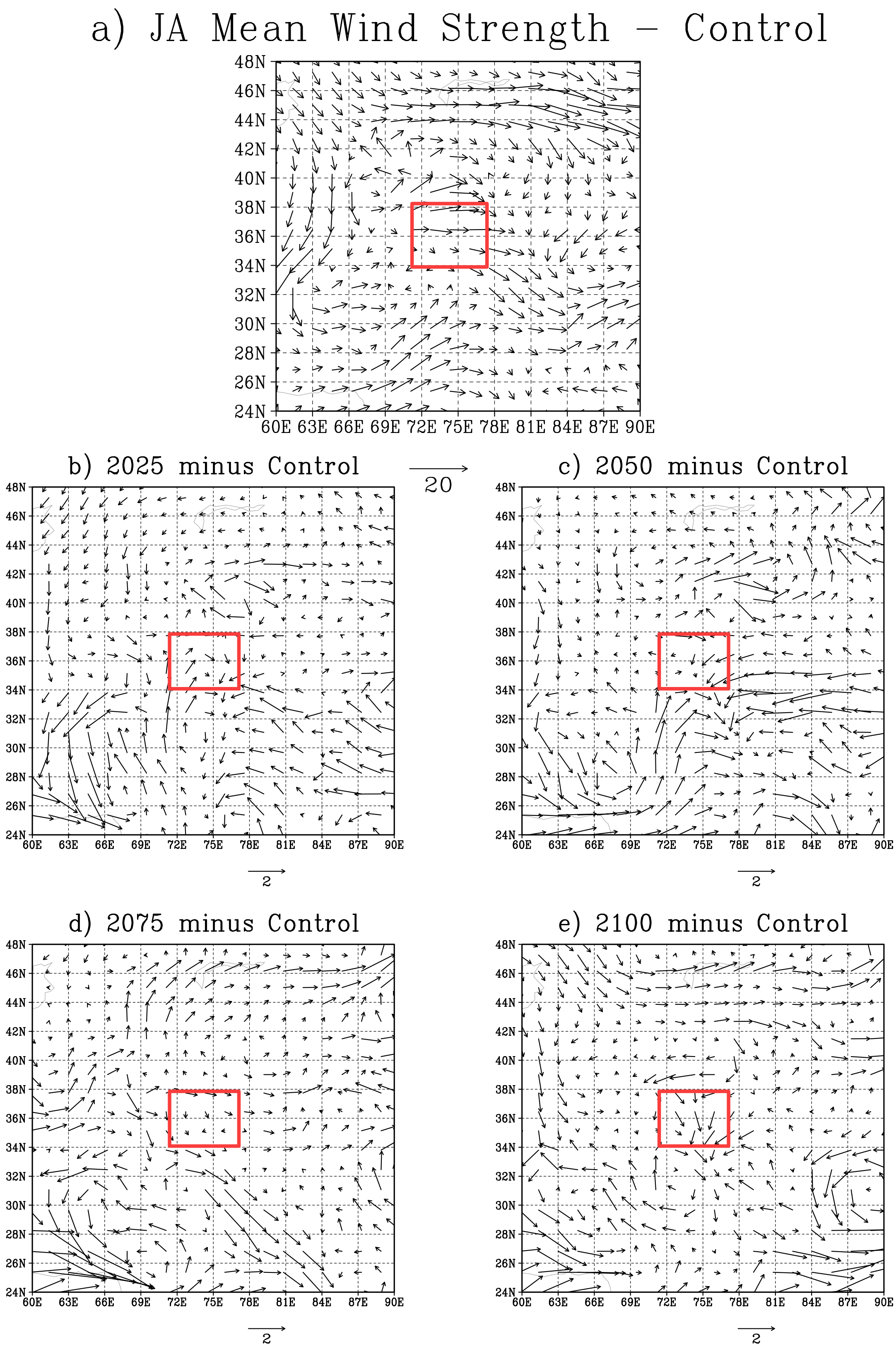

Figure 2.19: a) July-August mean wind strength averaged over the lowest 8 σ levels.b) As in a), but for 2025 minus Control. c) As in a), but for 2050 minus Control. d) As in a), but for 2075 minus Control. e) As in a), but for 2100 minus Control. Red boxes indicate the study region (Domain 3).

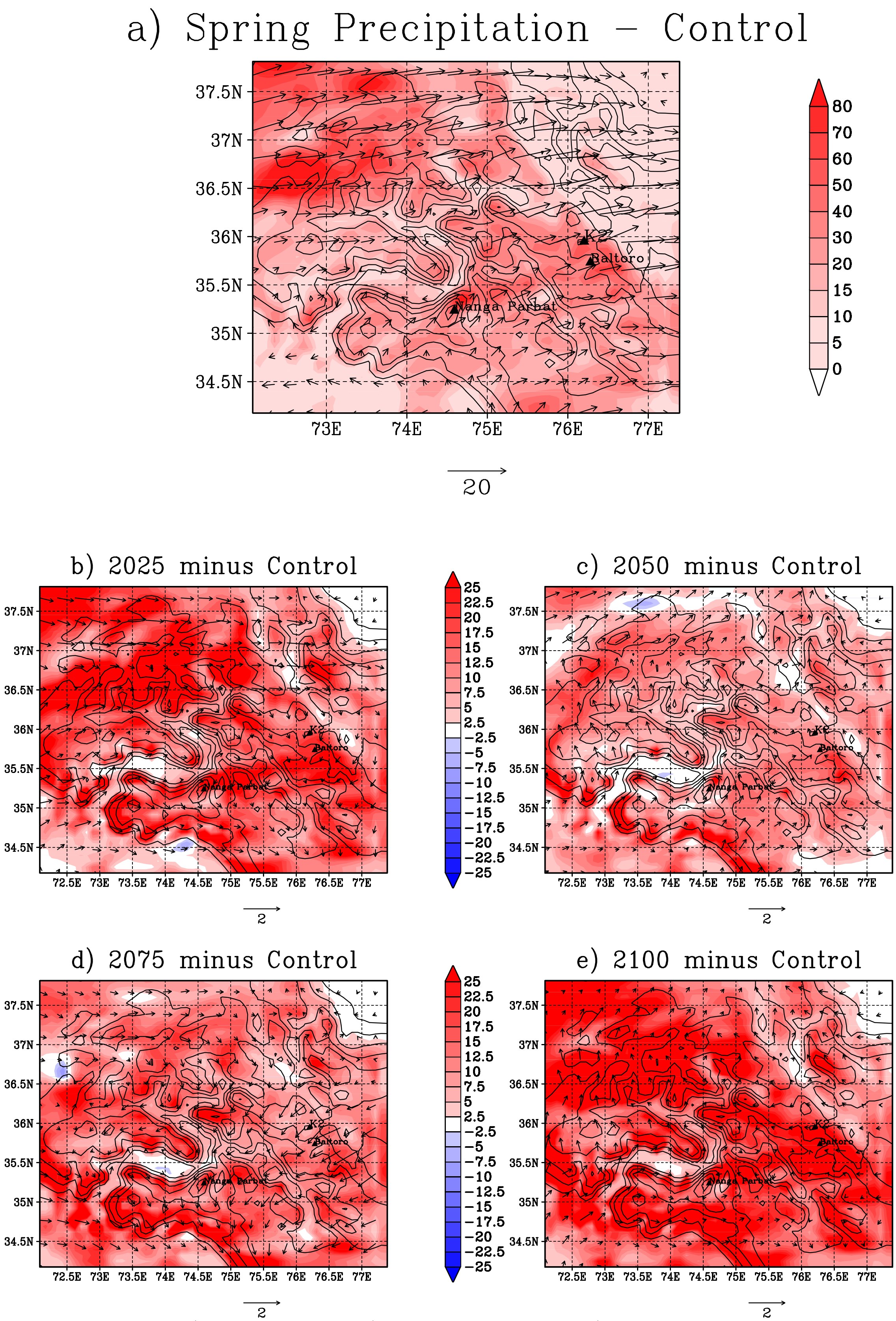

Figure 2.20: a) Precipitation (cm water equivalent) over the MAM period, plotted with lower level winds (m/s) averaged over the lowest 8 σ levels, for the Control simulation. b) As in a) but for 2025 minus Control. c) As in a) but for 2050 minus Control. d) As in a) but for 2075 minus Control. e) As in a) but for 2100 minus Control.

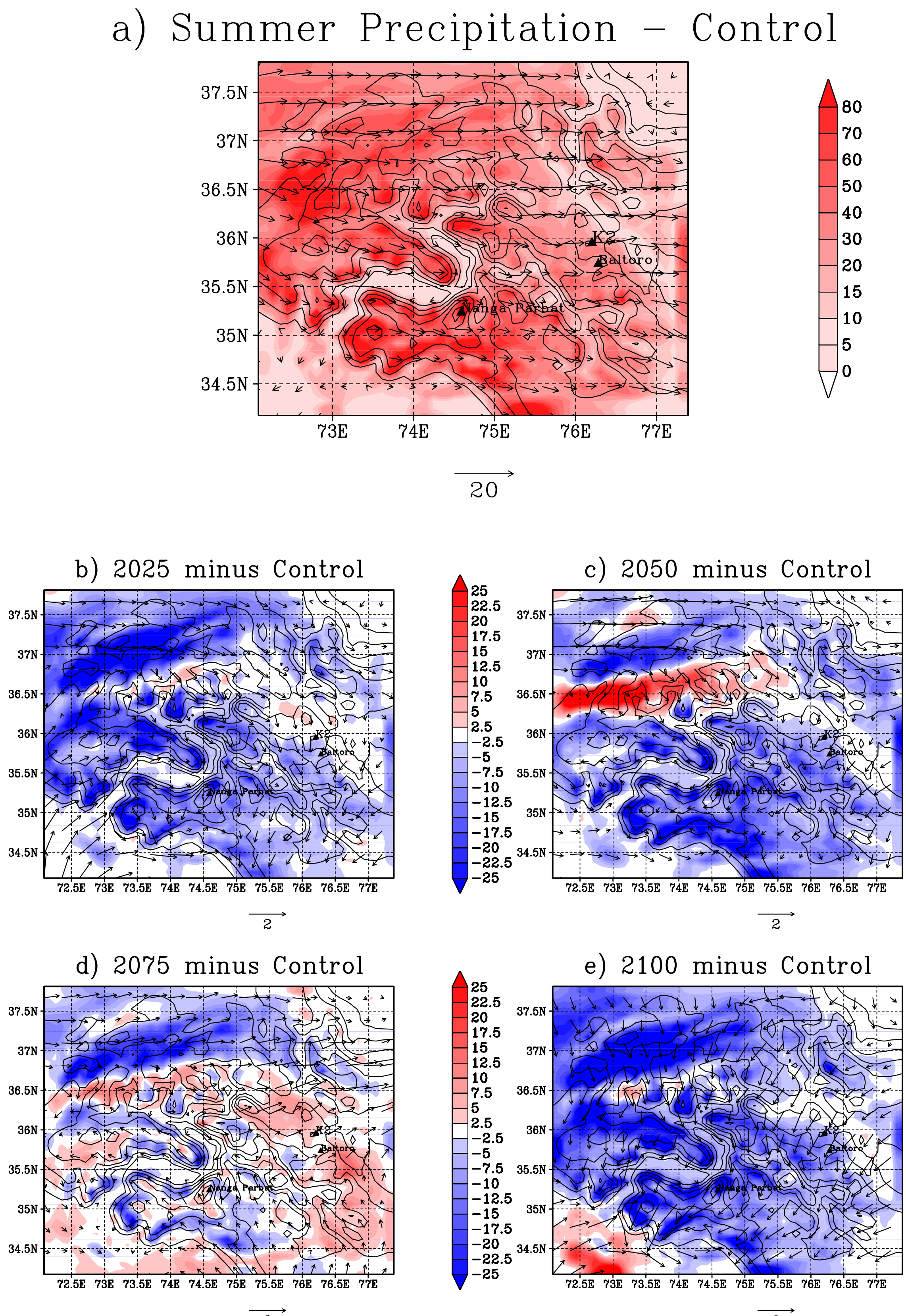

Figure 2.21: a) Precipitation (cm water equivalent) over the JJA period, plotted with lower level winds (m/s) averaged over the lowest 8 σ levels, for the Control simulation. b) As in a) but for 2025 minus Control. c) As in a) but for 2050 minus Control. d) As in a) but for 2075 minus Control. e) As in a) but for 2100 minus Control.

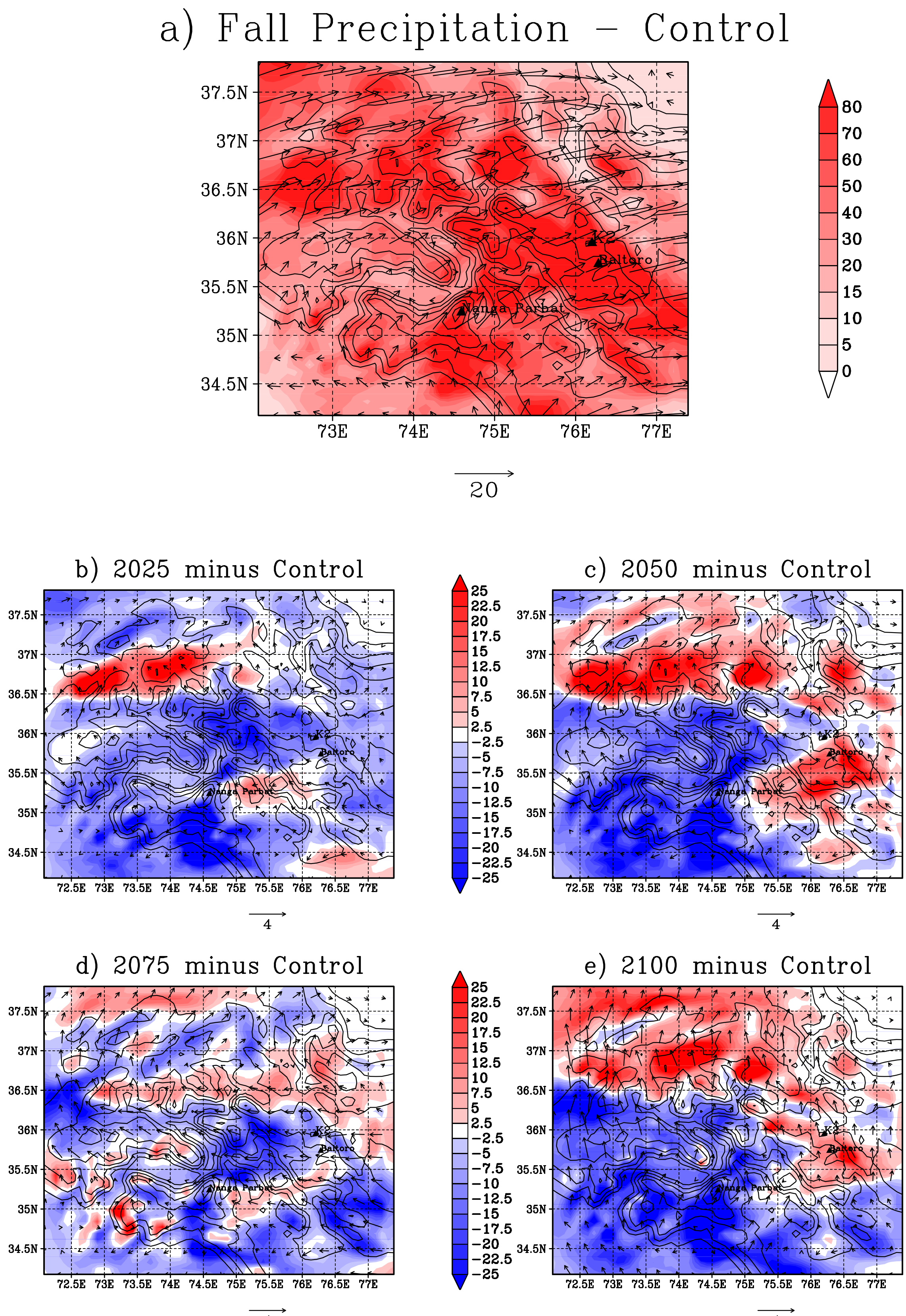

Figure 2.22: a) Precipitation (cm water equivalent) over the SON period, plotted with lower level winds (m/s) averaged over the lowest 8 σ levels, for the Control simulation. b) As in a) but for 2025 minus Control. c) As in a) but for 2050 minus Control. d) As in a) but for 2075 minus Control. e) As in a) but for 2100 minus Control.

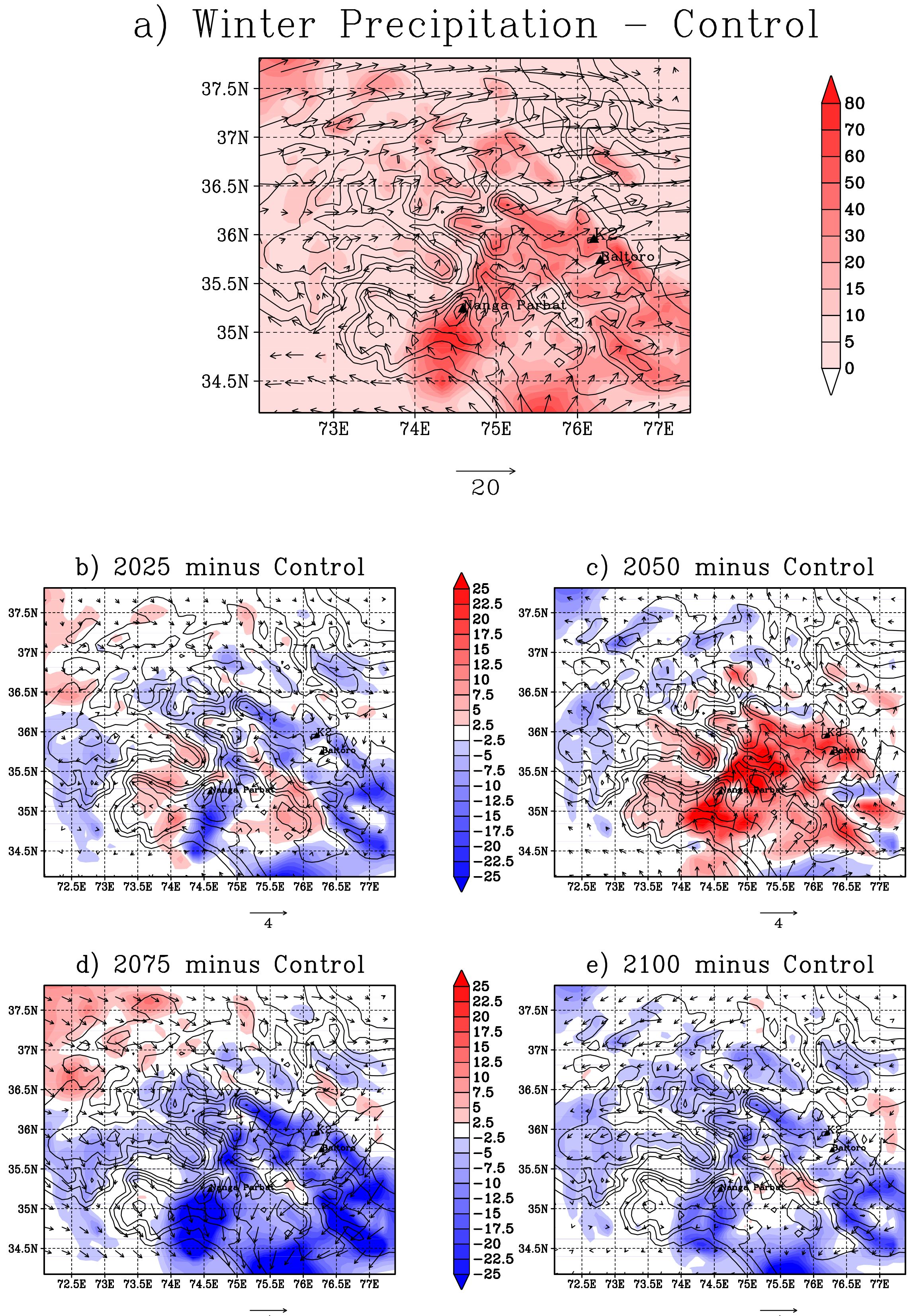

Figure 2.23: a) Precipitation (cm water equivalent) over the DJF period, plotted with lower level winds (m/s) averaged over the lowest 8 σ levels, for the Control simulation. b) As in a) but for 2025 minus Control. c) As in a) but for 2050 minus Control. d) As in a) but for 2075 minus Control. e) As in a) but for 2100 minus Control.

cance of anthropogenic warming on the region. Seasonal precipitation for the third model domain, along with lower level winds and three points of interest (the peaks of K2 and Nanga Parbat, along with the Baltoro Glacier) are shown in Figures 2.20 - 2.23. Interestingly, the largest precipitation increases are found in the spring months of March, April and May (Fig. 2.20), which is the time of most drastic simulated warming in the region (c.f. Fig. 2.14). As can be seen in Figure 2.14, areas of largest temperature increases over the Himalayan region are not large enough to increase regional temperatures above the freezing point, allowing for increases in precipitation to predominantly fall as snow. Circulation patterns portrayed in the spring months, indicated by wind vector anomalies in Figure 2.20, are highly variable and show no distinct pattern of evolution through the 21st century, although it is apparent that the spring months are predominantly influenced by westerly circulation patterns. Summer precipitation is shown to be mostly decreasing throughout the domain during the 21st century, with a few exceptions (Fig. 2.21). In particular, the 2075 simulation experiences a large increase in summer precipitation along 36.5°N and southward into the region of K2, arising from dominant westerly flow during this time period as described in Fig. 2.19d. Localized increases in precipitation are also apparent along 36.5°N in the 2025 simulation, and more so in the 2050 simulation, which also seem to be arising from a strengthening of westerly circulation in those regions (c.f. Figs. 2.21b and 2.21c). Summer precipitation is greatly reduced by the 2100 simulation, with circulation patterns indicating a more north-northeasterly direction, which is expected with a weakening of the summer monsoon system (c.f Figs. 2.13 and 2.19e). Low-elevated regions in the summer months show a clear indication of an increasing trend in precipitation under a warming climate. During the fall months of September, October and November, there is a distinct region in which large decreases in precipitation swiftly change to vast increases in precipitation (Fig. 2.22). Again, circulation patterns in these months are highly variable, with a more southerly component to wind directions by the end of the 21st century. Precipitation in the winter months does not seem to follow a distinct pattern, but rather relies more on the direction and origin of winds in the region (Fig. 2.23). During times of increased moist, southerly winds (c.f Fig. 2.23c), the Karakoram region receives an abundance of precipitation, whereas during times of increased dry, north-northeasterly winds (c.f Figs. 2.23d and 2.23e), a vast decrease in precipitation is simulated. It is interesting to note that during the 2050 simulation (a period of increased summer monsoon flow), there is decreased winter monsoon flow out of the Karakoram region, and vice versa during the 2075 simulation. The combined effect of these seasonal variations in precipitation on glacial evolution in the Karakoram region need to be considered when performing glacial mass balance calculations.

2.3.2 Snow Mass Balance Results

Annual snowfall accumulation results for the Karakoram region (herein consistent with the third model domain) are shown in Figure 2.24. As can be seen through the seasonal response to changes in precipitation (c.f. Figs. 2.20 - 2.23), the area of most pronounced precipitation increase lies along the line of 36.5°N, as well as areas of extremely high elevations surrounding the peak of K2. During the Control simulation (c.f. Fig. 2.24a), it is apparent that over an annual timescale, the mid-latitude westerlies provide the dominant climatic influence into the region. In the 2025 simulation, increases in snowfall along the line of 36.5°N are simulated, arising from an overall strengthening of the

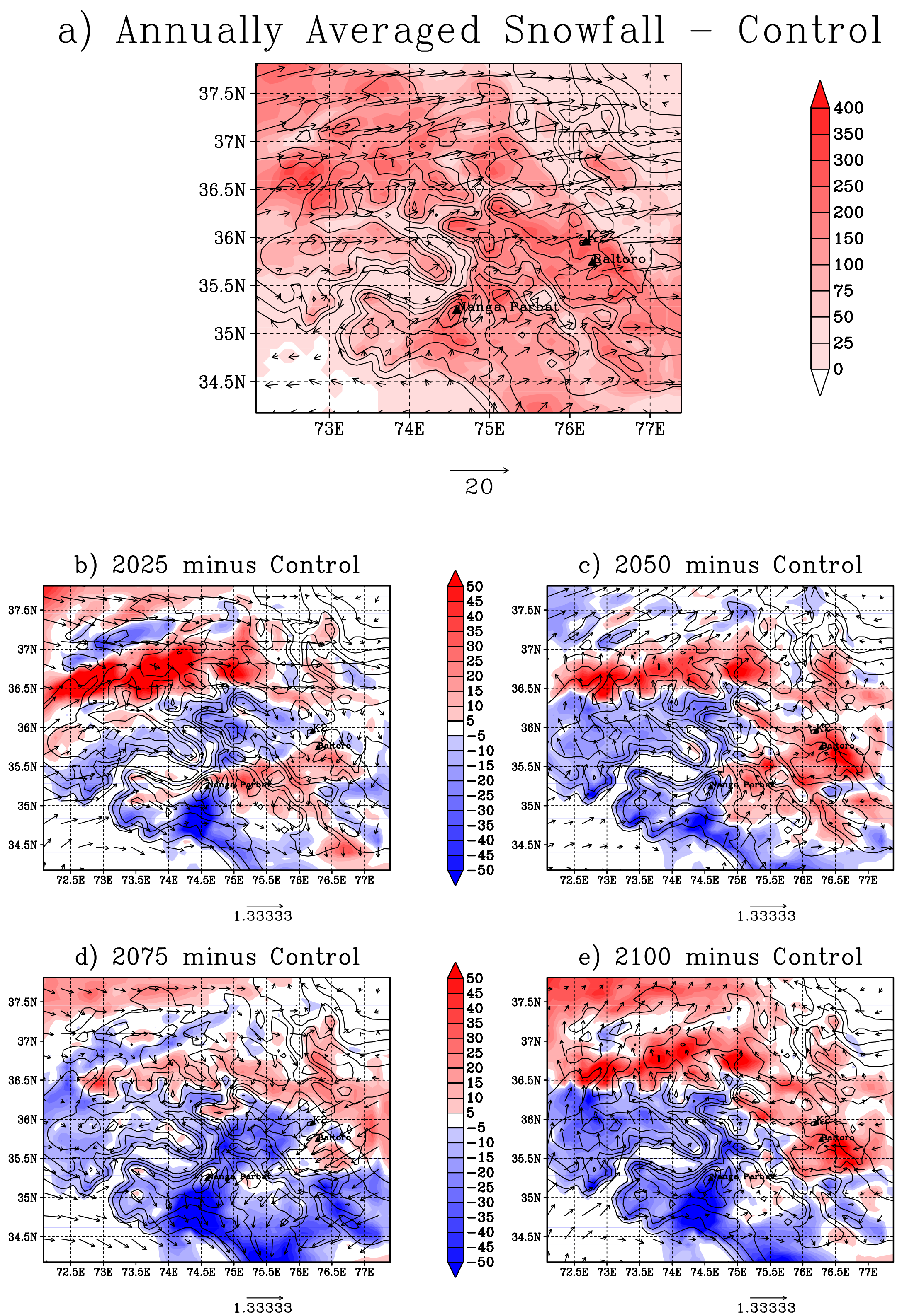

Figure 2.24: a) Annually averaged snowfall accumulation (cm water equivalent), superimposed with lower level winds averaged over the lowest 8 σ levels (m/s) for the Control simulation. b) As in a), but for 2025 minus Control. c) As in a), but for 2050 minus Control. d) As in a), but for 2075 minus Control. e) As in a), but for 2100 minus Control.

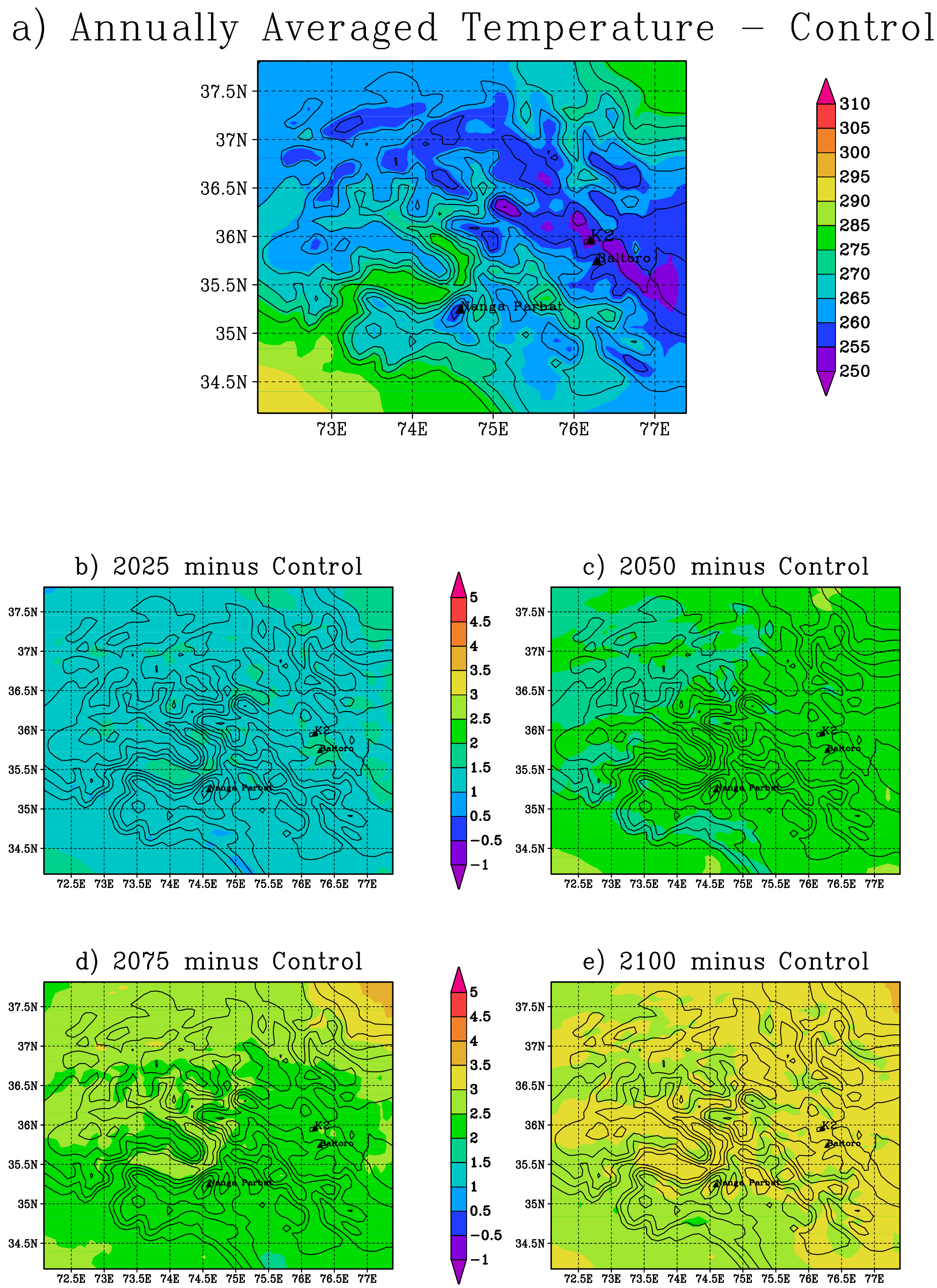

Figure 2.25: a) Annually averaged temperature (K) for the Control simulation. b) As in a), but for 2025 minus Control. c) As in a), but for 2050 minus Control. d) As in a), but for 2075 minus Control. e) As in a), but for 2100 minus Control.

westerlies during this time, with little influence of the Asian summer monsoon on an annual timescale. On the other hand, during the 2050 simulation, we do see an intrusion of the summer monsoon winds, which agrees with the suggestion of a stronger monsoonal system during this time period (c.f. Fig. 2.19c). This allows for increased snowfall accumulation at the lower latitudes surrounding the peaks of Nanga Parbat and K2. During the 2075 simulation, there is a drastic decrease in southerly wind strength over an annual timescale, which again agrees with the suggestion of a much weaker monsoonal system during this time period (c.f. Fig. 2.19d). Hence, decreases in snowfall accumulation at lower latitudes are simulated, with only slight increases at higher latitudes within the domain. By the end of the 21st century, the area of increased snowfall accumulation along 36.5°N is still very prominent, with lower level winds signifying a slight decrease in strength in both the westerlies and Asian summer monsoon. Despite increasing temperatures (and elevation dependency on this increase), which can be seen in Figure 2.25, areas of high elevations such as the peak of K2 are still experiencing increases in annual snowfall accumulation by the end of the 21st century, suggesting conditions for positive glacial mass balance in the future.

However, not all accumulated snowfall is able to persist through an annual cycle, as the effects of solar radiation, changes in precipitation, and other heat fluxes will reduce the accumulated amount of snowfall, and will therefore be the determining factors when performing mass balance estimations. Despite the albedo of snow being between 60 and 90% (Warren, 1982), incident short wave radiation is a large energy source for snow and ice melt on alpine glaciers. Results for the evolution of short wave radiation through the 21st century are shown in Figure 2.26. As can be seen in the Control simulation,

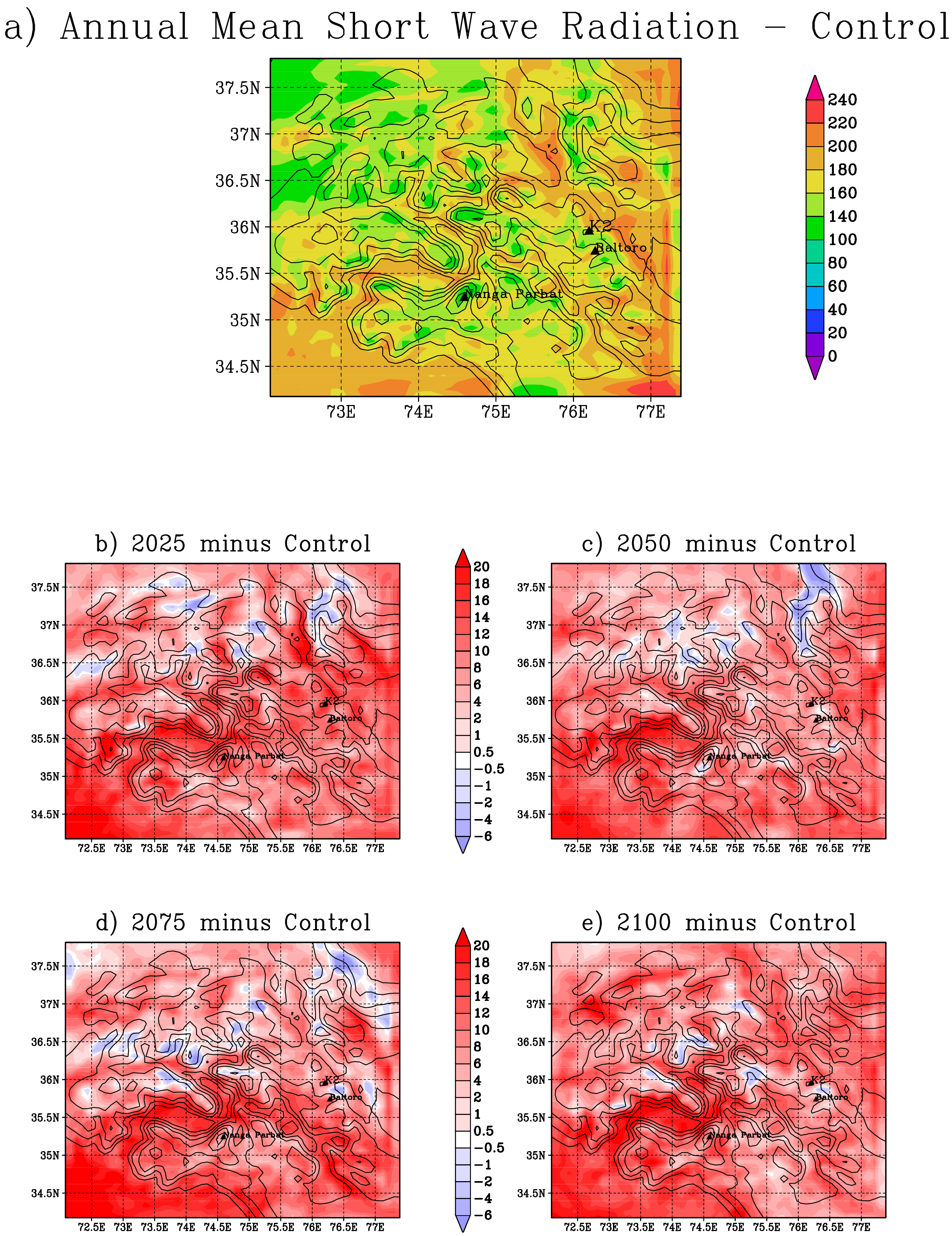

Figure 2.26: a) Annually averaged short wave radiation (W m^{-2}) for the Control simulation. b) As in a), but for 2025 minus Control. c) As in a), but for 2050 minus Control. d) As in a), but for 2075 minus Control. e) As in a), but for 2100 minus Control.

incident short wave radiation decreases with latitude, which is an expected characteristic of incoming solar radiation. While incident short wave radiation increases through the 21st century over most of the domain, which is correlated with increasing temperatures, there are a few scattered areas of unchanging or decreasing short wave radiation, particularly surrounding the line of 36.5°N as well as areas of extremely high elevation, such as the peak of K2 and the Baltoro glacier. These slight decreases are most substantial during the 2075 simulation, and least substantial during the 2100 simulation. The reduction in incoming solar radiation at higher altitudes, possibly arising from increased reflection due to the high albedo of snow or increased orographic cloud formation, will allow for decreased melting of snowfall accumulation of high elevation glaciers, and thus have a positive effect on the region's glacial mass balance.

Under a warming climate with increasing atmospheric CO_2 concentrations, long wave radiation emitted from the Earth's surface, which is then absorbed and re-remitted by lower level clouds, becomes an increasingly more important factor in global energy balance. As can be see in Figure 2.27, incident long wave radiation over the Karakoram region is steadily increasing through the 21st century, which is expected under an increasing CO_2 regime, and negatively affects snow and ice mass balance on a global scale.

Since changes in incoming and outgoing radiation are directly related to the type and frequency of cloud cover, it is necessary to investigate the evolution of cloud cover in a warming climate. Results for low and mid level cloud cover evolution suggest an overall decrease by the end of the 21st century, with a few exceptions of increases (particularly in the 2050 and 2075 simulation).

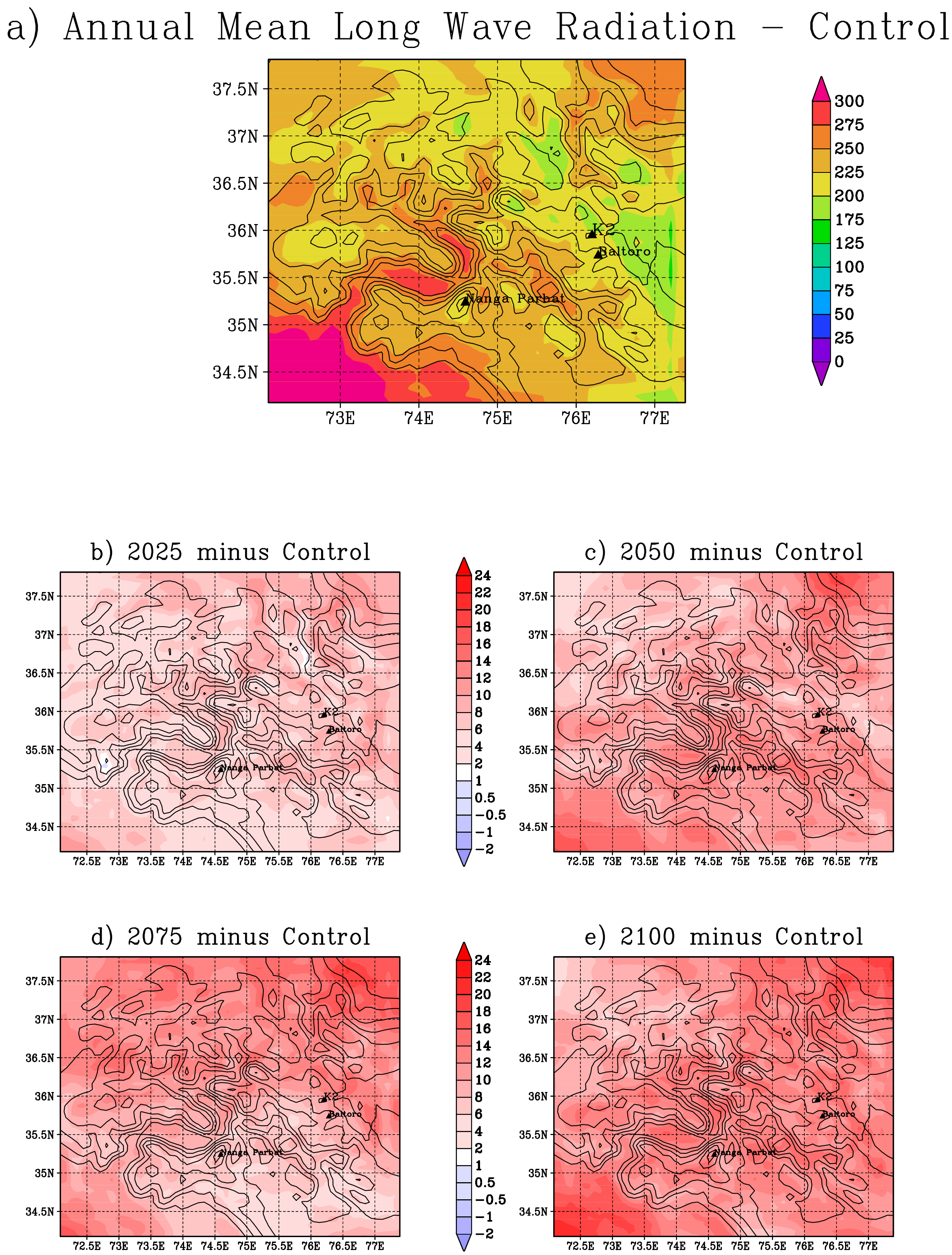

Figure 2.27: a) Annually averaged long wave radiation (W m^{-2}) for the Control simulation. b) As in a), but for 2025 minus Control. c) As in a), but for 2050 minus Control. d) As in a), but for 2075 minus Control. e) As in a), but for 2100 minus Control.

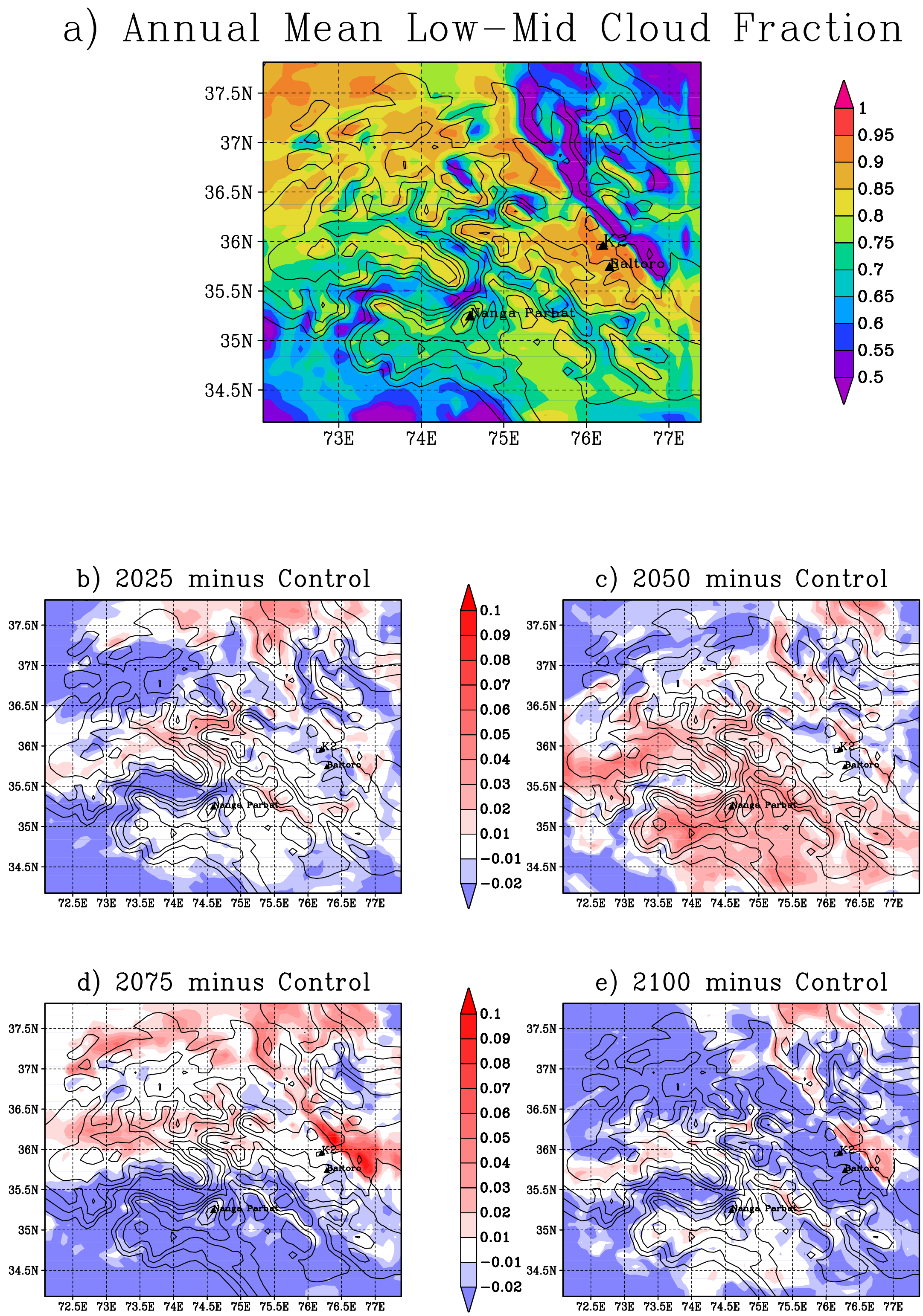

Figure 2.28: a) Annually averaged low and mid level cloud fraction for the Control simulation. b) As in a), but for 2025 minus Control. c) As in a), but for 2050 minus Control. d) As in a), but for 2075 minus Control. e) As in a), but for 2100 minus Control.

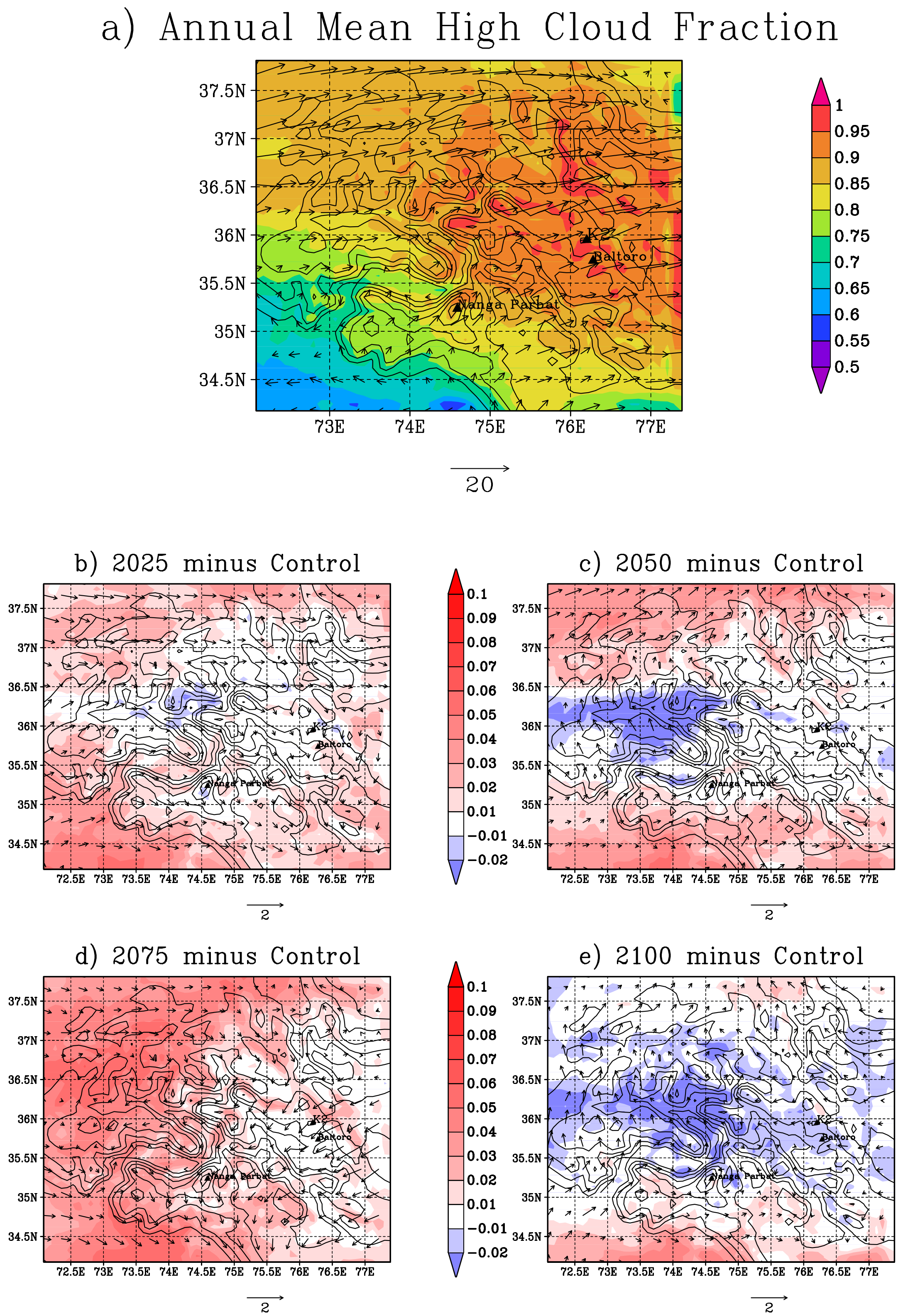

Figure 2.29: a) Annually averaged high level cloud fraction for the Control simulation. b) As in a), but for 2025 minus Control. c) As in a), but for 2050 minus Control. d) As in a), but for 2075 minus Control. e) As in a), but for 2100 minus Control.

While the causes and determining factors of cloud cover variability are not well known, Hansen *et al.* (1981) state that while high level clouds are a more efficient absorber of long wave radiation, therefore promoting the "greenhouse effect" on surface temperatures, low and mid level clouds are more efficient reflectors of incoming solar radiation, which results in a cooling effect of the Earth's surface. Therefore, there is a clear negative correlation between low and mid level cloud cover (c.f. Fig. 2.28) and incident short wave radiation (c.f. Fig. 2.26), with these correlations being least substantial during the 2100 simulation. Results for high level cloud cover evolution also suggest an overall decrease by the end of the 21st century, however results show times of prominent increase in high level cloud cover, such as the 2025 and 2075 simulations (c.f. Fig. 2.29). There is a clear positive correlation between high level cloud cover and incident long wave radiation up until the 2100 simulation (c.f. Fig. 2.27), at which point this correlation seems to dissolve. It is possible that due to the extreme elevations in the Karakoram region, the level at which high level cloud appears is beyond that defined by the high cloud variable set by the model.

While increases in accumulated snowfall suggest conditions of positive glacial mass balance (c.f. Fig. 2.24), it is necessary to investigate changes in rainfall accumulation, as any increases in rainfall will have a negative effect on the region's glaciers. As can be seen in the 2075 and 2100 simulations (Fig. 2.30d and 2.30e), areas of increased rainfall correspond to areas of decreased snowfall (c.f. Fig. 2.24), which is expected with increasing temperatures throughout the region (c.f. Fig. 2.25), as this allows for a transition of precipitation type from snow to rain as temperatures are raised above the freezing point of water. Also corresponding to increasing temperatures, increases in

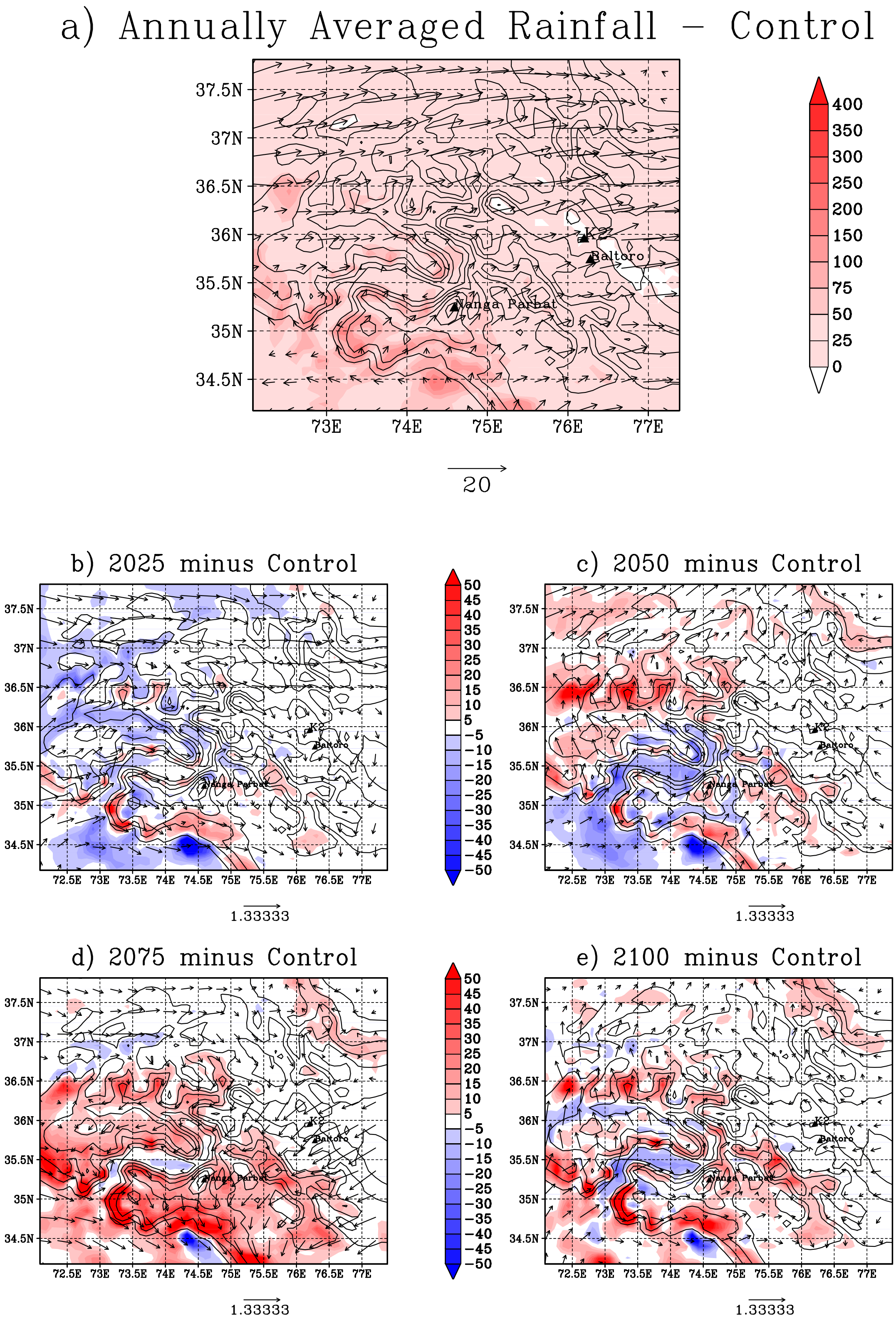

Figure 2.30: a) Annually averaged rainfall accumulation (cm), superimposed with lower level winds averaged over the lowest 8 σ levels (m/s) for the Control simulation. b) As in a), but for 2025 minus Control. c) As in a), but for 2050 minus Control. d) As in a), but for 2075 minus Control. e) As in a), but for 2100 minus Control.

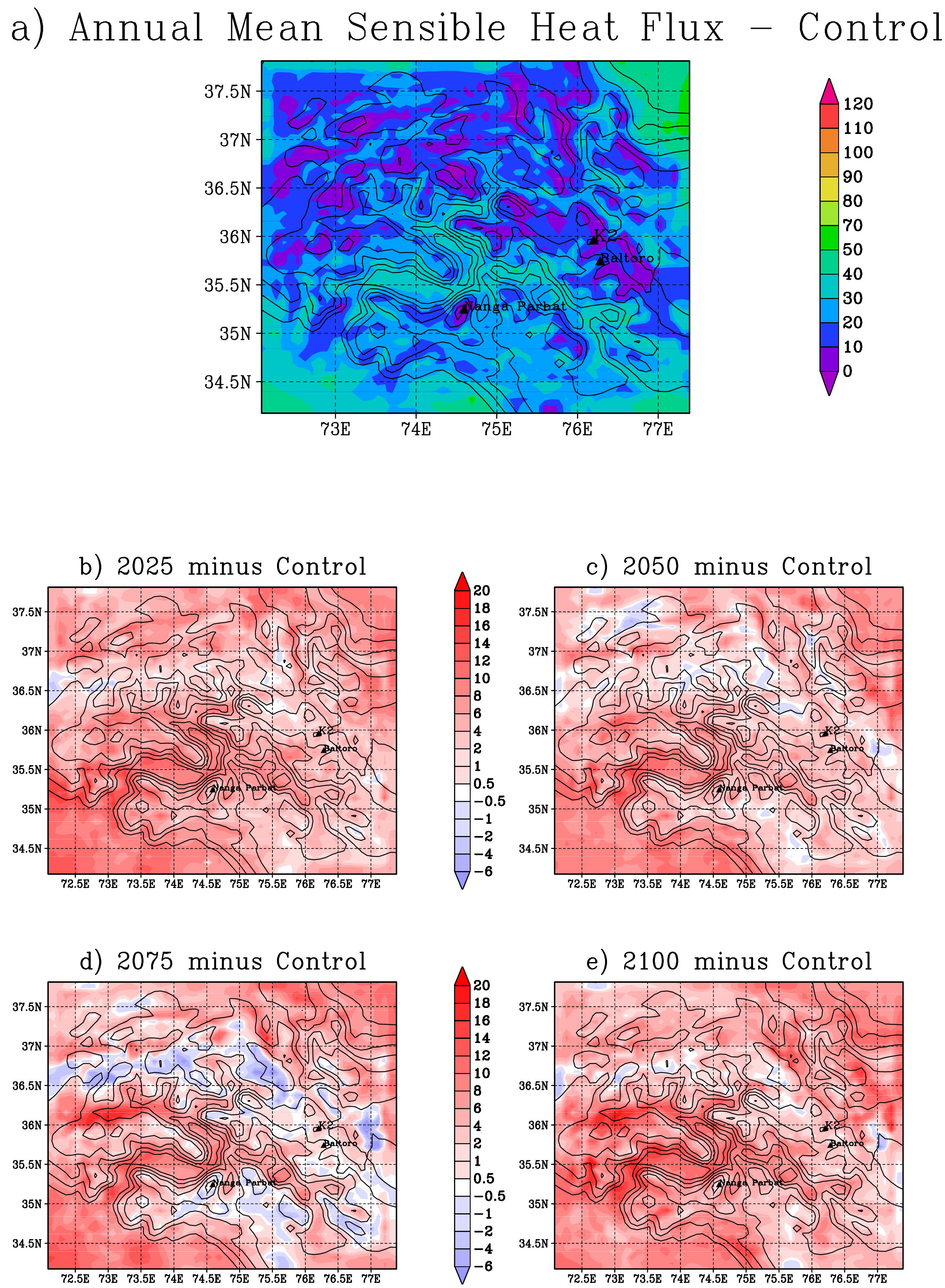

Figure 2.31: a) Annually averaged sensible heat flux (W $^{-2}$) for the Control simulation. b) As in a), but for 2025 minus Control. c) As in a), but for 2050 minus Control. d) As in a), but for 2075 minus Control. e) As in a), but for 2100 minus Control.

sensible heat flux can be seen through the Karakoram region, with areas of decreased sensible heat flux along 36.5°N in the 2075 simulation (Fig. 2.31). It is interesting to note that areas of decreasing or relatively unchanging sensible heat flux correspond to the areas of least temperature increase in the region (c.f. Fig. 2.25d), which is expected. Any areas of decreasing sensible heat flux will have a positive effect on glacial mass balance.

By combining the radiative melting effects of the above mentioned variables, and subtracting this combined effect from annually accumulated snowfall, a simple calculation is performed to yield an estimation of annual snow mass balance evolution in the Karakoram region under a warming climate. Annual snow mass balance (cm yr^{-1}) is formulated as a function of accumulated snowfall (cm yr^{-1}), incoming short and long wave radiation (W m^{-2}), sensible heat flux (W m^{-2}), and rainfall rate (r). The combination of accumulation and ablation is described in the following formula for snow mass balance (SMB) integrated over a 6-hour time span:

$$SMB = S - \frac{1}{L_f} \int H(T(t) - T_f)\gamma(t)dt \tag{2.2}$$

where S is the annual snowfall accumulation as described above, L_f is the latent heat of fusion for water (3.34 X 10^5 J kg^{-1}), T_f is the freezing temperature of water (273.15 K) and $H(x)$ is the step function, given as:

$$H(x) = \begin{cases} 1 & \text{if } x \geq 0 \\ 0 & \text{if } x < 0 \end{cases} \tag{2.3}$$

where x represents the variable to which we are applying the step function. The use of this step function in our mass balance calculation monitors that for temperatures below the freezing point of water, no ice or snow melt can occur. The function $\gamma(t)$ in equation 2.2 represents the combined melting factors of long and short wave radiation, sensible heat flux and rainfall rate, and is described by the following equation:

$$\gamma(t) = R_s(t)\alpha_s + Q_{shf} + H(R_l(t) - R_o)(R_l(t) - R_o) + c_{pw}r(t)(T(t) - T_f) \quad (2.4)$$

where R_s is the incident short wave radiation, R_l is the incident long wave radiation, α_s is the fraction of incident short wave radiation that is absorbed (taken as 0.3), R_o is the outgoing long wave radiation from an ice surface at 0°C (315 W m^{-2}) and c_{pw} is the specific heat capacity at constant pressure for water (4186 J kg^{-1} K^{-1}). In this case, the step function is used to regulate that no snow or ice melt occur when outgoing long wave radiation is greater than incoming long wave radiation, which implies cooling conditions. It is assumed that reflectivity of downward long wave radiation by the Earth's surface is negligible, hence there is no absorption factor for this term in equation 3.4. The sensible heat flux Q_{shf} is prescribed as seen in Munro (1991):

$$Q_{shf} = \rho_a(t)c_{pa}k_v^2 \frac{u(T(t) - T_f)}{[ln(z/z_o)]^2} \quad (2.5)$$

where ρ_a is air density (kg m^{-3}), c_{pa} is the specific heat capacity for air at constant pressure (1004 J kg^{-1} K^{-1}), k_v is the von Karman constant (taken as 0.41), u is the wind speed (m s^{-1}), z is height above ground (taken as 2 m), and z_o is the roughness length of a relatively smooth, wet snow covered surface (taken as 0.1 mm based on results by Calanca (2001)).

In this simple estimation for snow mass balance, liquid water produced by the melting of snow is assumed to immediately become involved in glacial runoff processes, and is therefore not available for refreezing. Without a more complex snow and ice model that is able to capture internal glacier dynamics, it is difficult to include the effects of refreezing on snow mass balance. Also for simplicity, the effects of latent heat fluxes arising from evaporation and sublimation, as well as ground heat storage, are ignored. Hence, the estimation for snow mass balance presented in this study is solely dependent on melt arising from changes in temperature, precipitation type, and downward radiation.

Each melting term described in equation 2.5 is investigated independently in Figures 2.32 - 2.35. Melt due to changes in short wave radiation and sensible heat fluxes are shown to be the dominant melting terms in equation 2.5 (c.f. Figs. 2.32 & 2.33), with melt due to long wave radiation and heat contained in rainfall being more substantial at lower elevations (c.f. Figs. 2.34 & 2.35). Consistent with the results for changes in incident short wave radiation (c.f. Fig. 2.26), Figure 2.32 shows areas of unchanging and even decreasing melt due to incident short wave radiation at the highest elevations in the Karakoram region, most prominently in the 2075 simulation. As mentioned previously, this arises from increases in low and mid level cloud cover seen over the Karakoram region (c.f. Fig. 2.28), as well as the glacier-nourishing effects of the snow-albedo feedback mechanism in the presence of increased snowfall. Melt due to sensible heat fluxes shows an elevation dependency throughout the 21st century, but experiences a substantial increase under a warming climate due to the direct relationship to increases in surface temperatures. However,

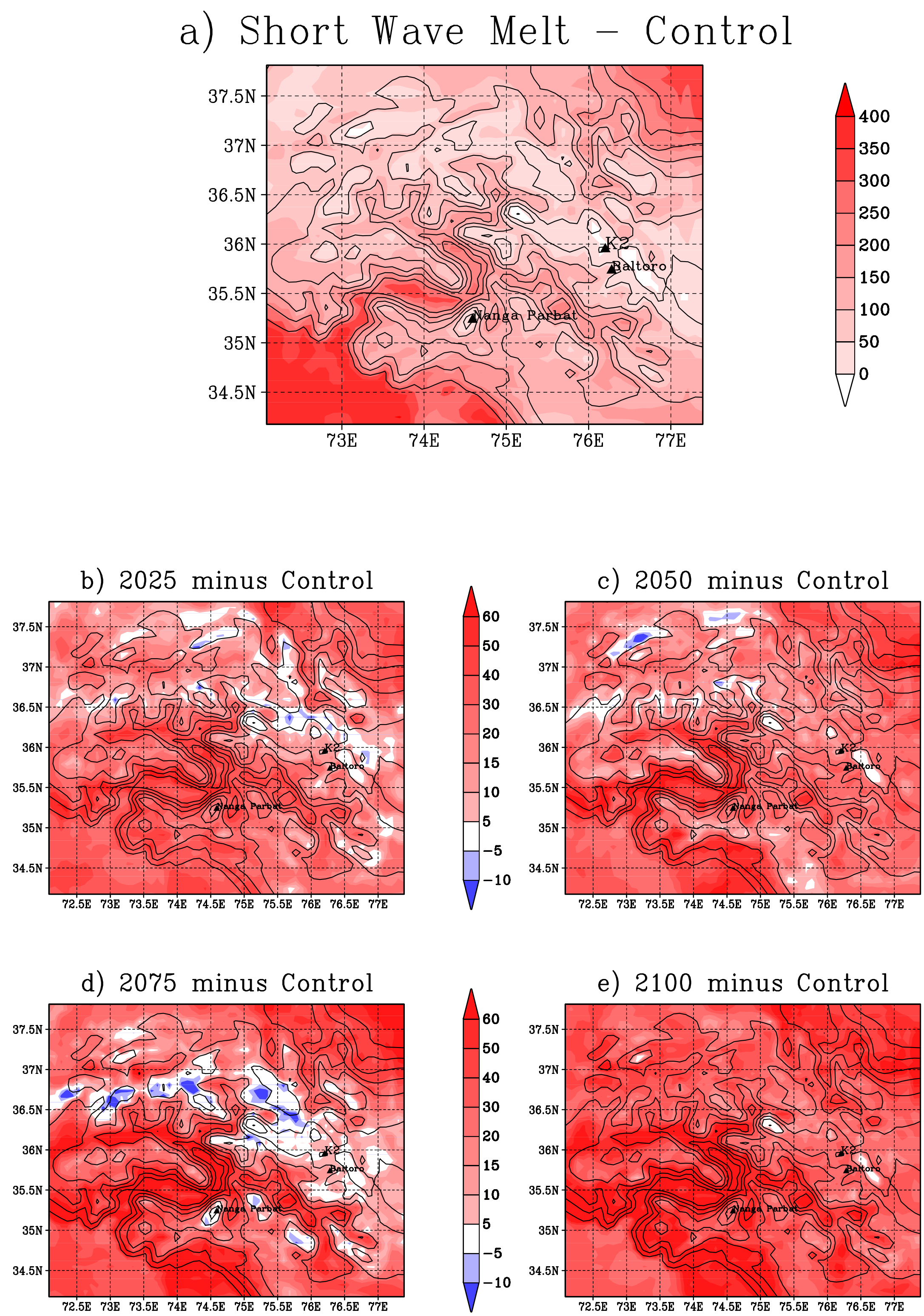

Figure 2.32: a) Annual snow melt due to incident short wave radiation (cm water equivalent) for the Control simulation. b) As in a), but for 2025 minus Control. c) As in a), but for 2050 minus Control. d) As in a), but for 2075 minus Control. e) As in a), but for 2100 minus Control.

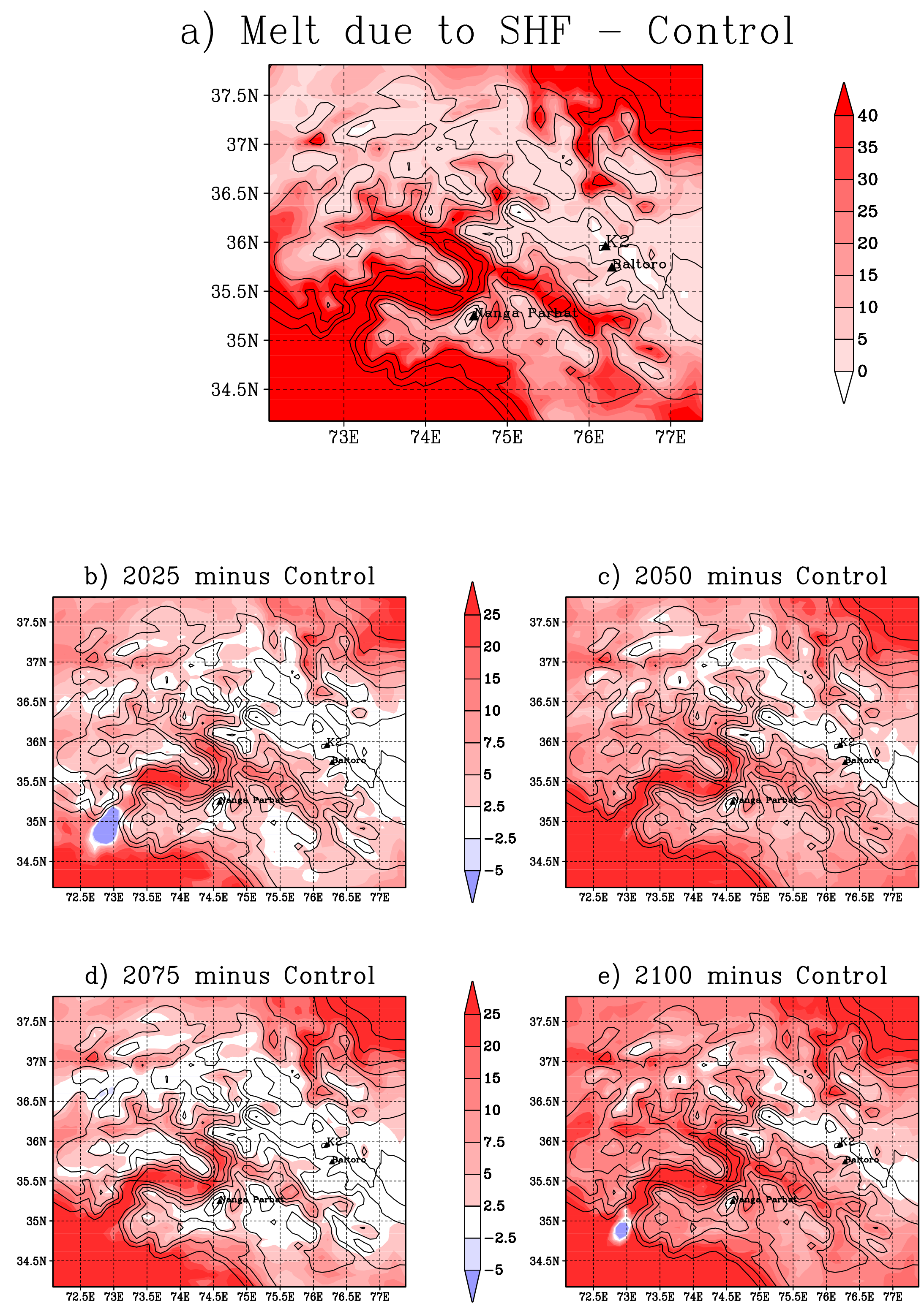

Figure 2.33: a) Annual snow melt due to sensible heat fluxes (cm water equivalent) for the Control simulation. b) As in a), but for 2025 minus Control. c) As in a), but for 2050 minus Control. d) As in a), but for 2075 minus Control. e) As in a), but for 2100 minus Control.

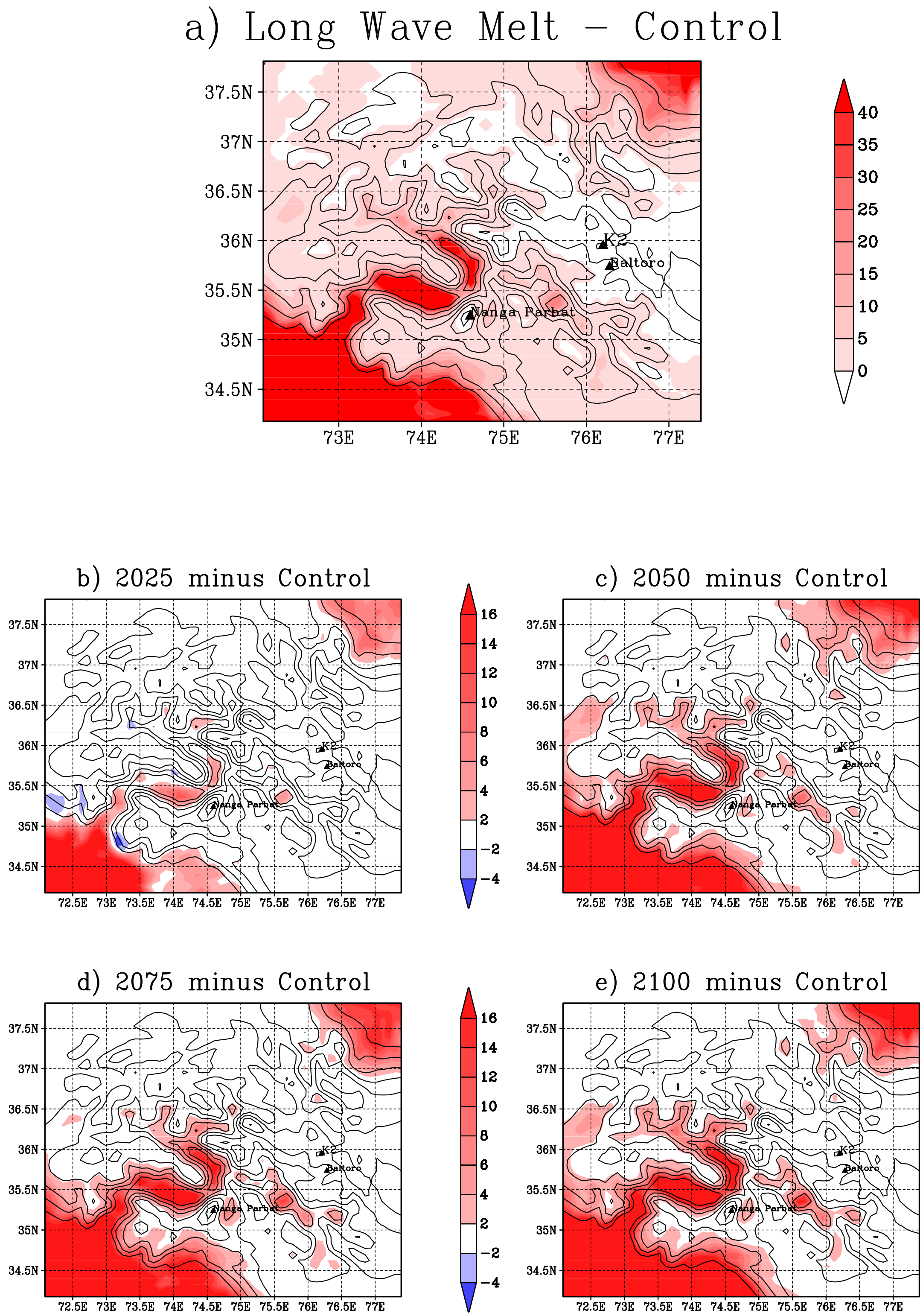

Figure 2.34: a) Annual snow melt due to incident long wave radiation (cm water equivalent) for the Control simulation. b) As in a), but for 2025 minus Control. c) As in a), but for 2050 minus Control. d) As in a), but for 2075 minus Control. e) As in a), but for 2100 minus Control.

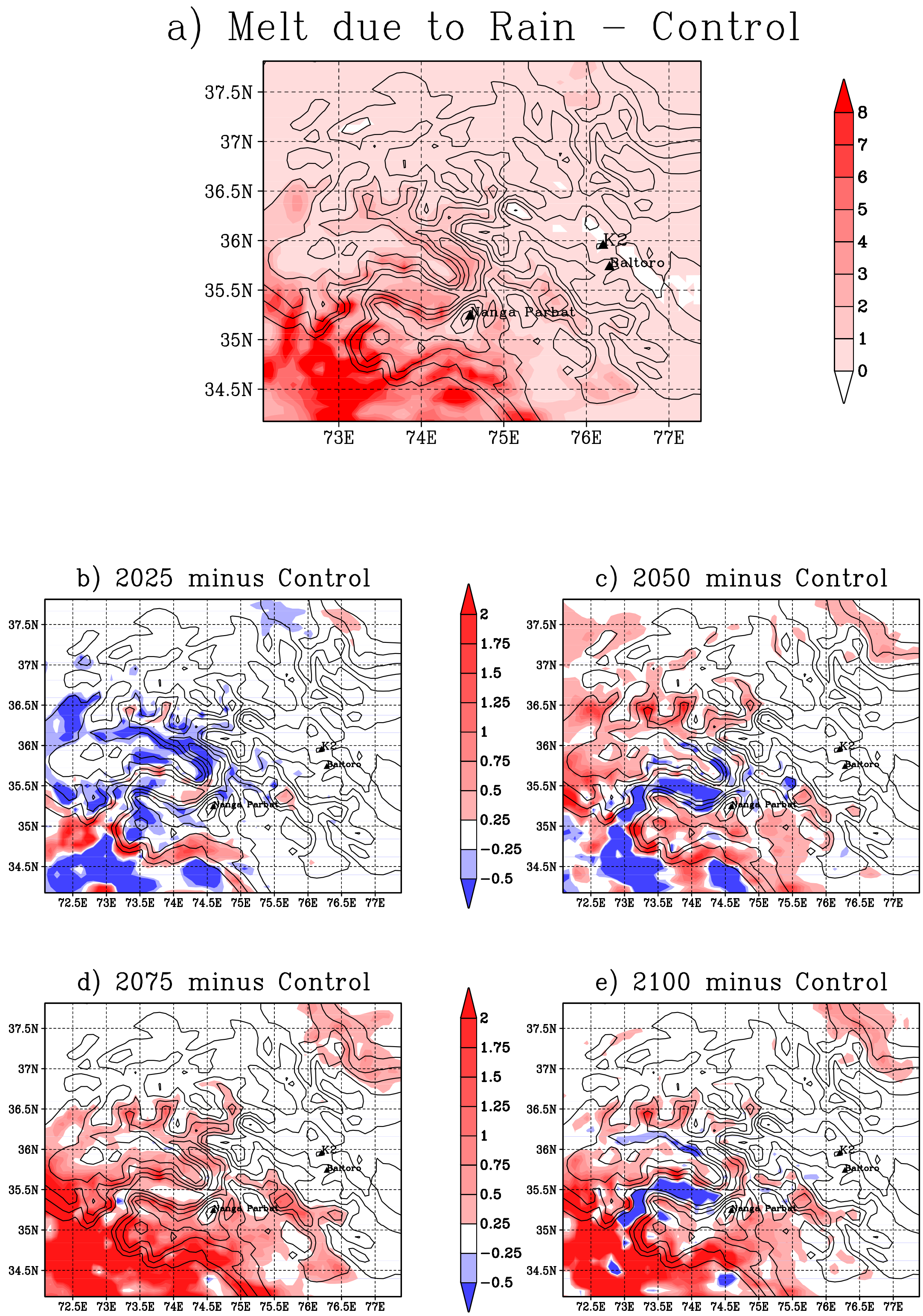

Figure 2.35: a) Annual snow melt due to heat contained in rain (cm water equivalent) for the Control simulation. b) As in a), but for 2025 minus Control. c) As in a), but for 2050 minus Control. d) As in a), but for 2075 minus Control. e) As in a), but for 2100 minus Control.

due to the high elevation of the Karakoram region, increases in sensible heat flux do not compare in magnitude to increases in incident short wave radiation throughout the region, implying that changes in short wave radiation are the dominant melting factor when performing mass balance calculations. Increases in melt due to incident long wave radiation, as well as the migration of these increases into higher altitudes during the 21st century (c.f. Fig. 2.34), are consistent with the evolutionary results of long wave radiation (c.f. Fig. 2.27), but do not seem to have an impact on the highest of elevations within the Karakoram region. While melt due to the heat contained in rainfall is highly variable (c.f. Fig. 2.35), the results are consistent with changes in accumulated rainfall under a warming climate (c.f. Fig. 2.30). However, the magnitude of melt due to rainfall throughout the Karakoram region is relatively small compared to the magnitudes of the other melting terms in equation 2.5.

By combining the melting effects of the terms described above, results for annual snow mass balance, described by equation 2.2, are calculated and portrayed in Figure 2.36. Throughout the 21st century, higher net snow accumulation tends to occur in areas that experience an increase in snowfall, which occurs most prominently along the line of 36.5°N (c.f. Figs. 2.24 & 2.36). Snow mass balance results show a clear dependency on elevation, with the most substantial increases in net snow accumulation at the highest elevations of the Karakoram region. Despite increases in surface temperatures (c.f. Fig. 2.25), snow mass balance shows an increasing trend at high elevations during the 2025 simulation, with simultaneous decreases in snow mass balance at lower elevations throughout the domain (c.f. Fig. 2.36b). Subsequent decreases in the surface area containing positive snow mass balance are seen until the end of the 21st century, at which time the least substantial increases

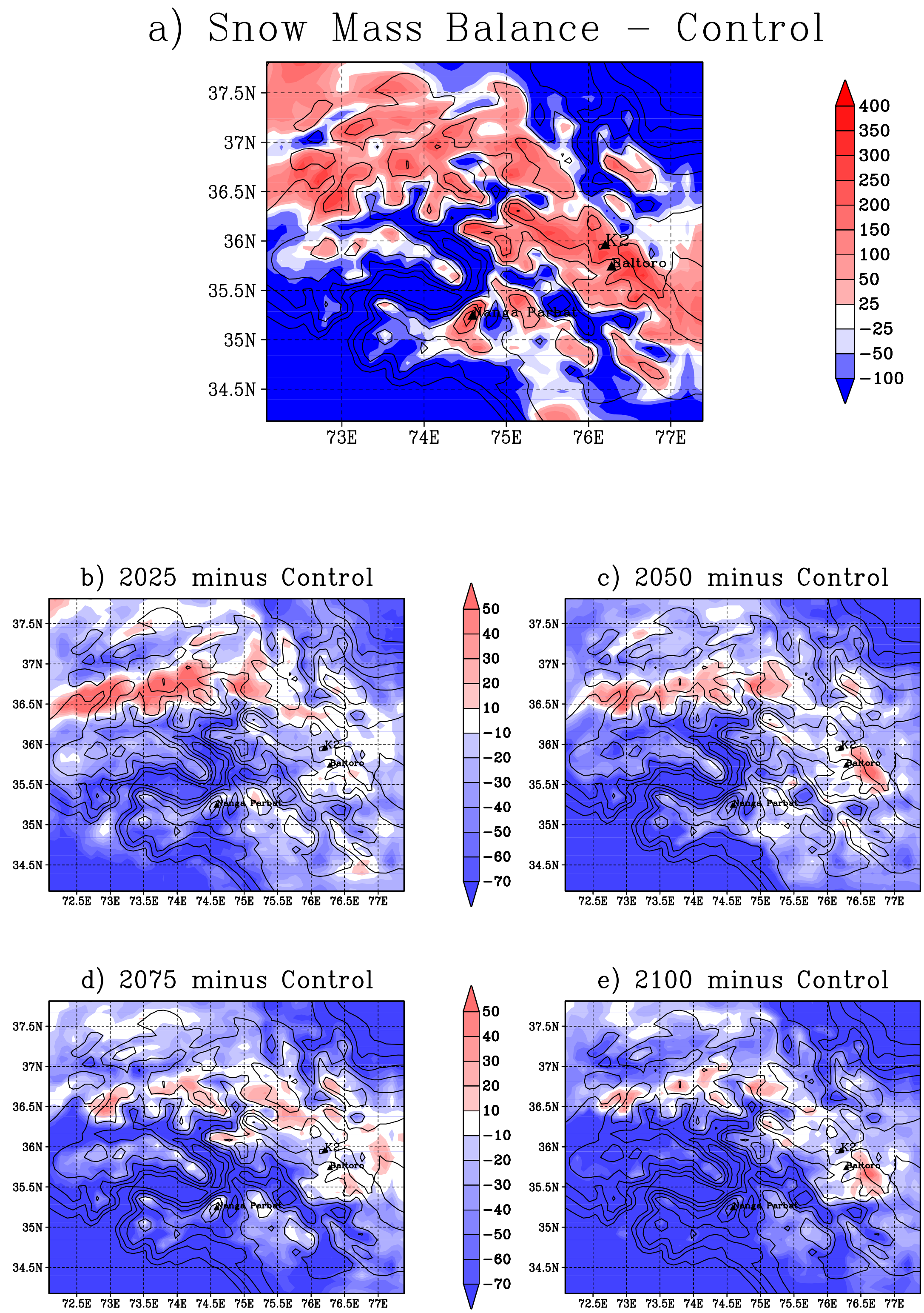

Figure 2.36: a) Annual snow mass balance (cm water equivalent) for the Control simulation. b) As in a), but for 2025 minus Control. c) As in a), but for 2050 minus Control. d) As in a), but for 2075 minus Control. e) As in a), but for 2100 minus Control.

in net snow accumulation is seen at the highest elevations, and the strongest decreases at the lowest elevations (c.f. Fig. 2.36e). It is clear that the slight decreases in simulated melt due to short wave radiation (c.f. Fig. 2.32), combined with relatively unchanging melt due to sensible heat flux surrounding the region of 36.5°N greatly overpower the influence of increasing surface temperatures on annual snow mass balance.

By separating the results for annual snow mass balance into seasonal components, it is apparent that the periods of most substantial increases in snow mass balance occur in the spring and fall months (c.f. Figs. 2.37 & 2.39), consistent with the time periods of most substantial precipitation increases (c.f Figs. 2.20 & 2.22). These increases in seasonal snow mass balance are located along 36.5°N as well as regions surrounding the peak of K2, which is consistent with the areas of positive annual net snow accumulation seen in Figure 2.36. However, the magnitude of snow melt that occurs during the summer months steadily increases through the 21st century (c.f. Fig. 2.38), corresponding to increases in surface temperatures at higher elevations (c.f. Fig. 2.15) and decreases in precipitation (c.f. Fig. 2.21), which has an increasingly negative effect on annual snow mass balance in the future.

Results for the equilibrium line altitude (ELA) evolution for the 21st century are shown in Figure 2.41, in which the shaded region represents the surface area encompassed by the equilibrium line. Here, the ELA is taken as the level of no net change in annual snow mass balance (c.f. Fig. 2.36) and hence, due to the smoothing of topography by MM5, the estimated position of the ELA will also be smoother than reality, encompassing a wider area. However, since glaciated and non-glaciated areas are generally separated by the level of no net

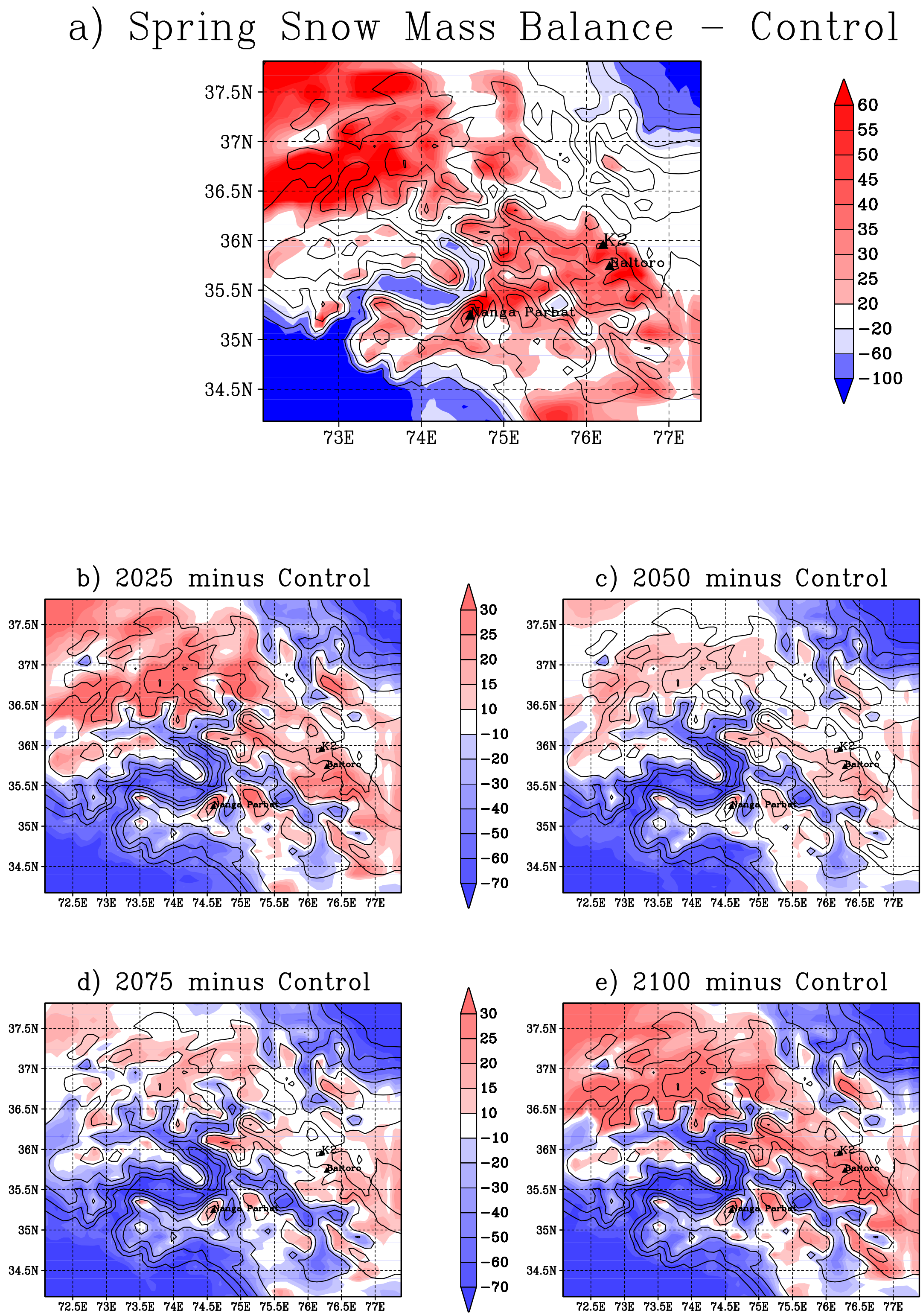

Figure 2.37: a) Snow mass balance during the months of March, April and May (cm water equivalent) for the Control simulation. b) As in a), but for 2025 minus Control. c) As in a), but for 2050 minus Control. d) As in a), but for 2075 minus Control. e) As in a), but for 2100 minus Control.

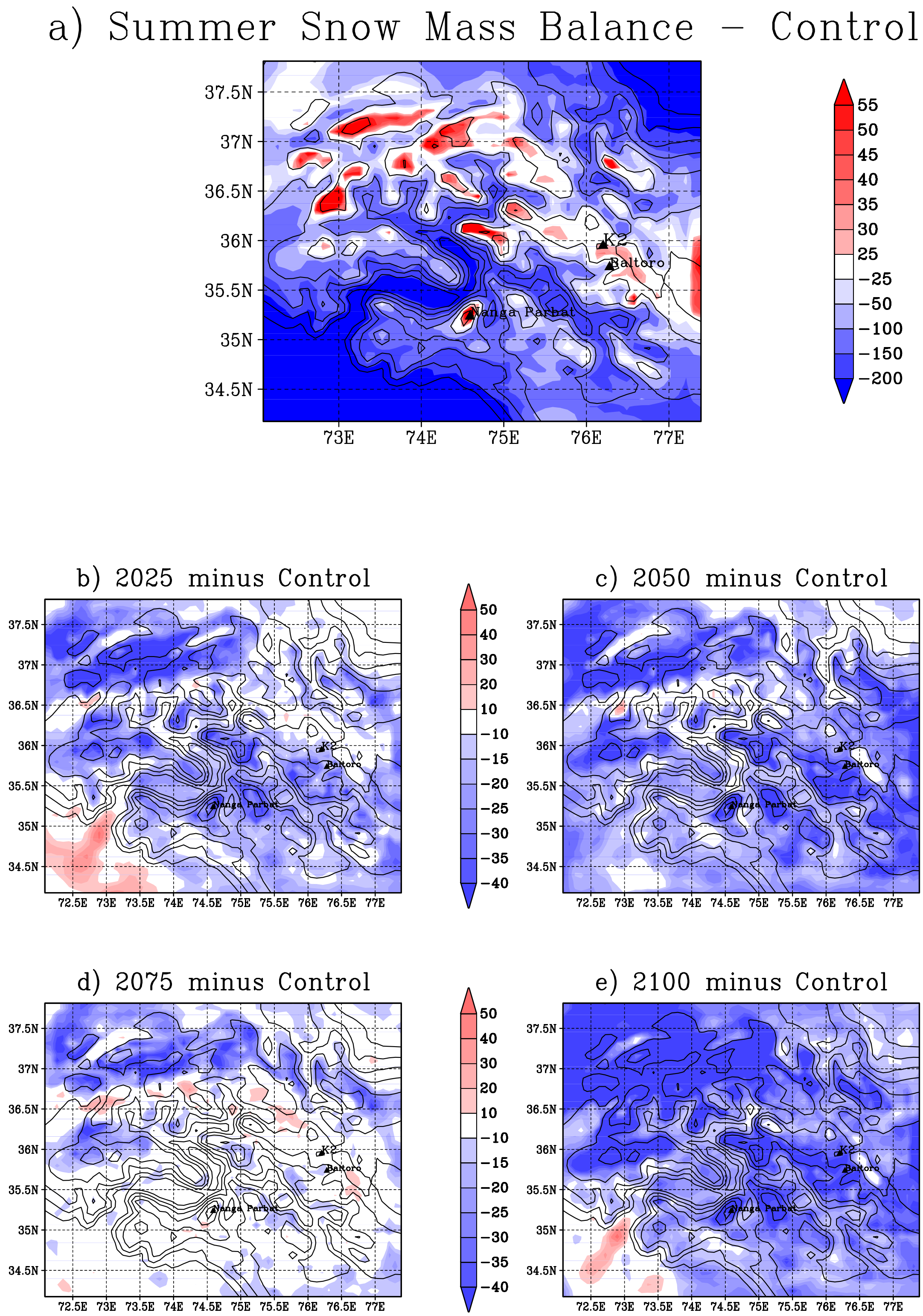

Figure 2.38: a) Snow mass balance during the months of June, July and August (cm water equivalent) for the Control simulation. b) As in a), but for 2025 minus Control. c) As in a), but for 2050 minus Control. d) As in a), but for 2075 minus Control. e) As in a), but for 2100 minus Control.

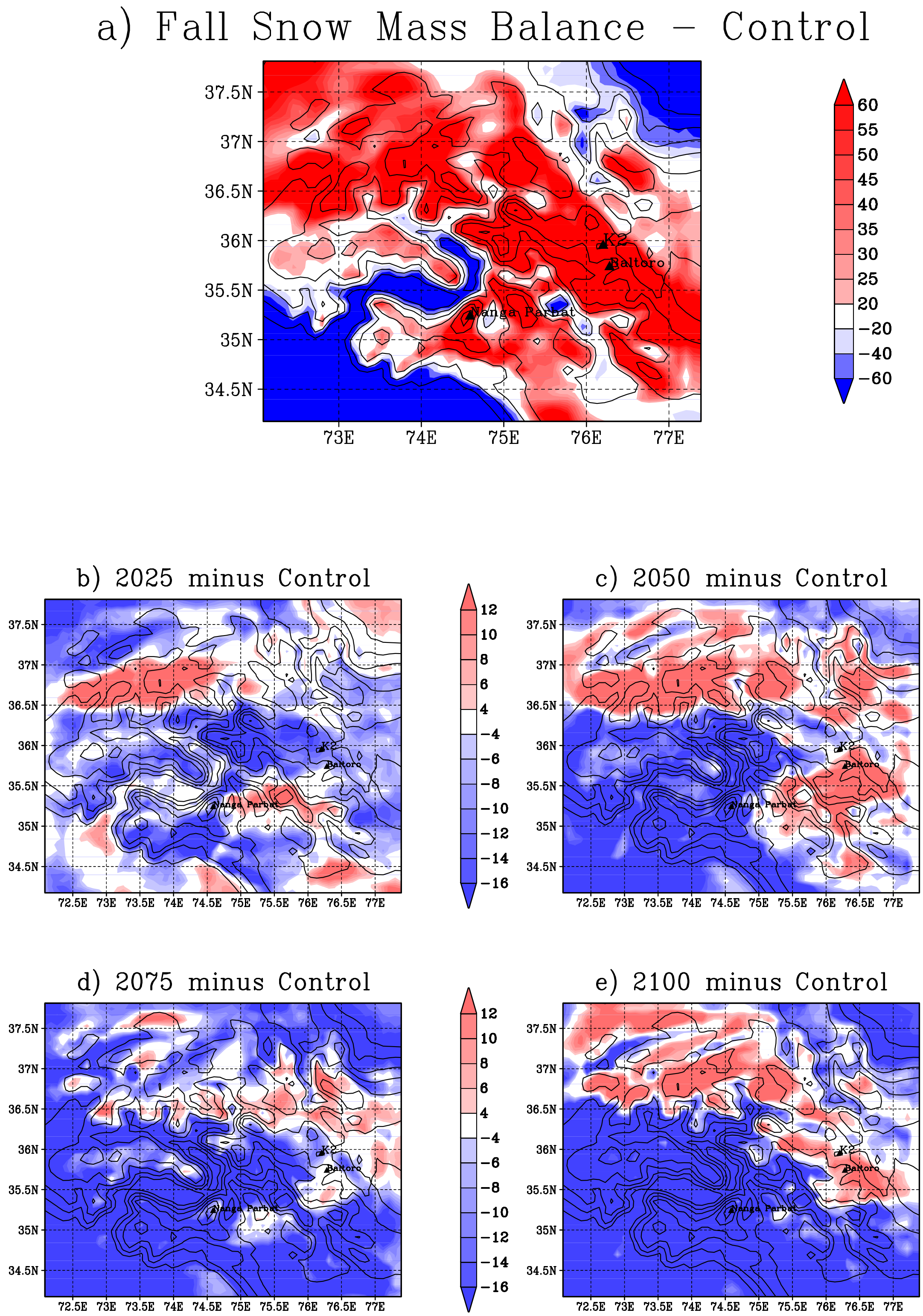

Figure 2.39: a) Snow mass balance during the months of September, October and November (cm water equivalent) for the Control simulation. b) As in a), but for 2025 minus Control. c) As in a), but for 2050 minus Control. d) As in a), but for 2075 minus Control. e) As in a), but for 2100 minus Control.

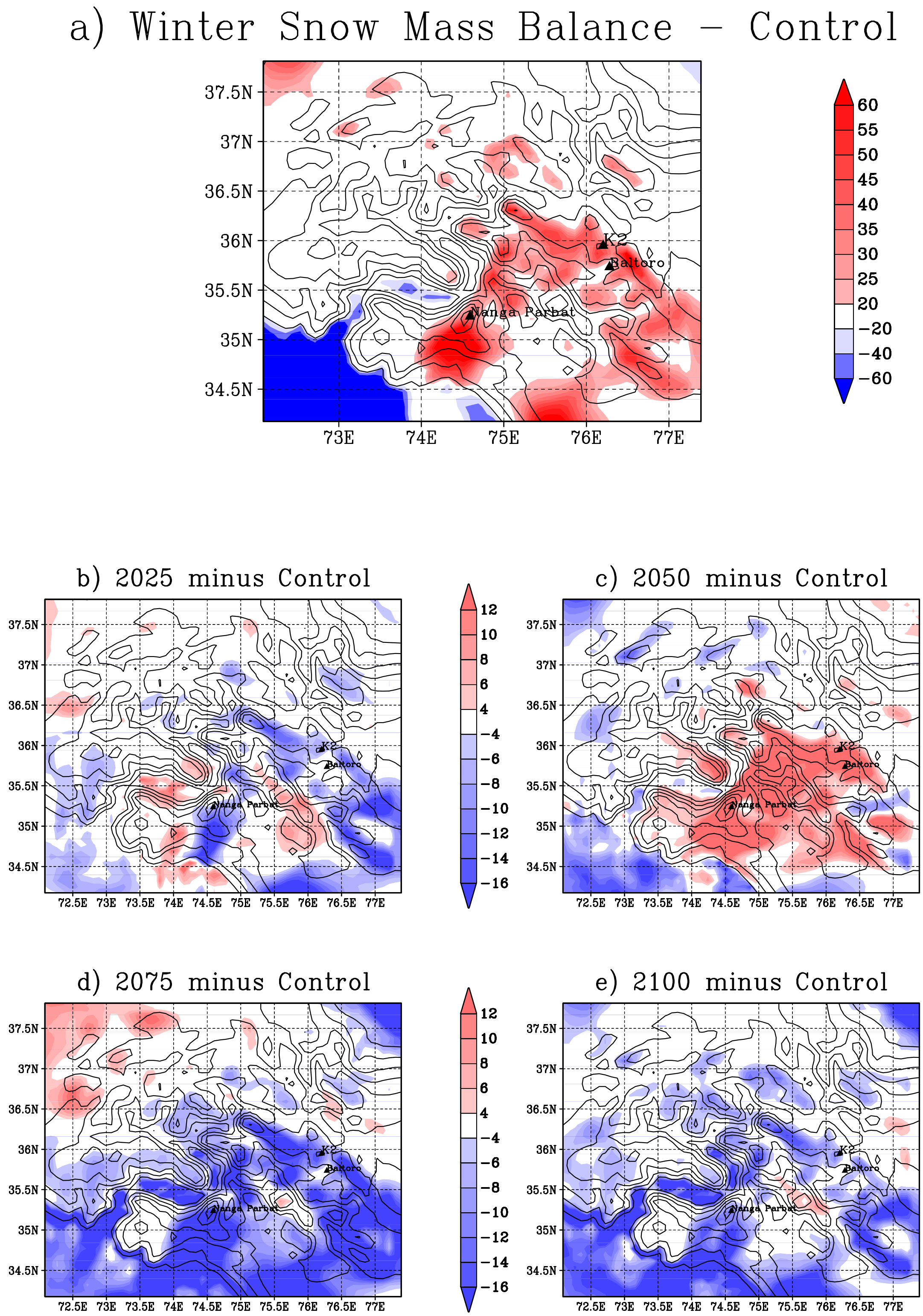

Figure 2.40: a) Snow mass balance during the months of December, January and February (cm water equivalent) for the Control simulation. b) As in a), but for 2025 minus Control. c) As in a), but for 2050 minus Control. d) As in a), but for 2075 minus Control. e) As in a), but for 2100 minus Control.

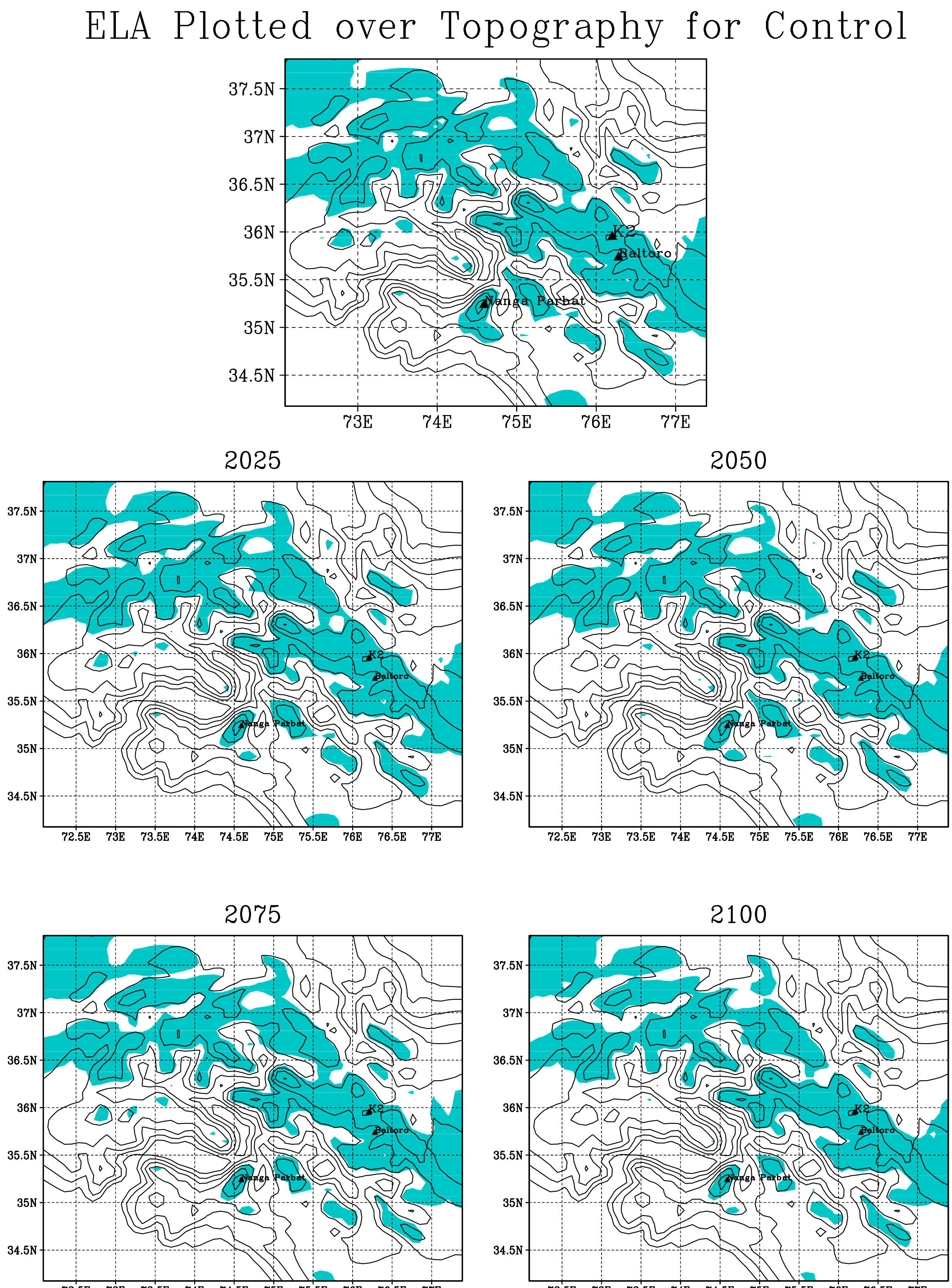

Figure 2.41: a) Equilibrium line altitude (ELA) plotted over topography for the Control simulation. b) As in a), but for 2025 minus Control. c) As in a), but for 2050 minus Control. d) As in a), but for 2075 minus Control. e) As in a), but for 2100 minus Control.

change in mass balance, this method will provide a good approximation for ELA position and evolution under anthropogenic warming. Consistent with the persistence of areas experiencing positive or unchanging snow mass balance under a warming climate (c.f. Fig. 2.36), the position of the ELA is relatively unchanging throughout the 21st century, with only slight fluctuations at lower elevations. The average altitude of the equilibrium line over the entire domain for each time slice calculation is highly variable, with only slight increases in average ELA found by the end of the 21st century (c.f. Table 2.2). The fractional areas of domain 3 that experience positive snow mass balance, or the area enclosed by the equilibrium line, are calculated to be consistently decreasing through the 21st century (c.f. Table 2.2), which is expected under an increasingly warm climate, and concurs with the evolution of snow mass balance in the Karakoram region (c.f. Fig. 2.36).

Table 2.2: Calculated ELA's and Fractional Areas enclosed by Equilibrium Lines

Time Period	Average ELA (m)	Fractional Area of Positive SMB
Control	4417.77	0.390501
2025	4523.51	0.363893
2050	4487.75	0.345122
2075	4515.41	0.345095
2100	4541.79	0.322655

Discussions and Conclusions

Discussions

Studies of the impact of increasing atmospheric CO_2 concentration on global climate through numerical simulations show a similar climate response indicated by the results presented within this study. The magnitude of annually averaged temperature increase (Fig. 2.4), along with the tendency of this temperature anomaly to be larger over continental land mass than neighbouring oceans, is within range of the results portrayed by Manabe & Wetherald (1975), Hansen *et al.* (1981), Manabe *et al.* (1991) and Johns *et al.* (2003).

The results obtained for atmospheric water vapour content and total precipitation trends concur with the suggestion of a more active hydrological with increasing atmospheric CO_2 concentrations made by Manabe & Wetherald (1975), Manabe *et al.* (1991), Johns *et al.* (2003) and Held *et al.* (2006). As mentioned previously, the sensitivity of precipitation increase computed for this study is in agreement with the global-mean precipitation sensitivity computed in the study by Johns *et al.* (2003), which invoked a comparable emission scenario to the one used here. It has been suggested by Ingram (2002) that an increase in water vapour related to increasing temperatures, as seen here, consequently result in small changes in global mean relative humidity, which has been observed as mostly unchanging for the past century (Dai, 2006) and is confirmed in this study (c.f. Fig. 2.8). These small changes in relative humidity, coupled with larger changes in atmospheric water vapour content, leads to the suggestion of a necessary increase in precipitation rate, especially in areas of orographic uplift, under a warming climate (Lorenz & DeWeaver, 2007). Slight variations between each simulation period, as seen in the results for water vapour content and total precipitation, may suggest the influence of multidecadal oscillations, which are not removed when averaging our boundary conditions over 10 year time spans.

In the study of the seasonal climate response to increasing atmospheric CO_2 performed by Manabe *et al.* (1992), it was found that soil moisture in the winter months increased globally, with the exception of regions surrounding 25°N, which experiences a strong decrease. These results are in agreement with winter soil moisture results presented in this study (c.f. Fig. 2.8). During boreal winter months, the midlatitude rainbelt, located at the convergence point of the Ferrel and Polar cells, is located at its lowest latitudes of the year. However, a slight northward shift of the midlatitude rainbelt has been portrayed as a climate response to increased poleward transportation of warm, moist air, resulting from increasing temperatures related to changes in atmospheric CO_2 in studies by Manabe *et al.* (1991,1992) as well as in this study (c.f. Fig. 2.7). This slight northward shift of the midlatitude rainbelt results in a reduction of precipitation in regions that would usually be located in the southernmost portion of the rainbelt, hence the reduction in soil moisture around 25°N in the winter months. In the summer months, Manabe *et al.* (1992) show a decrease in soil moisture on a global scale, with the exception of the Indian subcontinent, over which increases are seen. These results are in agreement with what is portrayed in this study, however our results for summer soil moisture seem to show much more variability than is presented in previous works.

Results obtained for the evolution of ENSO under increasing atmospheric CO_2 concentrations (c.f. Figs. 2.10 and 2.11) concur with the suggestion of a more El Niño-like state of the equatorial Pacific Ocean (Boer, 2004; Vecchi, 2006; Bush, 2007). A gradual warming of the ocean on a global scale, similar to the trends presented here, have been found in past studies of increasing CO_2 concentrations (Stouffer, 2004). A decrease in SLP gradient between the western and eastern tropical Pacific Ocean, as well as suppressed easterly trade winds, have been suggested through observations (Vecchi, 2006) as well as in previous studies simulating impacts of increasing CO_2 (Vecchi, 2006; Bush, 2007). Solely considering the effects of ENSO teleconnections, a shift towards a more El Niño-like state of the Pacific Ocean is expected to result in a more positive NAO through the 21st century, which is not the case presented in our results (c.f. Fig. 2.12). As expected, a weakening of the Asian summer monsoon wind strength is apparent in our results, with the most significant decreases in wind strength occurring after the 2075 simulation (c.f. Fig. 2.13). It should be noted that increases in precipitation described above do not necessarily equate to a strengthening of the monsoonal system, which is why it is necessary to interpret monsoon wind strength as an indicator for Asian summer monsoon evolution through the 21st century. This correlation between ENSO and the summer monsoon concurs with studies of monsoon sensitivity to changes in atmospheric CO_2 (Prell & Kutzbach, 1992). While the continuing uplift of the Tibetan Plateau has been shown to strengthen the Asian monsoon (Trenberth *et al.*, 2000; Zhisheng *et al.*, 2001), the timescale of this response is much too large to resolve any impacts of tectonic uplift in this study.

The seasonality of temperature fluctuations in the trans-Himalayan region (cf. Figs 2.14-2.17) is not in agreement with the observed seasonality of temperature fluctuations for the trans-Himalayan region over the period of 1961-2000 (Archer & Fowler, 2004), in which summer mean temperatures are said to be declining and winter temperatures are said to be increasing, with spring and fall temperature fluctuations of a comparable nature. There is a possibility that this disagreement is arising from the elevation dependency of the simulated temperature signal (Giorgi *et al.*, 1997) and observed temperature fluctuations at higher elevations (Liu & Chen, 2000), which is not captured through observations due to the sparse, valley-floor climate stations used in previous studies (Archer & Fowler, 2004). The study by Liu & Chen (2000), through observations taken from 78 meteorological stations above 2000m above sea level across the Himalayan region, portrays a more remarkable warming trend in the winter half year (October to March), with a stronger estimated warming trend over the Northwestern Tibetan Plateau, which is not confirmed through their study due to limited meteorological stations in the region. This observed winter half year warming could possibly explain the increased warming seen in the March-April-May results presented in this study, suggesting a delayed warming response in the Northwestern Himalaya. The elevation dependency on climate warming presented in our results agrees with the theory of elevation dependency suggested through simulations performed by Giorgi *et al.* (1997), as well as observations by Liu & Chen (2000).

The computed values for the Westerly Index do not indicate a linear evolutionary trend on climate influences in the Karakoram region, however when calculating the Westerly Index, it is difficult to tell whether changes in value are due to westerly or monsoonal variations. A weakening of the summer midlatitude jet under anthropogenic warming, along with a poleward shift consistent with the results presented here, are also suggested in 2XCO_2 simulation studies by Giorgi *et al.* (1992) and Rinke & Dethloff (2008). However, all other variables considered constant, a weakening in the midlatitude jet would in turn reduce the amount of precipitation received in areas of orographic uplift. As mentioned previously, in order to maintain increasing precipitation rates with a weakening midlatitude jet, relative humidity must remain fairly unchanged, which can be seen in Figure 2.6.

Observational analyses over the last five decades have shown an increase in winter precipitation (Hewitt, 2005; Archer & Fowler, 2006), which is not the case in seasonal precipitation results presented in this study. Increases in summer precipitation have been observed in climate station data (Archer & Fowler, 2006), but again, the opposite is occurring in our simulation results. One point of consistency in the results for precipitation is the presence of a rain shadow to the north-northwest of Nanga Parbat, the existence of which is stated by Phillips *et al.* (2000). The differences between simulated and observed seasonal precipitation are speculated to arise from the sparsity of data in the highly elevated regions of the Himalaya, and hence cannot be attributed to the performance of the regional model.

Annual snowfall accumulation results suggest an increase in snowfall accumulation at the highest altitudes of the Karakoram region, most prominently surrounding the peak of K2 (c.f. Fig. 2.24). These simulated increases in annual snowfall accumulation agree with observations by Bitz & Battisti (1999) and Box *et al.* (2006) that increasing global temperatures, and hence increases in precipitation, if located at high enough elevations will result in increased snowfall accumulation that can potentially offset the negative correlation between increasing temperatures and glacial mass balance.

Increasing incident long and short wave radiation results, along with the evolution of low, mid and high level cloud cover, are expected under a warming climate. Increases in incident short wave radiation are indirectly correlated with increases in temperature, arising from changes in lower level cloud, whereas increases in incident long wave radiation are directly related to increases in Earth's surface temperature, which regulates the amount of long wave radiation emitted upwards. In the results presented here, there are small scale occurrences of decreasing incident short wave radiation at the highest elevations within the study region, arising from increased snowfall and reflection of short wave radiation due to the high albedo of new snow, indicating a reversed role of the snow-albedo feedback mechanism seen in other alpine glaciers around the world. Both long and short wave radiation are altered by the presence of lower and higher level cloud cover, respectively. Under an increasingly moist climate, a shift towards more higher level clouds and less lower level clouds due to increased convection is expected, which is partially the case presented here. High level clouds are shown to increase until the 2075 simulation, after which a sharp decrease is apparent (c.f. Fig. 2.29), which does not correlate with the persistent increase in incident long wave radiation (c.f. Fig. 2.27). The evolution of rainfall accumulation and sensible heat flux are also expected results under a warming climate, as increases in temperature will allow for the transition of precipitation type from snow to rain, as well as an increase in sensible heat flux throughout most of the region, both of which have negative effects on the life span of Karakoram glaciers.

Results for snow mass balance, which suggest areas of positive snow mass balance correlating to areas of increased snowfall accumulation, are consistent with the findings of the observational study by Bitz and Battisti (1999) in which a strong positive correlation was found between snow mass balance and precipitation anomalies, with weaker negative correlations between snow mass balance and temperature anomalies for alpine glaciers throughout the Canadian Rockies. Due to the lack of available data it is difficult to compare these findings to observational studies for the Karakoram region, however positive glacial mass balance correlated with increases in precipitation has been recorded by Hewitt (2005), which is contradictory to global trends in alpine glacial evolution (Oerlemans, 2005). Glacial changes asynchronous to world wide trends have also been observed in previous time periods for areas surrounding Nanga Parbat (Phillips *et al*, 2000). Increasing snowfall trends at high elevations under a warming climate, arising from increases in precipitation predominantly falling as snow, have also been found for the Greenland icesheet (Box *et al.*, 2006) as well as the Rocky Mountains and Alaska (Bitz & Battisti, 1999). Future climate scenario studies performed over the Western United States have suggested that this increasing trend in snowfall accumulation will continue with increased anthropogenic warming (Kim *et al.*, 2002). The relatively unchanging ELA during the 21st century, consistent with the results for annual snow mass balance, further confirms the strong positive correlation between mass balance and precipitation anomalies, which outweighs the negative correlation between mass balance and temperature anomalies, suggested by Bitz & Battisti (1999).

Conclusions

Contrary to observations of world wide glacial retreat (Oerlemans, 2005), and despite simulated temperature changes throughout the study region, the highly elevated regions of the Karakoram mountain range experience positive snow mass balance until the end of the 21st century due to the strong positive correlation between snow mass balance and simulated increases in precipitation falling predominantly as snow. The strong elevation signal seen in the calculated snow mass balance illustrates the importance of elevation on net snow accumulation, as well as the need for high resolution models when performing numerical climate simulations in the presence of high topography. Although the results presented in this study suggest conditions for positive glacial mass balance under a warming climate, glacial expansion and surge events are not necessarily a guaranteed outcome. The models employed in this study do not take into account the effect of internal glacial dynamics on mass balance, which can play a major role in the downwasting or surging of alpine glaciers. In order to infer how glacial flow will evolve under increasing atmospheric CO_2 concentrations, hydrological and glaciological modelling experiments must be performed, using the results presented in this study as a basis for comparison. To obtain a more accurate representation of glacial evolution in a changing climate, it would be beneficial to account for not only increases in atmospheric CO_2, but increases in other anthropogenic as well as natural atmospheric constituents that are known to promote global climate change. Nevertheless, this study provides some essential aspects of climate change in highly elevated areas such as the Karakoram region, namely the relationship between increases in temperature and atmospheric water vapour content due to increasing atmospheric CO_2, resulting in more precipitation falling as glacier-nourishing snow. Throughout the 21st century, increases in snowfall result in areas of positive glacial mass balance at the highest elevations through the Karakoram, indicating a reversed role of the snow-albedo feedback mechanism that has been deemed the culprit of world wide high elevation glacial recession. Accurate global and regional climate modelling of the world's glaciers has the potential to predict changes in the hydrological cycle of surrounding regions that depend greatly on glacial runoff as a freshwater resource by accurately predicating glacier termini, thickness, and future glacial dynamics. Understanding the evolution of these glaciers under a warming climate is key to unravelling the effects climate change will have on the well-being of civilization.

References

Alexander, B.P., Elena, N.V., 1992. The NAO and ENSO teleconnection. *TOGA*, **note 6**, 10-11.

Archer, D.R. & Fowler, H.J., 2004. Spatial and temporal variations in precipitation in the Upper Indus Basin, global teleconnections and hydrological implications. *Hydrology and Earth Sciences*, **8**, 47-61.

Archer, D.R. & Fowler, H.J., 2006. Conflicting signals of climatic change in the Upper Indus Basin. *Journal of Climate*, **19**, 4276-4293.

Bitz, C.M. & Battisti, D.S., 1999. Interannual to Decadal Variability in Climate and the Glacier Mass Balance in Washington, Western Canada and Alaska. *Journal of Climate*, **12**, 3181-3196.

Boer, G.J., Kim, S., Flato, G.M., 2004. Is there observational support fo an El Niño-like pattern of future global warming? *Geophysical Research Letters*, **31**, L06201.

Box, J.E., Bromwich, D.H., Veenhuis, B.A., Bai, L.S., Stroeve, J.C., Rogers, J.C., Steffen, K., Haran, T., Wang, S.H., 2006. Greenland ice sheet surface mass balance variability (1988-2004) from calibrated polar MM5 output. *Journal of Climate*, **19**, 2783-2800.

Bromwich, D.H., Bai, L., & Bjarnason, G.G., 2005. High-resolution regional climate simulations over Iceland using Polar MM5. *Monthly Weather Review*, 3527-3547.

Bush, A.B.G. & Philander, S.G., 1998. The role of ocean-atmosphere interactions in tropical cooling during the Last Glacial Maximum. *Science*, **279**, 1341-1344.

Bush, A.B.G., 2000. A positive climatic feedback mechanism for Himalayan glaciation. *Quaternary International*, **65/66**, 3-13.

Bush, A.B.G., 2004. Modelling of late Quaternary climate over Asia: a synthesis. *Boreas*, **33**. 155-163.

Bush, A.B.G., 2007. Extratropical Influences on the El Niño-Southern Oscillation through the Late Quaternary. *Journal of Climate*, **20**, 788-800.

Cai, W. & Whetton, P.H., 2000. Evidence for a time-varying pattern of greenhouse warming in the Pacific Ocean. *Geophysical Research Letters*, **27**, 2577-2580.

Calanca, P., 2001. A note on the roughness length over melting snow and ice. *Journal of the Royal Meteorological Society*, **127**, 255-260.

Callendar, G.S., 1938. The Artificial Production of Carbon Dioxide and its Influence on Temperature. *Quarterly Journal of the Royal Meteorological Society*, **64**, 223-240.

Callendar, G.S., 1949. Can carbon dioxide influence the climate? *Weather*, **4**, 310-314.

Chen, F. & Dudhia, J., 2001. Coupling an advanced land surface-hydrology model with the Penn State-NCAR MM5 modeling system. Part I: Model implementation and sensitivity. *Monthly Weather Review*, **129**, 569-585.

Chen, F. & Dudhia, J., 2001. Coupling an advanced land surface-hydrology model with the Penn State-NCAR MM5 modeling system. Part II: Preliminary model validation. *Monthly Weather Review*, **129**, 587-604.

Chen, X., Kimoto, M., Takahashi, M., 2005. Changes in ENSO in response to greenhouse warming as simulated by the CCSR/NIES/FRCGC coupled GCM. *SOLA*, textbf1, 149-152.

Copland, L., Pope, S., Bishop, M.P., Shroder, J.F., Clendon, P., Bush, A., Kamp, U., Seong, U.B., Owen, L.A., 2009. Glacier velocities across the Central Karakoram. *Annals of Glaciology*, **50**, 41-49.

Cubasch, U., Meehl, G.A., Boer, G.J., Stouffer, R.J., Dix, M., Noda, A., Senior, C.A., Raper, S., Yap, K.S., 2001. Projections of future climate change. In: Houghton, J.T., Ding, Y., Griggs, D.J., Noguer, M., van der Linden, P., Dai, X., Maskell, K., Johnson, C.I., (eds) Climate change 2001: the scientific basis. Contribution of working group I to the 3rd assessment report of the intergovernmental panel on climate change. *Cambridge University Press, Cambridge*, 525-582.

Dai, A., 2006. Recent Climatology, Variability and Trends in Global Surface Humidity. *Journal of Climate*, **19**, 3589-3606.

Dickinson, R.E., Errico, R.M., Giorgi, F., & Bates, G.T., 1989. A regional climate model for the western United States. *Climatic Change*, **15**, 383-422.

Dugam, S.S., Kakade, S.B., Verma, R.K., 1997. Interannual and Long-term Variability in the North Atlantic Oscillation and Indian Summer Monsoon Rainfall. *Theoretical and Applied Climatology*, **58**, 21-29.

Dyurgerov, M., 2003. Mountain and subpolar glaciers show an increase in sensitivity to climate warming and intensification of water cycle. *Journal of Hydrology*, **282**, 164-176.

Giorgi, F., 1990. Simulation of Regional Climate Using a Limited Area Model Nested in a General Circulation Model. *Journal of Climate*, **3**, 941-963.

Giorgi, F., Marinucci, M.R., Visconti, G., 1990. Use of a limited-area model nested in a general circulation model for regional climate simulation over Europe. *Journal of Geophysical Research*, **95**, 18413-18431.

Giorgi, F., Marinucci, M.R., Visconte, G., 1992. A 2XCO_2 Climate Change Scenario Over Europe Generated Using a Limited Area Model Nesting in a General Circulation Model 2. Climate Change Scenario. *Journal of Geophysical Research*, **97**, 10011-10028.

Giorgi, F., Hurrell, J.W., Marinucci, M.R., 1997. Elevation Dependency of the Surface Climate Change Signal: A Model Study. *Journal of Climate*, **10**, 288-296.

Gordon, C.T., & Stern, W.F., 1982. A description of the GFDL Global Spectral Model. *Monthly Weather Review*, 625-644.

Hansen, J., Johnson, D., Lacis, A., Lebedeff, S., Lee, P., Rind, D., Russel, G., 1981. Climate Impact of Increasing Atmospheric Carbon Dioxide. *Science*, **213**, 957-966.

Haritashya, U.K., Bishop, M.P., Shroder, J.F., Bush, A.B.G., Bulley, H.N.N., 2009. Space-based assessment of glacier fluctuations in the Wakhan Pamir, Afghanistan. *Climate Change*, **94**, 5-18.

Held, I.M. & Soden, B.J., 2006. Robust Responses of the Hydrological Cycle to Global Warming. *Journal of Climate*, **19**, 5686-5699.

Hernandez, J.L., Srikishen, J., Erickson, D.J., Oglesby, R., & Irwin, D., 2006. A regional climate study of Central America using the MM5 modeling system: Results and comparison to observations. *International Journal of Climatology*, **26**, 2161-2179.

Hewitt, K., 2005. The Karakoram Anomaly? Glacier Expansion and the 'Elevation Effect', Karakoram, Himalaya. *Mountain Research and Development*, **25**, 332-340.

Hewitt, K., 2007. Tributary glacier surges: an exceptional concentration at Panmah Glacier, Karakoram Himalaya. *Journal of Glaciology*, **53**, 181-188.

Hock, R., 2003. Temperature index modelling in mountain areas. *Journal of Hydrology*, **282**, 104-115.

Ingram W.J., 2002. On the robustness of the water vapour feedback: GCM vertical resolution and formulation. *Journal of Climate*, **15**, 917-921.

IPCC (Intergovernmental Panel on Climate Change), 2007: IPCC WG1 AR4 Report. Retrieved Dec 2009. [Available online at http://ipcc-wg1.ucar.edu/wg1/wg1-report.html].

Ji, Y. & Vernekar, A.D., 1997. Simulation of the Asian summer monsoons of 1987 and 1988 with a regional model nested in a global GCM. *Journal of Climate*, **10**, 1965-1979.

Johns, T.C., Gregory, J.M., Ingram, W.J., Johnson, C.E., Jones, A., Lowe, J.A., Mitchell, J.F.B., Roberts, D.L., Sexton, D.M.H., Stevenson, D.S., Tett, S.F.B., Woodage, M.J., 2003. Anthropogenic climate change for 1860 to 2100 simulated with the HadCM3 model under updated emission scenarios. *Climate Dynamics*, **20**, 583-612.

Kalnay, E., Kanamitsu, M., Kistler, R., Collins, W., Deaven, D., Gandin, L., Iredell, M., Saha, S., White, G., Woollen, J., Zhu, Y., Chelliah, M., Ebisuzaki, W., Higgins, W., Janowiak, J., Mo, K.C., Ropelewski, C., Wang J., Leetmaa, A., Reynolds, R., Jenne, R., & Joseph, D. The NCEP/NCAR 40-Year Reanalysis Project. *Bulletin of the American Meteorological Society*, 437-471.

Kim, J., Kim, T., Arritt, R., Miller, N., 2002. Impacts of Increased Atmospheric CO_2 on the Hydroclimate of the Western United States. *Journal of Climate*, **15**, 1926-1942.

Lorenz, D., DeWeaver, E., 2007. The Response of the Extratropical Hydrological Cycle to Global Warming. *Journal of Climate*, **20**, 3470-3484.

Liu, X. & Chen, B., 2000. Climatic warming in the Tibetan Plateau during recent decades. *International Journal of Climatology*, **20**, 1729-1742.

Manabe, S. & Wetherald, R.T., 1975. The effects of doubling the CO_2 concentration on the climate of a general circulation model. *Journal of Atmospheric Science*, **32**, 3-15.

Manabe, S., Stouffer, R.J., Spelman, M.J., Bryan, K., 1991. Transient Responses of a Coupled Ocean-Atmosphere to Gradual Changes of Atmospheric CO_2. Part I: Annual Mean Response. *Journal of Climate*, **4**, 785-818.

Manabe, S., Spelman, M.J., Stouffer, R.J., 1992. Transient Responses of a Coupled Ocean-Atmosphere to Gradual Changes of Atmospheric CO_2. Part II: Seasonal Response. *Journal of Climate*, **4**, 785-818.

Manabe, S. & Stouffer, R.J., 1994. Multi-Century Response of a Coupled Ocean-Atmosphere Model to an Increase of Atmospheric Carbon Dioxide. *Journal of Climate*, **7**, 5-23.

Meehl, G.A. & Washington, W.M., 1996. El Niño-like climate change in a model with increased atmospheric CO_2 concentrations. *Nature*, **382**, 56-60.

Molnia, B.F., 2007. Late nineteenth to early twenty-first century behavior of Alaskan glaciers as indicators of changing regional climate. *Global and Planetary Change*, **56** , 23-56.

Munro, S., 1991. A surface energy exchange model of glacier melt and net mass balance. *Journal of Climatology*, **11**, 689-700.

Oerlemans, J., 2005. Extracting a Climate Signal from 169 Glacier Records. *Science*, **308**, 675-677.

Pacanowski, R.C., 1995. MOM 2 documentation: Users guide and reference manual, Version 1.0. *GFDL Ocean Group Technical Report No. 3*, Geophysical Fluid Dynamics Laboratory, Princeton, New Jersey.

Phillips, W.M., Sloan, V.F., Shroder Jr., J.F., Sharma, P., Clarke, M.L., Rendell, H.M., 2000. Asynchronous glaciation at Nanga Parbat, northwestern Himalaya Mountains, Pakistan. *Geology*, **28**, 431-434.

Prell, W. & Kutzbach, J., 1992. Sensitivity of the Indian monsoon to forcing parameters and implications for its evolution. *Nature*, **360**, 647-652.

Qian, J.H., Seth, A., Zebiak, S., 2003. Reinitialized versus Continuous Simulations for Regional Climate Downscaling. *Monthly Weather Review*, **131**, 2857-2874.

Reisner, J., Rasmussen, R.M., & Bruintjes, R.T., 1998. Explicit forecasting of supercooled liquid water in winter storms using the MM5 mesoscale model. *Q.J.R. Meteorol. Soc.*, **124**, 1071-1107.

Rinke A. & Dethloff, K., 2008. Simulated circum-Arctic climate changes by the end of the 21st century. *Global and Planetary Change*, **62**, 173-186.

Salerno, F., Buraschi, E., Bruccoleri, G., Tartari, G., Smirgalia, C., 2008. Glacier surface-area changes in Sagarmatha national park, Nepal, in the second half of the 20th century, by comparison of historical maps. *Journal of Glaciology*, **54**, 738-752.

Seong, Y.B., Owen, L.A., Bishop, M.P., Bush, A., Clendon, P., Copland, L., Finkel, R., Kamp, U., Shroder, J.F., 2007. Quaternary glacial history of the Central Karakoram. *Quaternary Science Reviews*, **26**, 3384-3405.

Seong, Y.B., Owen, L.A., Caffee, M.W., Kamp, U., Bishop, M.P., Bush, A.,, Copland, L., Shroder, J.F., 2009. Rates of basin-wide rockwall retreat in the K2 region of the Central Karakoram defined by terrestrial cosmogenic nuclide ^{10}Be. *Geomorphology*, **107**, 254-262.

Singh, D. & Ganju, A., 2008. Mountain range specific analog weather forecast model for Northwest Himalaya in India. *J. Earth Syst. Sci.*, **117**, 575-587.

Thompson, D.W.J. & Wallace, J.M., 2001. Regional Climate Impacts of the Northern Hemisphere Annular Mode. *Science*, **293**, 85-89.

Thompson, L.G., Yao, T., Mosley-Thompson, E., Davis, M.E., Henderson, K.A., Lin, P.N., 2000. A high-resolution millennial record of the South Asian Monsoon from Himalayan ice cores. *Science*, **289**, 1916-1919.

Timmerman, A.J., Oberhuber, J., Bacher, A., Esch, M., Latif, M., Roeckner, E., 1999. Increased El Niño frequency in a climate model forced by future greenhouse warming. *Nature*, **398**, 694-696.

Trenberth, K.E., Stepaniak, D.P., Caron, J.M., 2000. The Global Monsoon as seen through the divergent atmospheric circulation. *Journal of Climate*, **13**, 3969-3993.

Troen, I.B., & Mahrt, L., 1986. A simple model of the atmospheric boundary layer; sensitivity to surface evaporation. *Boundary-Layer Meteorology,* **37**, 129-148.

Vecchi, G.A., Soden, B.J., Wittenberg, A.T., Held, I.M., Leetmaa, A., 2006. Weakening of tropical Pacific atmospheric circulation due to anthropogenic forcing. *Nature*, **441**, 73-76.

Visbeck, M.H., Hurrell, J.W., Polvani, L., Cullen, H.M., 2001. The North Atlantic Oscillation: Past, present, and future. *PNAS*, **98**, 12876-12877.

Warren, S., 1982. Optical properties of snow. *Reviews of Geophysics*, **20**, 67-89.

Yanfeng, Z. & Longxun, C., 2002. The relationship between the Asian/Australian Monsoon and ENSO on a Quasi-Four-Year Scale. *Advances in Atmospheric*

Sciences, **19**, 727-739.

Zemp, M., Haeberli, W., Hoelzle, M., Paul, F., 2006. Alpine glaciers to disappear within decades? *Geophysical Research Letters*, **33**, L13504.

Zhisheng, A., Kutzbach, J., Prell, W., Porter, S., 2001. Evolution of Asian monsoons and phased uplift of the Himalaya-Tibetan plateau since Late Miocene times. *Nature*, **411**, 62-66.

Appendix A

MM5 Model Equations

As seen in the PSU/NCAR Mesoscale Modelling System Tutorial Class Notes and User's Guide, the basic governing equations for variables of the nonhydrostatic component of MM5 are shown below, in terms of terrain following coordinates (x,y,σ). Brief derivations of these equations can be found in Appendix B. Because we are interested in nonhydrostatic processes, it is necessary to define constant reference states, with perturbations from this reference state, for each variable in question, as follows (as seen in Grell *et al.*, 1994):

$$p(x,y,z,t) = p_o(z) + p^{'}(x,y,z,t) \tag{3.6}$$

$$T(x,y,z,t) = T_o(z) + T^{'}(x,y,z,t) \tag{3.7}$$

$$\rho(x,y,z,t) = \rho_o(z) + \rho^{'}(x,y,z,t) \tag{3.8}$$

where p is pressure, T is temperature, ρ is density, p_o, T_o and ρ_o are the reference states, and $p^{'}$, $T^{'}$ and ρ' are the perturbations from their respective reference states.

Pressure

$$\frac{\partial p^{'}}{\partial t} - \rho_o g w + \gamma p \nabla \cdot \vec{\mathbf{u}} = -\vec{\mathbf{u}} \cdot \nabla p^{'} + \frac{\gamma p \dot{Q}}{T c_p} \tag{3.9}$$

where g is acceleration due to gravity, w is the vertical component of velocity, γ is the ratio of the specific heat capacity at constant pressure to the specific heat capacity at constant volume (taken as 1.4), $\vec{\mathbf{u}}$ is the velocity field in vector notation, $\dot{Q}$ is the time rate of change of heat flux, and c_p is the specific heat capacity at constant pressure.

Thermodynamics

$$\frac{\partial T}{\partial t} = -\vec{\mathbf{u}} \cdot \nabla T \ + \ \frac{1}{\rho c_p}\left(\frac{\partial p^{'}}{\partial t} + \vec{\mathbf{u}} \cdot \nabla p^{'} - \rho_o g w\right) + \frac{\dot{Q}}{c_p} \tag{3.10}$$

Momentum (x - component)

$$\frac{\partial u}{\partial t} + \frac{m}{\rho}\left(\frac{\partial p^{'}}{\partial x} - \frac{\sigma}{p^*}\frac{\partial p^*}{\partial x}\frac{\partial p^{'}}{\partial \sigma}\right) = -\vec{\mathbf{u}} \cdot \nabla u + v\left(f + u\frac{\partial m}{\partial y} - v\frac{\partial m}{\partial x}\right) - ew\cos\alpha - \frac{uw}{r_e} + D_u \tag{3.11}$$

where u is the zonal component of velocity, v is the meridional component of velocity, m is the map scale factor implemented by MM5, p^* is the pressure difference between the model surface and the model top, f is the Coriolis parameter, r_e is the radius of Earth, and D_u represents the zonal component of a diffusion term. The third to last term, where e is given as $2\Omega \cos \lambda$, where λ is latitude and α is the degree of deviation from a central longitude, represents a component to the Coriolis force that is usually neglected, and essentially accounts for the slight tilt in Earth's rotational axis (more details regarding this term can be found in Appendix B, equation 3.50). The second to last term accounts for centripetal acceleration arising from the curvature of the Earth.

Momentum (y - component)

$$\frac{\partial v}{\partial t}+\frac{m}{\rho}\left(\frac{\partial p'}{\partial y}-\frac{\sigma}{p^*}\frac{\partial p^*}{\partial y}\frac{\partial p'}{\partial \sigma}\right)=-\vec{\mathbf{u}}\cdot\nabla v-u\left(f+u\frac{\partial m}{\partial y}-v\frac{\partial m}{\partial x}\right)+ew\sin\alpha-\frac{vw}{r_e}+D_v \tag{3.12}$$

where D_v represents the meridional component of a diffusion term.

Momentum (z - component)

$$\frac{\partial w}{\partial t}-\frac{\rho_o}{\rho}\frac{g}{p^*}\frac{\partial p'}{\partial \sigma}+\frac{g}{\gamma}\frac{p'}{p}=-\vec{\mathbf{u}}\cdot\nabla w+g\frac{p_o}{p}\frac{T'}{T_o}-\frac{gR_d}{c_p}\frac{p'}{p}+e(u\cos\alpha-v\sin\alpha)+\frac{u^2+v^2}{r_e}+D_w \tag{3.13}$$

where R_d is the gas constant for dry air, and D_w represents the vertical component of a diffusion term.

Within the above equations, the advection terms for variable "A" can be expanded as:

$$\vec{\mathbf{u}}\cdot\nabla A\equiv mu\frac{\partial A}{\partial x}+mv\frac{\partial A}{\partial y}+\dot{\sigma}\frac{\partial A}{\partial \sigma} \tag{3.14}$$

where

$$\dot{\sigma}=-\frac{\rho_o g}{p^*}w-\frac{m\sigma}{p^*}\frac{\partial p^*}{\partial y}v \tag{3.15}$$

and the divergence terms for variable "A" can be expanded as:

$$\nabla \cdot \vec{\mathbf{u}} \equiv m^2 \frac{\partial}{\partial x}\left(\frac{u}{m}\right) - \frac{m\sigma}{p^*}\frac{\partial p^*}{\partial x}\frac{\partial u}{\partial \sigma} + m^2 \frac{\partial}{\partial y}\left(\frac{v}{m}\right) - \frac{m\sigma}{p^*}\frac{\partial p^*}{\partial y}\frac{\partial v}{\partial \sigma} - \frac{\rho_o g}{p^*}\frac{\partial w}{\partial \sigma} \quad (3.16)$$

The σ-coordinate is related to pressure by the following equation:

$$\sigma = \frac{p_o - p_{top}}{p^*} \quad (3.17)$$

Appendix B

MM5 Model Equation Derivations

Derivation of the Pressure Tendency Equation

Starting with the ideal gas law in terms of density, given as

$$p = \rho R T \tag{3.18}$$

the material derivative is taken, and the result is rearranged to get

$$\frac{1}{p}\frac{Dp}{Dt} = \frac{1}{\rho}\frac{D\rho}{Dt} + \frac{1}{T}\frac{DT}{Dt} \tag{3.19}$$

Applying the first law of thermodynamics including terms of advection, given as

$$c_p \frac{DT}{Dt} = \frac{1}{\rho}\frac{Dp}{Dt} + \dot{Q} \tag{3.20}$$

it is possible to eliminate $\frac{DT}{Dt}$, and equation 3.19 becomes

$$\frac{1}{p}\frac{Dp}{Dt} = \frac{1}{\rho}\frac{D\rho}{Dt} + \frac{1}{T}\left(\frac{1}{c_p\rho}\frac{Dp}{Dt} + \frac{\dot{Q}}{c_p}\right) \tag{3.21}$$

The use of the continuity equation, shown below, to eliminate $\frac{D\rho}{Dt}$

$$\frac{D\rho}{Dt} = -\rho\nabla\cdot\vec{\mathbf{u}} \tag{3.22}$$

and equation 3.21 becomes

$$\frac{1}{p}\frac{Dp}{Dt} = -\nabla\cdot\vec{\mathbf{u}} + \frac{\dot{Q}}{c_pT} + \frac{1}{c_p\rho T}\frac{Dp}{Dt} \tag{3.23}$$

which, when like terms are combined, results in

$$\frac{Dp}{Dt}\left(\frac{1}{p} - \frac{1}{c_p\rho T}\right) = -\nabla\cdot\vec{\mathbf{u}} + \frac{\dot{Q}}{c_pT} \tag{3.24}$$

The term in brackets can then be rewritten, with help from the ideal gas law, as

$$\frac{1}{p}\left(1 - \frac{R}{c_p}\right) \tag{3.25}$$

which can then be further simplified by implementing the knowledge that $R = c_p - c_v$, and that the ratio of specific heat capacities $\frac{c_p}{c_v}$ is given by a constant γ, whose value is taken as 1.4. Therefore, equation 3.24 becomes

$$\frac{1}{p}\frac{Dp}{Dt}\left(\frac{1}{\gamma}\right) = -\nabla\cdot\vec{\mathbf{u}} + \frac{\dot{Q}}{c_pT} \tag{3.26}$$

which can then be rearranged into the form

$$\frac{Dp}{Dt} = -\gamma p\nabla\cdot\vec{\mathbf{u}} + \frac{\gamma p\dot{Q}}{c_pT} \tag{3.27}$$

Next, the material derivative is expanded to obtain

$$\frac{\partial p}{\partial t} + \vec{\mathbf{u}} \cdot \nabla p = -\gamma p \nabla \cdot \vec{\mathbf{u}} + \frac{\gamma p \dot{Q}}{c_p T} \tag{3.28}$$

which, when rearranged, becomes

$$\frac{\partial p}{\partial t} + \gamma p \nabla \cdot \vec{\mathbf{u}} = -\vec{\mathbf{u}} \cdot \nabla p + \frac{\gamma p \dot{Q}}{c_p T} \tag{3.29}$$

Applying equation 3.6, in order to account for nonhydrostatic processes, equation 3.29 then becomes

$$\frac{\partial p^{'}}{\partial t} + \gamma p \nabla \cdot \vec{\mathbf{u}} = -\left(\vec{\mathbf{u}} \cdot \nabla p_o + \vec{\mathbf{u}} \cdot \nabla p^{'}\right) + \frac{\gamma p \dot{Q}}{c_p T} \tag{3.30}$$

where the term inside the brackets can be expanded as

$$w \frac{\partial p_o}{\partial z} + \vec{\mathbf{u}} \cdot \nabla p^{'} \tag{3.31}$$

By implementing hydrostatic balance equation, given as

$$\frac{\partial p_o}{\partial z} = -\rho_o g \tag{3.32}$$

the terms in equation 3.31 become

$$-\rho_o g w + \vec{\mathbf{u}} \cdot \nabla p^{'} \tag{3.33}$$

and equation 3.30 results in

$$\frac{\partial p^{'}}{\partial t} + \gamma p \nabla \cdot \vec{\mathbf{u}} = \rho_o g w - \vec{\mathbf{u}} \cdot \nabla p^{'} + \frac{\gamma p \dot{Q}}{c_p T} \tag{3.34}$$

which, when rearranged, becomes the equation for pressure tendency given by equation 3.9 in Appendix A.

$$\frac{\partial p^{'}}{\partial t} - \rho_o g w + \gamma p \nabla \cdot \vec{\mathbf{u}} = -\vec{\mathbf{u}} \cdot \nabla p^{'} + \frac{\gamma p \dot{Q}}{T c_p} \tag{3.35}$$

Derivation of the Thermodynamics Equation

The first law of thermodynamics, when applying the ideal gas law and the fact that $R = c_p - c_v$ can be written as

$$dQ = c_v dT + p dv = c_p dT - v dp \tag{3.36}$$

From here, since we are dealing with specific heat capacities, a per unit mass convention is adopted, which allows the definition of α as

$$\alpha = \frac{v}{m} = \frac{v}{1} \equiv \frac{1}{\rho} \tag{3.37}$$

and hence, equation 3.36 becomes

$$dQ = c_v dT + p d\alpha = c_p dT - \alpha dp \tag{3.38}$$

Rewriting the right hand equivalency in equation 3.38, and taking the time derivative, results in

$$\dot{Q} = c_p \frac{dT}{dt} - \alpha \frac{dp}{dt} \tag{3.39}$$

which, when applying equation 3.37 and accounting for the nonlinearity of the variables T and p, therefore invoking the material derivative, can be rewritten and rearranged as

$$c_p \frac{DT}{Dt} = \frac{1}{\rho} \frac{Dp}{Dt} + \dot{Q} \tag{3.40}$$

By expanding the material derivative terms, the following is obtained

$$c_p \left(\frac{\partial T}{\partial t} + \vec{\mathbf{u}} \cdot \nabla T \right) = \frac{1}{\rho} \left(\frac{\partial p}{\partial t} + \vec{\mathbf{u}} \cdot \nabla p \right) + \dot{Q} \tag{3.41}$$

which, when applying the definition for the nonhydrostatic variables combined with the equation for hydrostatic balance, similar to the application seen in the derivation of the pressure tendency equation, results in

$$c_p \left(\frac{\partial T}{\partial t} + \vec{\mathbf{u}} \cdot \nabla T \right) = \frac{1}{\rho} \left(\frac{\partial p^{'}}{\partial t} + \vec{\mathbf{u}} \cdot \nabla p^{'} - \rho_o g w \right) + \dot{Q} \tag{3.42}$$

Equation 3.42 can then be rearranged to form MM5's thermodynamics equation, given by equation 3.10

$$\frac{\partial T}{\partial t} = -\vec{\mathbf{u}} \cdot \nabla T + \frac{1}{\rho c_p} \left(\frac{\partial p^{'}}{\partial t} + \vec{\mathbf{u}} \cdot \nabla p^{'} - \rho_o g w \right) + \dot{Q} \tag{3.43}$$

Derivation of the Equation for Zonal Momentum

The basic equation for zonal momentum, including nonlinear terms, is given by

$$\frac{Du}{Dt} = -\frac{1}{\rho} \frac{\partial p}{\partial x} + f v \tag{3.44}$$

By expanding the material derivative, the above equation can be rewritten and rearranged to give

$$\frac{\partial u}{\partial t} + \frac{1}{\rho}\frac{\partial p}{\partial x} = -\vec{\mathbf{u}} \cdot \nabla u + fv \tag{3.45}$$

Implementing the nonhydrostatic definition of variables, seen in equation 3.6, equation 3.45 becomes

$$\frac{\partial u}{\partial t} + \frac{1}{\rho}\frac{\partial p'}{\partial x} = -\vec{\mathbf{u}} \cdot \nabla u + fv \tag{3.46}$$

In order to transform the above equation into the coordinates (x, y, σ), the following coordinate transformation must be performed.

$$\left(\frac{\partial}{\partial x}\right)_z \Longrightarrow \left(\frac{\partial}{\partial x}\right)_\sigma - \left(\frac{\partial z}{\partial x}\right)_\sigma \frac{\partial}{\partial z} \tag{3.47}$$

Following the equation for hydrostatic balance,

$$\delta z = \frac{-\delta p_o}{\rho_o g} = -\frac{(p^* \delta\sigma + \sigma \delta p^*)}{\rho_o g} \tag{3.48}$$

where p^* is defined as $p_{surface} - p_{top}$. Applying this to equation 3.47 results in

$$\left(\frac{\partial}{\partial x}\right)_z \Longrightarrow \left(\frac{\partial}{\partial x}\right)_\sigma - \frac{\sigma}{p^*}\frac{\partial p^*}{\partial x}\frac{\partial}{\partial \sigma} \tag{3.49}$$

This transformation is now used to rewrite equation 3.46 as

$$\frac{\partial u}{\partial t} + \frac{1}{\rho}\left(\frac{\partial p'}{\partial x} - \frac{\sigma}{p^*}\frac{\partial p^*}{\partial x}\frac{\partial p'}{\partial \sigma}\right) = -\vec{\mathbf{u}} \cdot \nabla u + fv \tag{3.50}$$

From here, MM5 then implements a map-scale factor m, terms to account for the effects of Earth's curvature and centripetal acceleration, a horizontal diffusion term D_u, as well as a term to account for an extra component to Coriolis acceleration containing e. This often neglected component of the Coriolis force, given as

$$e = 2\Omega \cos \lambda \tag{3.51}$$

Accounting for this component of the Coriolis force makes it not necessary to define the origin of our reference state along the axis of rotation, and hence allows for the angular velocity Ω to be defined as having three components (x, y, z). Essentially, implementing this component of the Coriolis force accounts for the slight tilt in Earth's rotational axis. Combining all of these effects into equation 3.50 results in MM5's equation for zonal momentum as seen in equation 3.11.

$$\frac{\partial u}{\partial t}+\frac{m}{\rho}\left(\frac{\partial p'}{\partial x}-\frac{\sigma}{p^*}\frac{\partial p^*}{\partial x}\frac{\partial p'}{\partial \sigma}\right) = -\vec{\mathbf{u}}\cdot\nabla u+v\left(f+u\frac{\partial m}{\partial y}-v\frac{\partial m}{\partial x}\right)-ew\cos\alpha-\frac{uw}{r_e}+D_u \tag{3.52}$$

where α represents the degree of deviation from a central longitude, and the extra Coriolis parameter accounts for the meridional component of angular velocity.

Derivation of the Equation for Meridional Momentum

The basic equation for meridional momentum, including nonlinear terms, is given by

$$\frac{Dv}{Dt} = -\frac{1}{\rho}\frac{\partial p}{\partial y} - fu \tag{3.53}$$

which, by implementing the same method as seen for zonal momentum above, can be rewritten as

$$\frac{\partial v}{\partial t} + \frac{1}{\rho}\frac{\partial p^{'}}{\partial y} = -\vec{\mathbf{u}} \cdot \nabla v - fu \tag{3.54}$$

Next, by using the same coordinate transformation seen in equation 3.49, but replacing x with y, we obtain

$$\frac{\partial v}{\partial t} + \frac{1}{\rho}\left(\frac{\partial p^{'}}{\partial y} - \frac{\sigma}{p^*}\frac{\partial p^*}{\partial y}\frac{\partial p^{'}}{\partial \sigma}\right) = -\vec{\mathbf{u}} \cdot \nabla v - fu \tag{3.55}$$

From here, the same implementations seen for the zonal momentum equation are made by MM5, accounting this time for the zonal component of angular velocity in the second Coriolis component, which results in the equation for meridional momentum as seen in equation 3.12.

$$\frac{\partial v}{\partial t}+\frac{m}{\rho}\left(\frac{\partial p^{'}}{\partial y}-\frac{\sigma}{p^*}\frac{\partial p^*}{\partial y}\frac{\partial p^{'}}{\partial \sigma}\right) = -\vec{\mathbf{u}}\cdot\nabla v-u\left(f+u\frac{\partial m}{\partial y}-v\frac{\partial m}{\partial x}\right)+ew\sin\alpha-\frac{vw}{r_e}+D_v \tag{3.56}$$

Derivation of the Equation for Vertical Momentum

The derivation for vertical momentum differs from that of zonal or meridional momentum, as hydrostatic balance (i.e. buoyancy) needs to be accounted for. The basic equation for vertical momentum is given by

$$\rho\frac{Dw}{Dt} = -\frac{\partial p}{\partial z} - \rho g \tag{3.57}$$

Implementing the definition of $\alpha = \frac{1}{\rho}$ seen previously, this can be rewritten as

$$\frac{Dw}{Dt} + \alpha\frac{\partial p}{\partial z} + g = 0 \tag{3.58}$$

From here, using the definition of nonhydrostatic for α and p, as seen in equations 3.6-3.8, equation 3.58 becomes

$$\frac{Dw}{Dt} + (\alpha_o + \alpha^{'})\left(\frac{\partial p_o}{\partial z} + \frac{\partial p^{'}}{\partial z}\right) + g = 0 \tag{3.59}$$

which can then be expanded as

$$\frac{Dw}{Dt} + \alpha_o\frac{\partial p_o}{\partial z} + \alpha_o\frac{\partial p^{'}}{\partial z} + \alpha^{'}\frac{\partial p_o}{\partial z} + \alpha^{'}\frac{\partial p^{'}}{\partial z} + g = 0 \tag{3.60}$$

From hydrostatic balance, written with respect to α as seen below

$$\alpha_o\frac{\partial p_o}{\partial z} = -g \tag{3.61}$$

equation 3.60 can be rewritten, with like terms combined, as

$$\frac{Dw}{Dt} + \alpha\frac{\partial p^{'}}{\partial z} + \alpha^{'}\frac{\partial p_o}{\partial z} = 0 \tag{3.62}$$

Again, implementing hydrostatic balance as seen in equation 3.61, the above equation can be rewritten as

$$\frac{Dw}{Dt} + \alpha\frac{\partial p^{'}}{\partial z} - g\frac{\alpha^{'}}{\alpha_o} = 0 \tag{3.63}$$

Next, the $\alpha^{'}$ is expanded as $\alpha - \alpha_o$, which results in

$$\frac{Dw}{Dt} + \alpha\frac{\partial p^{'}}{\partial z} - g\frac{\alpha - \alpha_o}{\alpha_o} = 0 \tag{3.64}$$

The term on the right hand side, when written with respect to ρ, can be simplified using the following method.

$$\begin{aligned}\frac{\alpha-\alpha_o}{\alpha_o} &= \frac{\frac{1}{\rho}-\frac{1}{\rho_o}}{\frac{1}{\rho_o}} \\ &= \frac{\rho_o-\rho}{\rho} \qquad (3.65)\end{aligned}$$

This can be expressed in terms of temperature by implementing the ideal gas law (as seen in equation 3.18), as well as the nonhydrostatic definition of variables given in equations 3.6-3.8, in the following method.

$$\begin{aligned}\frac{\rho_o-\rho}{\rho} &= \frac{\rho_o}{\rho}-1 \\ &= \frac{p_oT}{pT_o}-1 \\ &= \frac{p_o}{p}\left(\frac{T}{T_o}-\frac{p}{p_o}\right) \\ &= \frac{p_o}{p}\left(\frac{T^{'}}{T_o}-\frac{p^{'}}{p_o}\right) \qquad (3.66)\end{aligned}$$

Inputting equation 3.66 into equation 3.64 results in the following

$$\frac{Dw}{Dt}+\frac{1}{\rho}\frac{\partial p^{'}}{\partial z}-g\frac{p_o}{p}\left(\frac{T^{'}}{T_o}-\frac{p^{'}}{p_o}\right)=0 \qquad (3.67)$$

Next, the material derivative is expanded, and the equation is rearranged into the following

$$\frac{\partial w}{\partial t}+\frac{1}{\rho}\frac{\partial p^{'}}{\partial z}=-\vec{\mathbf{u}}\cdot\nabla w+g\frac{p_oT^{'}}{pT_o}-g\frac{p^{'}}{p} \qquad (3.68)$$

After some rearranging and substitution using $R_d = c_p - c_v$, the above equation becomes

$$\frac{\partial w}{\partial t}+\frac{1}{\rho}\frac{\partial p^{'}}{\partial z}+\frac{g}{\gamma}\frac{p^{'}}{p}=-\vec{\mathbf{u}}\cdot\nabla w+g\frac{p_oT^{'}}{pT_o}-\frac{gR_d}{c_p}\frac{p^{'}}{p} \qquad (3.69)$$

which, after applying the coordinate transformation to the differential in the z component as well as implementing the effects of curvature, vertical diffusion, the often neglected component of the Coriolis force and centripetal acceleration, results in the equation used in MM5 for vertical momentum, as seen in equation 3.13.

$$\frac{\partial w}{\partial t}-\frac{\rho_o}{\rho}\frac{g}{p^*}\frac{\partial p'}{\partial \sigma}+\frac{g}{\gamma}\frac{p'}{p}=-\vec{\mathbf{u}}\cdot\nabla w+g\frac{p_o}{p}\frac{T'}{T_o}-\frac{gR_d}{c_p}\frac{p'}{p}+e(u\cos\alpha-v\sin\alpha)+\frac{u^2+v^2}{r_e}+D_w \tag{3.70}$$

While the above equation experiences no influence from the Coriolis component f, it does in fact take into account the meridional and zonal component of Earth's angular velocity, hence the use of the term containing e.